Title
Through-going Muons in the LUX Dark Matter Search

Author
Ihm, Catherine Mia

Publication Date
2018

Peer reviewed|Thesis/dissertation

Through-going Muons in the LUX Dark Matter Search

by

Catherine Mia Ihm

A dissertation submitted in partial satisfaction of the

requirements for the degree of

Doctor of Philosophy

in

Physics

in the

Graduate Division

of the

University of California, Berkeley

Committee in charge:

Professor Robert G. Jacobsen, Chair
Professor Bernard Sadoulet
Professor Kai Vetter

Summer 2018

Through-going Muons in the LUX Dark Matter Search

Abstract

Through-going Muons in the LUX Dark Matter Search

by

Catherine Mia Ihm

Doctor of Philosophy in Physics

University of California, Berkeley

Professor Robert G. Jacobsen, Chair

Dark matter makes up most of the mass of the universe, and yet the true nature of this mysterious substance remains unknown. The LUX experiment uses a detector consisting of target xenon nuclei to search for Weakly Interacting Massive Particles, a promising dark matter candidate. The LUX detector is a 370 kg dual-phase xenon time projection chamber. Incident radiation interacts with xenon atoms, resulting in a recoil nucleus or electron that causes both ionization and excitation of Xe along the recoil track. De-excitation of Xe results in the emission of 175 nm scintillation light, and the properties of this scintillation can be used to determine the nature of the incident radiation - possibly identifying WIMP dark matter.

LUX has placed world-leading limits on the WIMP-nucleon interaction cross section. The rarity of such interactions requires a thorough understanding of backgrounds in order to implement appropriate background-reducing measures and an effective event-rejection methodology. The LUX water tank surrounds the xenon detector and serves as an active shield, reducing background radiation but also identifying high energy cosmic ray muons that can lead to the production of a highly undesirable neutron background. Since signals created by neutrons may appear very similar to those of WIMPs, care must be taken to not only reduce neutron backgrounds as much as possible, but to also understand any neutron backgrounds that may be present.

The goal of this dissertation was to develop a method to identify cosmic ray muons that traverse both the LUX Xe detector and water tank, and to measure a muon flux at the LUX detector depth. The xenon gas-liquid interface served as a fiducial surface through which muon flux was measured. Simultaneous signals between Xe and water detectors were analyzed, and xenon pulse shapes were used to determine the energy and track geometry of the interaction. Muons passing the Xe liquid surface exhibited a particular signature in their pulse shape; this signature was used to identify through-going muons and calculate muon flux.

In a previous work, muon flux measurements were taken at sites above the LUX detector, and muon transport models were used to predict vertical muon flux as $4.40 \times 10^{-9}\,\mathrm{muons\,s^{-1}\,cm^{-2}}$ at the LUX detector depth. In this work, a flux of $(4.60 \pm 0.33_{stat}) \times 10^{-9}\,\mathrm{muons\,s^{-1}\,cm^{-2}}$ is measured through the LUX water tank and xenon detector liquid surface. The resulting neutrons expected to be seen during the full LUX exposure is $\sim 1 \times 10^{-1}$.

While expected the background contribution from muon-induced neutrons poses little problem for the LUX WIMP search, an understanding of this background becomes increasingly important as target volumes grow for future generation experiments.

Contents

List of Figures

List of Tables

Acknowledgments

This dissertation would not have been possible without the support of many people, and I am truly grateful for everyone who has helped me along.

First and foremost, I must thank Bob Jacobsen, my advisor who has stuck by me through my long grad career. Thanks for all your insights, both in physics and beyond. I can only hope to someday achieve your intuition for physics and instrumentation, or your patience and kindness.

Thanks to Jim Siegrist for first introducing me to detectors along with my committee member Kai Vetter. I learned so much in your imaging lab, and I am a better experimentalist because of my time there.

And thanks to Bernard Sadoulet, my other committee member, who is a scion of the field and has mentored my mentors. You've taught me so much about cosmology and dark matter.

My first mentor, Vicky Kalogera, has been an amazing role model and continues to inspire me by being a kickass astrophysicist.

I've been lucky to be a part of an amazing experiment, and even luckier that that experiment is made up of amazing people. Thanks for all the good times in South Dakota, both at work and at play - you made Lead, SD more than just a place to work, it became my second home. And here I will try to name all of you, in no particular order: Rachel, Patrick, Carmen, Emily, Monica, Simon, Carlos, Dave, Jeremy C, Peter, Michal, Eryk, Mongkol, James V, Alexey, James N, Sid, Louis, Lucie, Ethan, Blair, Scott, Kevin, Markus, Nicole, Evan, Brian, Mark, Doug, Curt, Attila, Richard, Jon, Nick, Matthew, Mike W, Surge, Jeremy M, James M, Kareem, Chao, Dana, Chris and Angela C, Richard O, Alastair, Jim, Vladimir, Luiz, Alex, Francisco, Claudio, Kelsey, Mike C, Dev, Mary, Karen, Adam, Chang, Kati... and I know there are more. Robyn, Oren, and Dave T - all your support and smiles at Homestake have been invaluable. And thanks to all the PIs, for all your hard work and mentorship. It has been an honor to work with you all.

I've had great LUX colleagues at Berkeley: Alex, Sophia, Addi, Vic, Daniel, Kate, thanks for growing our group and sharing in this experience. And no Berkeley physics graduate student could have made it through without the department's support services, so a special thank you to Anne Takizawa and Donna Sakima for your unfailing help and huge hearts.

Of course I wouldn't be who I am today without my family and friends. Thanks Mom, Dad, Al, Beckey, and Caleb. Thanks to all the friends, housemates, campmates that have made sure that I have a life outside physics, and forgive me for any neglect I may have shown these past years.

I couldn't have done this without you.

Chapter 1

Introduction

This dissertation is presented in two parts. The first focuses on dark matter as the motivation behind the Large Underground Xenon (LUX) detector. Chapter 2 gives an overview of the current understanding of dark matter: evidence that it exists, possible candidates, and arguments for WIMP dark matter, the candidate of choice for the LUX. Chapter 3 discusses various detection methods and current experiments; the operating principles behind noble gas detectors are introduced. Chapter 4 describes the LUX detector: its design and construction as well as features of data acquisition and data processing.

Part II addresses a possible background source: cosmic ray muons. While muons can be easily identified and rejected inside the LUX detector, they can give rise to neutrons through interactions with the surrounding rock and water. Neutrons are a particularly troublesome background because their interactions within the LUX detector mimic WIMP interactions. Understanding how many muon-induced neutrons may appear in the detector is necessary to determine possible WIMP signals and to calculate WIMP limits and rates. Chapter 5 briefly introduces cosmic ray muons and their behavior below the surface of the earth. Chapter 6 describes another detector, the LUX water shield and veto system. In Chapter 7, a method for identifying cosmic ray muons using LUX and its veto is proposed. Using this method, a cosmic ray muon flux for the 4850 level of Homestake is determined, which is the subject of chapter 8.

To conclude, Chapter 9 presents some final results and future prospects, now that the LUX detector has been decommissioned.

The author of this dissertation has been lucky enough to see evolution of LUX from construction to data collection and analysis. Her main hardware contributions were the design and construction of the high voltage systems that powered the grids, which maintained the appropriate electric fields within the detector. Her software and analysis contribution focused on the commissioning of the water tank PMTs, and on the identification of through-going muons. The resulting calculation of the muon rate and any associated uncertainties were also done by the author, and constitute the main thesis of this work.

Before the LUX detector was deployed deep underground for its science runs, it underwent a trial run at the surface as a test of all major systems. Operation of the detector at

Figure 1.1: The Flammarion engraving, seeing past the firmament

the surface required special considerations due to the high rate of cosmic rays. With so much activity in the detector, all the light generated could degrade the light-collecting photomultiplier tubes. The author developed a direct charge readout of signals that offered another way of identifying interactions within the detector, without using light. A charge-sensitive preamplifier was connected to the detector, collecting any charge liberated by recoils within the detector. The author also built the circuitry to control the preamplifier, and developed the software to read out and analyze its signals. Due to limited time on the surface run, a significant amount of data could not be collected from the charge readout. As it is unrelated to main focus of this work, the charge readout won't be detailed any further in this dissertation.

Amidst all the details and humble contributions that add up to an experiment such as LUX, one can forget what makes science a noble, fulfilling pursuit. We are trying to see past the universe we know, to what is beyond the firmament.

Part I

Detecting Dark Matter

Chapter 2

Dark Matter: Background and Motivation

2.1 The Makeup of the Universe

According to the current scientific consensus, only a small fraction of the energy density of the universe consists of the normal, baryonic matter that dominates everyday life. Dark energy, which can also be referred to as Λ, is the mysterious entity that accelerates the expansion of the universe, and it is responsible for 71% of the energy density of the universe. The remaining 29% consists of "matter", which tries to slow down the expansion of the universe through gravitational attraction. Only a small fraction of this matter is baryonic, most of it is in the form of cold, dark matter (CDM). The ΛCDM model does remarkably well for explaining the dynamics of the universe on large scales. The dynamics of the universe, and its history, simply cannot be explained by a universe consisting of only stars and other baryonic matter. The following walk through the standard cosmology results from knowledge gained in the treatments in References [1] and [2].

Astronomical observations have repeatedly confirmed that at large scales, the universe is isotropic and homogeneous. The metric of such a universe follows the Robertson-Walker metric:

$$ds^2 = -c^2dt^2 + a(t)^2\left[\frac{dx^2}{1-\kappa x^2/R_0^2} + x^2 d\Omega^2\right]. \tag{2.1}$$

In equation 2.1, the scale factor $a(t)$ describes the expansion (or contraction) of the universe, which may change with time t. The factors κ and R_0 describe the curvature of the universe. The values of κ can be -1, 0, or 1, which correspond to negative, flat, and positive curvature respectively, and R_0 is the radius of curvature.

The Einstein field equations relate the space-time metric to the energy and pressure of a point in space:

$$G_{\mu\nu} \equiv R_{\mu\nu} - \frac{1}{2}Rg_{\mu\nu} = \frac{8\pi G}{c^4}T_{\mu\nu} + \Lambda g_{\mu\nu} \tag{2.2}$$

$G_{\mu\nu}$ defines the *Einstein tensor*. The components of the Ricci curvature tensor $R_{\mu\nu}$

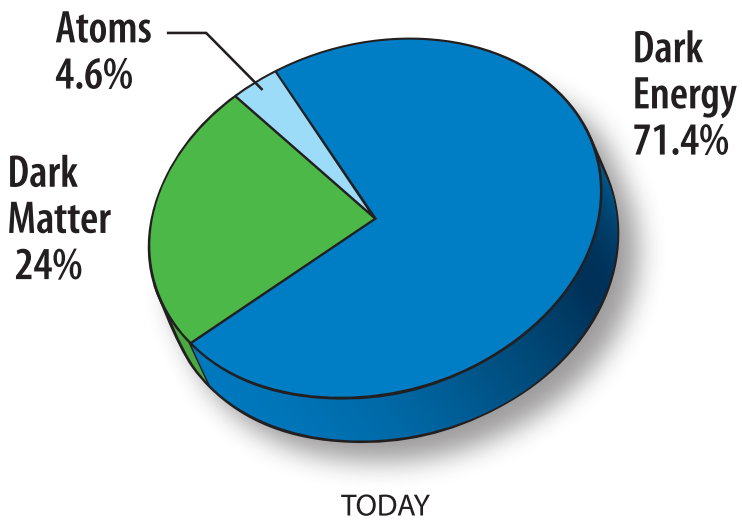

Figure 2.1: The makeup of the universe. Precision measurements from the Wilkinson Microwave Anisotropy Probe can help determine the density of atomic and non-atomic matter in the universe. Credit: NASA/WMAP Science Team

can be found from the scale factor $a(t)$ and its time derivatives, as can the Ricci scalar R. Cosmological constant Λ describes the energy density that arises from the vacuum of space, even absent of matter. $T_{\mu\nu}$ is the stress-energy tensor, which describes the state of energy and momentum. G is the gravitational constant, c the speed of light.

Equation 2.1 can be used for the metric $g_{\mu\nu}$, and Einstein's field equations can relate the metric to energy and pressure, leading to the Friedmann equation:

$$\left(\frac{\dot{a}}{a}\right)^2 = H(t)^2 = \frac{8\pi G}{3c^2}\varepsilon - \frac{\kappa c^2}{R_0^2 a^2} + \frac{\Lambda}{3} \tag{2.3}$$

where the Hubble parameter $H(t)$ describes the expansion rate with $\frac{\dot{a}}{a}$.

The critical density ε_{crit} can also be defined here as the present-day energy density for a flat universe ($\kappa = 0$) and no cosmological constant ($\Lambda = 0$), or $\varepsilon_{crit} = \frac{3H_0^2 c^2}{8\pi G}$.

Present-day density parameters Ω_x can subsequently be defined with respect to ε_{crit} :

$$\Omega_x = \frac{\varepsilon_x}{\varepsilon_{crit}} \tag{2.4}$$

where subscript x denotes various components affecting the energy density of the universe: radiation, matter (baryonic and cold dark matter), curvature κ, and Λ.

The symmetry of the metric $g_{\mu\nu}$ simplifies the stress-energy tensor to only the diagonal terms: $T_{\mu\nu} = \mathrm{diag}(\varepsilon, -p, -p, -p)$ where p is pressure. The fluid equation

$$\dot{\varepsilon} + 3\frac{\dot{a}}{a}(\varepsilon + p) = 0 \tag{2.5}$$

can be derived from conservation of stress-energy (or the first law of thermodynamics). Equations of state $p = w\varepsilon$ relate pressure and energy density, and from Equation 2.5 the energy density relates to the scale factor as

$$\varepsilon \propto a^{-3(1+w)} \tag{2.6}$$

Some important examples are:

$$\begin{array}{lll} \text{Radiation:} & p = \frac{1}{3}\varepsilon & \rightarrow \varepsilon \propto a^{-4} \\ \text{Matter:} & p = 0 & \rightarrow \varepsilon \propto a^{-3} \\ \text{Dark Energy } (\Lambda): & p = -\varepsilon & \rightarrow \varepsilon \propto \text{constant} \end{array} \tag{2.7}$$

The Friedmann Equation 2.3 can be taken together with the fluid equation (Eq. 2.5) and equation of state (Eq. 2.6) to solve for the cosmological parameters of interest, $a(t)$ and $\varepsilon(t)$. Considering a universe of multiple components, $\varepsilon = \sum \varepsilon_x$, the Friedmann Equation 2.3 can be rewritten as

$$\frac{H^2}{H_0^2} = \frac{\Omega_{r,0}}{a^4} + \frac{\Omega_{m,0}}{a^3} + \Omega_{\Lambda,0} + \frac{1 - \Omega_0}{a^2} \tag{2.8}$$

where the 0 subscript refers to present day, r to radiation, m to matter, and $\Omega_0 = \Omega_{r,0} + \Omega_{m,0} + \Omega_{\Lambda,0}$

The results of several independent observations converge upon the result of a flat, Λ-dominated universe (see Figure 2.2, Reference [3]). The ΛCDM model is also known as the Benchmark model, and consists of a 71% dark energy contribution to energy density, and a 29% matter contribution. The matter portion can be split further into a 24% dark matter component, and 5% baryonic matter component. While the observations have demonstrated the robustness of the model, they also reveal our ignorance concerning over 95% of the energy density of the universe. While we are certain of the existence of these components, the nature of dark matter and dark energy is largely unknown.

2.2 Evidence for Dark Matter

For nearly a century, the astronomical evidence for dark matter has been mounting. Several different observations hint at a mysterious "missing mass," and some of them are detailed in this section.

2.2.1 A First Hint: the Coma Cluster

In 1933, Fritz Zwicky applied the virial theorem to galaxies in the Coma Cluster to relate the kinetic (T) and potential (V) energies of the bound system:

$$< T >= -\frac{1}{2} < V > \tag{2.9}$$

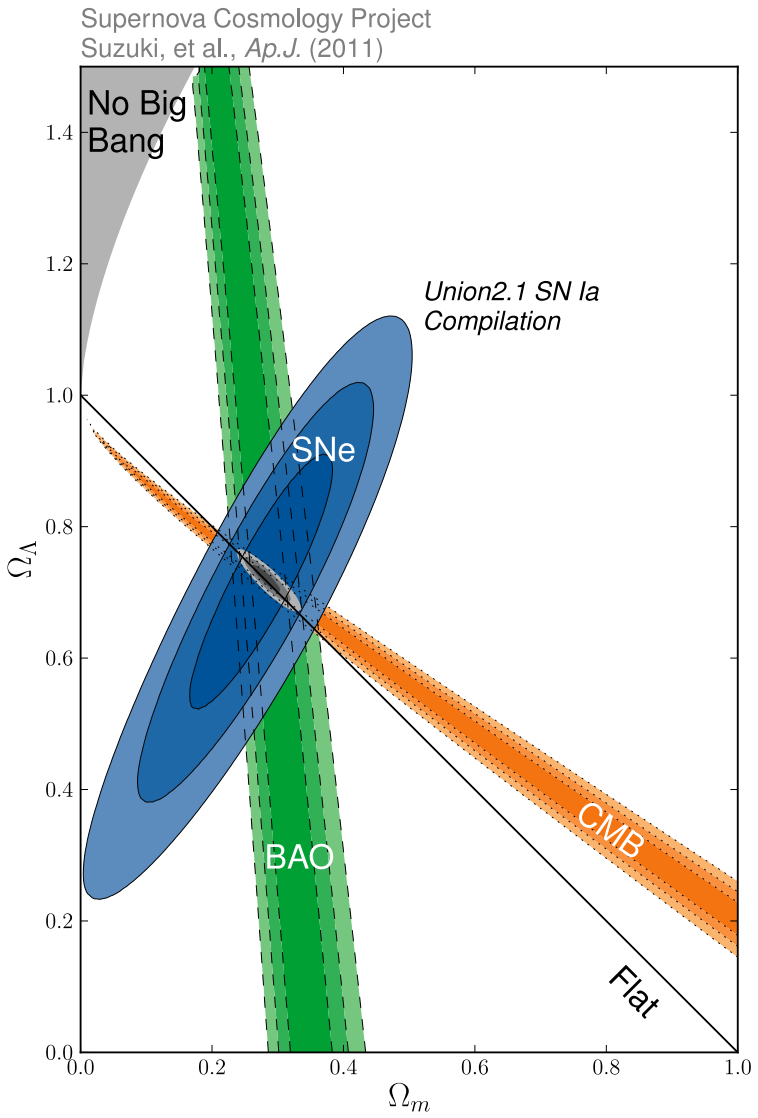

Figure 2.2: The ΛCDM consensus. Supernova, Cosmic Microwave Background, and baryon acoustic oscillation data combine to point to a universe that is 71% dark energy, 29% matter, and flat. Figure from Reference [3].

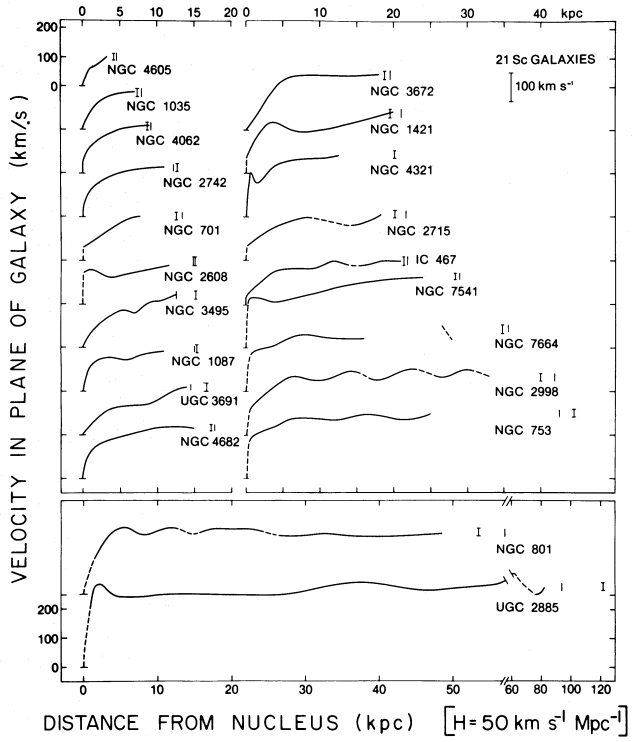

Figure 2.3: Galactic rotation curves. Their shapes remain "flat" at large radii instead of dropping off as $\sqrt{r}$. From Reference [7]

The velocities of the galaxies were obtained through their observed Doppler shifts, which led to an estimation of the gravitational potential and mass of the system. Surprisingly, it was found that nearly 500 times more mass was required to explain the dynamics of the Coma cluster than that which was inferred from starlight alone (Reference [4]). The assumption at the time was that the bulk of the mass in galaxies and clusters should be coming from luminous matter (stars), but Zwicky concluded that most of the cluster mass must come in the form of *dunkle Materie*, or *dark matter* (Reference [5]).

Jan Hendrick Oort observed stars in our galaxy that were moving faster than could be explained by the light observed (Reference [6]). The example is one of many other measurements of anomalous mass-to-light ratios, but chosen here to recognize that the observation was made a year before Zwicky's now-famous study of the Coma cluster. Zwicky, however, was first to hypothesize that the phenomena was caused by the now-embraced explanation of missing mass, dark matter.

2.2.2 Galactic Rotation Curves

For an object mass m in a circular orbit of radius r, orbital speed v can be related to the mass $M(r)$ enclosed in its orbit by equating centripetal and gravitational forces:

$$\begin{aligned} \frac{mv^2}{r} &= \frac{GmM(r)}{r^2} \\ v(r) &= \sqrt{\frac{GM(r)}{r}} \end{aligned} \tag{2.10}$$

At distances far from the center of a galaxy, the mass enclosed within some radius wasn't expected to increase with increasing radius. This reasoning again relies upon the assumption that most of the mass of a galaxy is tied to its luminous matter. With $M(r)$ becoming a constant at large radii, Equation 2.10 says that orbital velocities should drop off as $\sqrt{r}$. However, studies of rotation curves of galaxies do not exhibit this drop-off, but instead velocities remain flat even far away from galactic centers (see Figure 2.3). Vera Rubin later attached a mass profile to explain these strange rotation curves in Reference [7]. In order to explain the flat rotation curves, enclosed mass should be proportional to r, or mass density $\rho \propto r^{-2}$. The numerous observations of flat rotation curves indicated that these galaxies also possess a massive, spherical halo of non-luminous matter that extends to radii well beyond the luminous disks.

2.2.3 Gravitational Lensing

In Einstein's theory of general relativity, mass determines the shape of its surrounding spacetime, and in a cosmic feedback loop, the paths of mass and light are governed by the shape of the spacetime they move through. One can infer the existence of missing mass through gravitational lensing, the bending of light by massive objects. One canonical example is that of the lensing from galaxy cluster Abell 2218 (see Figure 2.4). The galaxy cluster Abell 2218 is in the foreground and acts as the lens (the agent that bends light), while light from background galaxies gets distorted into circular arcs around the lens. Depending on the position and alignment of the background objects with respect to the lens, the background light could even take multiple paths around the lens, or form an Einstein ring around the lens. Highly deformed shapes and light paths are hallmarks of *strong lensing*. The degree of distortion a lens causes is dependent on the mass of the lens. Lensing can be thus used to estimate the masses of galaxies and clusters without depending on the light output of luminous matter. Indeed, the luminous mass is not sufficient to explain the lensing effects seen, much more mass is needed.

In *weak lensing* and *microlensing*, the shapes of light coming from background galaxies will be warped/sheared slightly, but not as dramatically as galaxies more closely aligned with the lens. Instead, astronomers look for preferred alignments of possibly lensed objects, where the presence of a gravitational lens could "stretch" background galaxy shapes all in the same direction. If a statistically significant slant to galaxy shapes appears rather than

Figure 2.4: Gravitational lensing by galaxy cluster Abell 2218. Photo Credit: NASA, ESA, A. Fruchter and the ERO Team (STScI, ST-ECF).

a random assortment of shapes and orientations, it may be caused by a gravitational lens. If weak/microlensing occurs in the absence of a massive, luminous lens, again a "missing mass" must account for the observed distortions.

2.3 Dark Matter Candidates

There is no longer any doubt that a considerable dark component makes up the masses of galaxies and clusters. Even though dark matter is not seen directly, the gravitational effects (too-fast orbits, lensing) are undeniable. The question has now turned to the nature of dark matter: what exactly *is* it? Several possible explanations are mentioned in this section, but the account is by no means exhaustive. Some models have obvious shortcomings, but are mentioned here for their historical context, and to help build the case for this dissertation's preferred dark matter candidate: Weakly Interacting Massive Particles (WIMPs).

2.3.1 MACHOs and Other Baryons

One initial explanation for dark matter is that it is simply ordinary matter that does not shine like a star. Interstellar gas, planets, and brown dwarfs are all types of nonluminous baryonic matter. Compelling contenders were dubbed MAssive Compact Halo Objects (MACHOs), astronomical compact objects such as black holes, neutron stars, white dwarfs and brown dwarfs. Compact objects are the end states of stars. While they may exhibit compa-

rable masses to stars, they no longer (or never in the first place did) undergo thermonuclear fusion, and thus do not emit light. The EROs and MACHO collaborations searched for weak lensing events caused by MACHOs (as described in Section 2.2.3). Analysis shows that only up to 20% of the typical dark matter halo model could be made up of MACHOs (Reference [8]).

Big-Bang Nucleosynthesis

Furthermore, Big-Bang-nucleosynthesis (BBN) calculations show that most dark matter cannot be baryonic, ruling out gas and dust as major dark matter contributors. The baryon-photon ratio η determines baryon density parameter Ω_b (as defined in Equation 2.4). Deuterium is believed to have only been created in the early universe. Its primordial abundance, observed in gas clouds, offers insight into the reaction rates of BBN, and can be used to infer η and Ω_b (Reference [9]). Using deuterium line observations, the baryon density parameter Ω_b has been constrained to be much less than the the overall matter density parameter Ω_m (Reference [10]), so a complete understanding of dark matter requires a non-baryonic component. While non-luminous baryonic matter certainly exists, not enough exists to explain all of the missing mass attributed to dark matter.

Cosmic Microwave Background Observations

Additional arguments against baryonic dark matter come from the observations of the Cosmic Microwave Background (CMB). The CMB (see Figure 2.5) comes from the time when the early universe had expanded and cooled enough to become transparent to photons. The CMB photons were no longer being constantly scattered by electrons and protons, and instead traveled freely to us, the observers of the CMB, after a journey of nearly 14 billion years through an expanding universe. Fluctuations in the CMB are the seeds from which large scale structure in the universe has grown.

CMB fluctuations can reveal a great deal about the structure of the universe at the time of recombination, the era where electrons and protons first formed neutral hydrogen. Recombination immediately preceded photon decoupling, where CMB photons originate. Density fluctuations in the primordial plasma before recombination induced acoustic oscillations where gravitational compressions were countered by radiation pressure. The resulting anisotropies are interpreted in an angular power spectrum of the CMB (see Figure 2.6), where the amplitudes of the peaks at specific multipole moments can expose the contributions of various components of the universe: baryons, photons, and even dark matter. The shape of the power spectrum is well-explained by the ΛCDM model, where dark matter makes up approximately 24% of the energy density or 84% of the mass of the universe.

2.3.2 Neutrinos

Neutrinos are another known particle, but nonbaryonic, that might be considered dark matter. They interact via the gravitational and weak force alone and are difficult to detect.

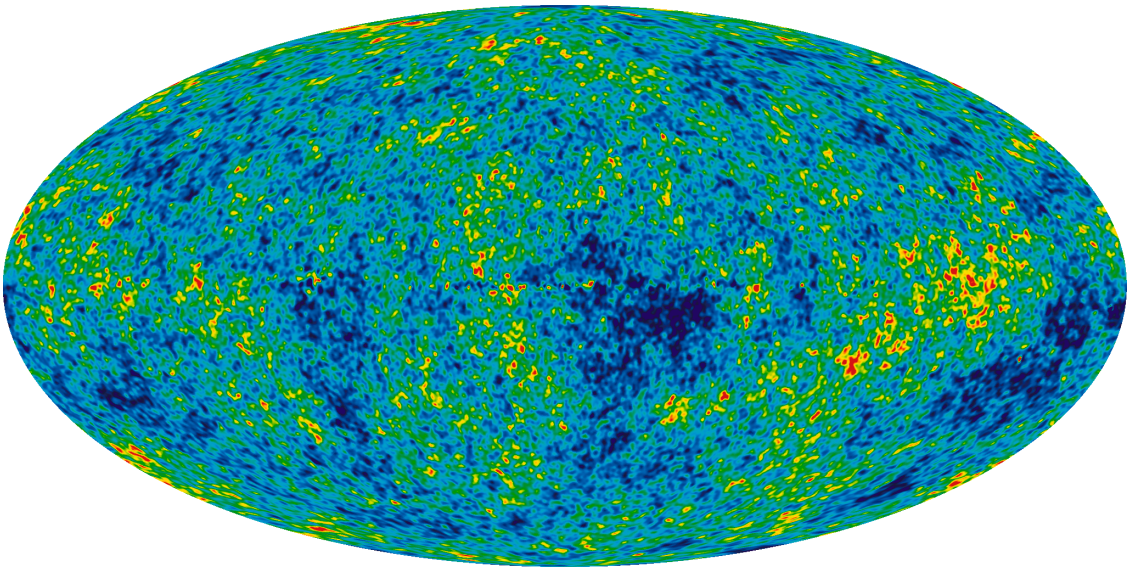

Figure 2.5: 9 year WMAP all-sky picture of the Cosmic Microwave Background. This map shows the unscattered photons reaching us from the time when the universe first became transparent. The differing colors represent temperature fluctuations of $\pm 200\,\mu$Kelvin. Photo Credit: NASA/WMAP Science Team

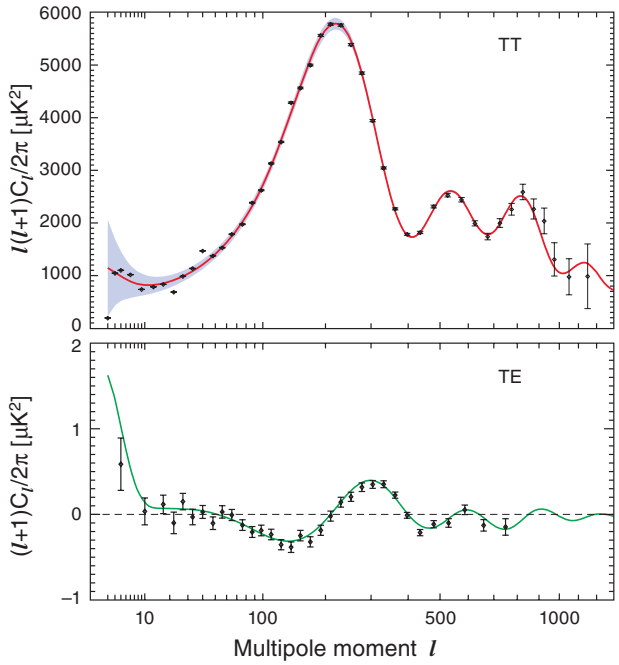

Figure 2.6: WMAP angular power spectrum. The data are well fit by the ΛCDM model (solid line). The model parameters are approximately $\Omega_b h^2 = 0.0226$, $\Omega_c h^2 = 0.1123$, $\Omega_\Lambda = 0.728$. From Reference [11].

These relativistic particles were initially thought to be massless, but observations of flavor mixing quashed expectations by requiring nonzero neutrino mass. While the exact masses of neutrinos are currently not known, they must have *some* mass - and could be the massive, non-luminous explanation for dark matter.

However, if neutrinos were to contribute significantly to the universe's dark matter inventory, large scale structure formation could not have occurred (Reference [12]). The small density fluctuations that served as the seeds for future galaxies would have been smoothed out by the relativistic neutrinos. Neutrinos as dark matter contradicts the structure observed in the universe today, and so another necessary attribute of dark matter arises: it must be nonrelativistic, or "cold."

2.3.3 Modified Gravity and Dynamics

MOdified Newtonian Dynamics (MOND) and other modified gravity theories say that the classical laws of gravity and dynamics don't apply at large distance scales, and that some new unknown physics has come into play. Such paradigm-shifting theories seem almost natural as humans become able to observe the physical world on larger and larger scales. Our understanding of gravity near the surface of the earth gave way to the gravitational force between two bodies, which gave way to Einstein's general relativity. Will MOND or other modified gravity theories be next?

Modified gravity theories posit that dark matter isn't actually matter at all, but the manifestation of new laws of physics. While MOND may explain some aspects of dark matter well (Reference [13]), there are other areas in which it fails, as described in the next section.

2.4 The Case for WIMP Dark Matter

2.4.1 The Bullet Cluster

Galaxy cluster collisions offer a cosmic arena for testing matter interactions on large scales. The luminous components of galaxy clusters are galaxies and intergalactic gas. The understanding used to be that the majority of a cluster's mass comes from intergalactic gas. When two galaxy clusters collide, the galaxies themselves rarely collide with each other due to their sparse spacing. The gas does collide and becomes excited, resulting in the emission of X-rays. Observations of visible and X-ray emissions of the Bullet cluster collision show the galaxies and gas decoupling, with colliding gas exhibiting prominent bow shocks, and the stellar component passing through relatively unencumbered (see Figure 2.7).

Weak lensing (see Section 2.2.3) was used to map out the gravitational potential surrounding the Bullet cluster collision site. In the absence of dark matter, the potential should follow the dominant mass component: intergalactic gas, as highlighted by the emitted X-rays. However, the gravitational contours instead follow the light profiles of the collisionless galaxies, which collisionless dark matter is expected to coincide with spatially. An additional,

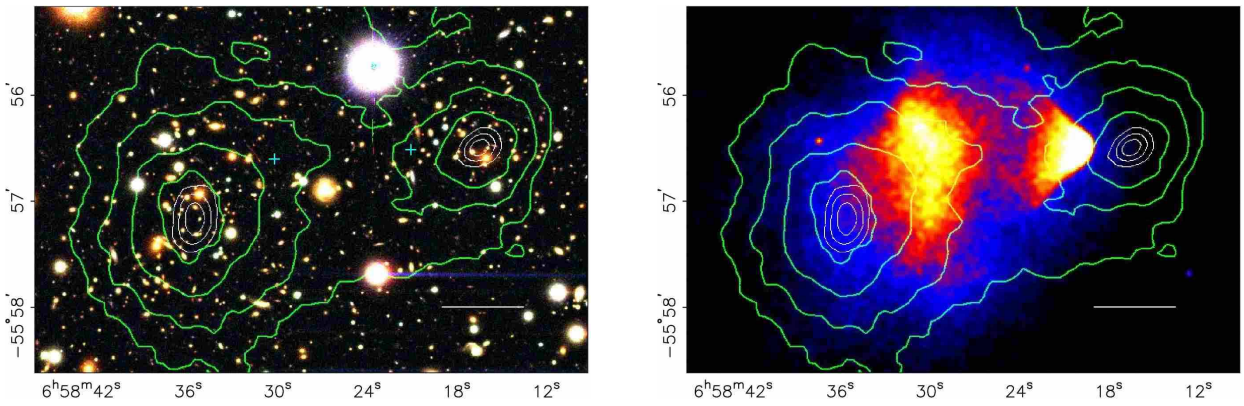

Figure 2.7: Bullet cluster. On the left, the galaxies making up the clusters are shown. X-ray emissions from the colliding intergalactic gas appear on the right. Contours mapping the gravitational potential, obtained through weak lensing, is shown in both images in green. The contours do not trace the X-rays, the dominant luminous component, but instead indicate that most of the mass is in the form of dark matter that remained relatively unaffected by the collision. From Reference [14].

invisible gravitational component must be following the galaxies. So gas still makes up the main baryonic component of these clusters, but lensing reveals another massive component that appears to rarely interact.

Theories of modified gravity and dynamics (Section 2.3.3) fail to explain how the observed gravitational profiles so completely mismatch the mass profiles outlined by intergalactic gas, the main baryonic component. The bullet cluster has been called the smoking gun in the compilation of evidence for dark matter (see Reference [14]). Furthermore, unlike the gas, dark matter appears to pass through itself freely in the cluster collision, indicating that dark matter should have a low self-interaction cross-section, lower than that of baryonic matter.

2.4.2 The WIMP Miracle

A series of potential dark matter candidates have fallen short of completely explaining the strange behaviors attributed to dark matter. However, these shortcomings help to identify qualities of an ideal dark matter candidate: matter that is non-luminous, non-baryonic, non-relativistic, and relatively seldom interacting. A new, yet-to-be-discovered particle could encompass all these characteristics and explain dark matter, and the existence of such a particle would be made all the more compelling if it were also able to explain outstanding questions in particle physics. Enter: the Weakly Interacting Massive Particle (WIMP).

Freeze-out, Relic Abundances

More details on following outline of early universe thermodynamics and particle freeze out can be found in Reference [1]. Natural units ($k_B = c = \hbar = 1$) are employed in this subsection.

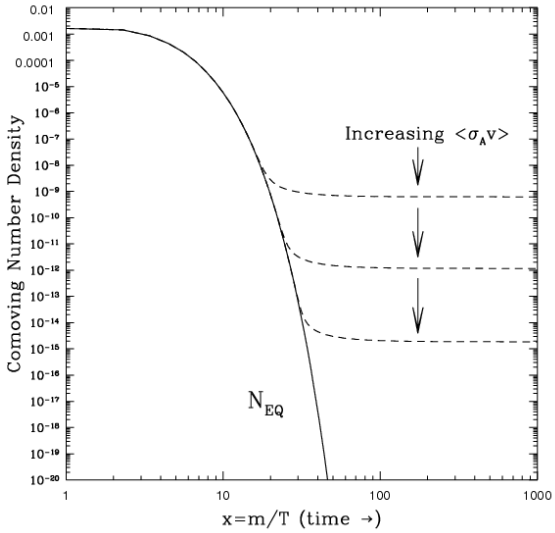

Figure 2.8: WIMP freeze-out. The solid curve N_{EQ} shows how number density changes with time if thermal equilibrium is maintained. The dashed lines show freeze-out occurring for different values of interaction cross section, breaking off the equilibrium annihilation curve when WIMPs become decoupled. Image from [15]

If a stable WIMP particle χ were to exist in the early universe, some relic abundance should exist today. While the universe was hot and dense with temperature $T \gg m_\chi$, the χ particle would maintain thermal equilibrium by annihilating with its antiparticle into Standard Model particle/antiparticle pairs $(\phi, \bar{\phi})$, and vice versa:

$$\chi\bar{\chi} \rightleftharpoons \phi\bar{\phi}. \tag{2.11}$$

As the universe cooled, the process of creating χ particles (right-to-left version of Equation 2.11) becomes suppressed because the Standard Model particles ϕ are not energetic enough to create χ particles, and subsequently the number density n_χ decreases. Annihilation rate Γ_χ also falls as n_χ falls since $\Gamma_\chi = \langle\sigma v\rangle n_\chi$ where $\langle\sigma v\rangle$ is the average χ annihilation cross section times velocity. A decoupling from thermal equilibrium roughly occurs when Γ_χ gets surpassed by the expansion rate of the universe H. More precisely, number density n_χ is governed by the Boltzmann equation:

$$\frac{dn_\chi}{dt} + 3Hn_\chi = -\langle\sigma v\rangle(n_\chi^2 - n_{eq}^2). \tag{2.12}$$

Here, n_χ^2 describes WIMP self-annihilation, and n_{eq}^2 the creation of WIMPs from lighter particles. In thermal equilibrium the right side of this equation equals zero, but as the universe cools and expands thermal equilibrium is not maintained. At some point the number of χ particles becomes fixed, with the *relic abundance* of χ remaining. This process is known as *freeze-out*. The curve illustrating freeze-out is displayed in Figure 2.8, where one can see where "freeze-out" occurs for different values of $\langle\sigma v\rangle$ as number density breaks off the standard annihilation curve and approaches a constant "frozen-in" value.

If the relic χ abundance were to explain the observed dark matter density in the universe today, then

$$\Omega_\chi h^2 \simeq \frac{3 \times 10^{-27} \text{cm}^3 \text{s}^{-1}}{\langle \sigma v \rangle} \tag{2.13}$$

Equation 2.13 can be used to determine WIMP cross section σ. The most recent results from Planck (Reference [16]) indicate that $\Omega_\chi h^2 \approx 0.12$. Taking velocity v to be velocity from the temperature at freeze-out, the resulting cross section $\sigma \simeq 10^{-37} \text{cm}^2$ is typical of weak-scale interactions, offering a convincing argument for a Weakly Interacting Massive Particle. By simply assuming that dark matter particles interact at the weak scale, one can predict roughly the correct observed dark matter abundance $\Omega_\chi h^2$. This coincidence has become known as the "WIMP miracle."

Hierarchy Problem

The treatment and result of the previous subsection, while interesting, does not constitute a miracle by itself. Rather, it is the concurrent prediction by particle physics of a particle on the electro-weak scale that makes the WIMP candidate miraculous. As cosmologists pondered the nature of the dark matter that appeared to dominate the universe, particle physicists were trying to solve their own problems. The WIMP provides a two-birds-with-one-stone solution for both fields.

The Standard Model (SM) of particle physics has served exceptionally well to explain the properties and interactions of the known particles. However, the Standard Model is at odds with the aesthetic desires of many physicists, who hope to unify the fundamental forces of physics: electromagnetic, strong, weak, gravitational. As it stands, quantum field theory (which encompasses the strong and electroweak forces) is incompatible with general relativity (gravity), and some new physics must come into play to reconcile the two into a more comprehensive, elegant model. One such attempt at reconciliation is supersymmetry, where all SM particles have supersymmetric partner particles.

The recent discovery of the Higgs Boson (References [17] and [18]) filled in the last missing piece of the Standard Model puzzle. Both the ATLAS and CMS experiments observed a Higgs Boson of mass ~ 125 GeV. The finding solidifies the presence of a *hierarchy problem* in the Standard Model. The Higgs Boson mass is expected to be on the order of the Planck scale, $\sim 10^{18}$ GeV, and in the absence of physics beyond the Standard Model, considerable fine tuning would be required in order to accommodate a Higgs mass that is so low. Supersymmetry would eliminate the need for fine tuning as the gauge hierarchy caused by SM particles would be balanced out by their supersymmetric partners (for supersymmetric masses on the order of 100's of GeV).

Finally, a quantum number called R-parity exists in supersymmetry, with $R = +1$ for normal particles and $R = -1$ for "super"-particles. Conservation of R-parity implies that the lightest supersymmetric particle (LSP) is stable, and that decay to a SM particle would be forbidden as it violates R-parity. This would mean that the LSP must still exist today, offering a testable hypothesis that is inviting further study.. The LSP makes for a well-

Figure 2.9: Wimps, a compelling candidate. Photo credit ROB MCEWAN / TWENTIETH CENTURY FOX.

motivated candidate for dark matter on the weak scale. The need from both astrophysics and particle physics for a LSP/WIMP makes the WIMP the most popular contender to explain dark matter. For more in-depth treatments of supersymmetry and supersymmetric dark matter, consult References [15], [19], and [20].

Not to be overlooked...

The overview of dark matter candidates in this chapter is by no means comprehensive, and many other compelling arguments exist in favor of these other candidates.

Axions ([21], [22], [23]), like WIMPs, provide solutions to open questions in both cosmology and particle physics. In quantum chromodynamics, the strong interaction allows for breaking of the combined symmetries of charge and parity (CP violation). However, such CP violation has never been observed, begging the question, "why not?" This puzzle has become known as the strong CP problem.

Peccei and Quinn proposed the Peccei-Quinn mechanism (Reference [24]) to solve the strong CP problem; a new symmetry is introduced. When the new symmetry is spontaneously broken, a new particle results and CP-violation is suppressed. This new particle is known as the axion, and if its mass were to be in the right range, it would both solve the strong CP problem and contribute significantly to the missing mass problem known as dark matter.

Several methods for searching for axions exist. Experiments such as the Axion Dark Matter eXperiment (ADMX, Reference [25]) seek to convert dark matter axions into microwave photons using a resonant microwave cavity in a large superconducting magnet.

Sterile neutrinos ([26], [27]), light mass dark matter, and other particles are well-motivated and being studied, but will not be described in detail here. WIMPs were postulated early

on as a dark matter solution, and are probably the most-studied candidate. Following suit, the LUX detector is specifically tuned to search for WIMP dark matter. Due to the focus on WIMP dark matter, from now on this dissertation may use the terms WIMP, dark matter, and χ interchangeably.

Chapter 3

Detection of WIMP Dark Matter

3.1 Ways to Study Wimps

WIMPs may couple to Standard Model (SM) particles and result in the detectable phenomena of production, annihilation, or scattering. Subsequently, the study of dark matter particles (referred to as χ) can be categorized into three methods: production at colliders, indirect detection, and direct detection (see Figure 3.1). These three complementary approaches probe different areas of the WIMP parameter space and employ detection techniques both on Earth and out in space. Measurements are traditionally presented in a plot of WIMP mass versus WIMP-nucleon interaction cross section, with null results setting limit curves, carving out the parameter space in which WIMPs can exist, see Figures 3.5 and 9.2 for recent results.

Particle production occurs at colliders such as the Large Hadron Collider, where SM particles (protons in the case of the LHC) are accelerated to speeds high enough to create new particles upon collision. If such collisions reached energies significantly higher than the WIMP mass, WIMPs could be created. Since dark matter is expected to be weakly interacting, it won't be easily seen by detectors at the LHC, but it can still be identified by the missing energy and momentum seen in its interactions.

WIMPs may be their own anti-particle, allowing for self-annihilation. Indirect detection methods search for the photons or antiparticle excess that could be created in areas dense in dark matter. In particular, PAMELA (Reference [28]) and AMS (Reference [29]) have found surprising positron excesses in cosmic rays, which could in part be attributed to dark matter annihilations.

Should a dark matter halo made of WIMPs exist in the Milky Way, the Earth would be passing through a sea of WIMPs as it orbits and moves throughout the galaxy. Since WIMPs are weakly interacting, most dark matter would pass through the Earth unnoticed. However, even a tiny interaction cross section would eventually lead to recoils caused by WIMPs. Direct detection techniques set up and observe massive targets in terrestrial detectors, waiting for possible WIMP-target interactions. The LUX detector is designed for direct detection of dark matter, and so direct detection will be described more fully in the

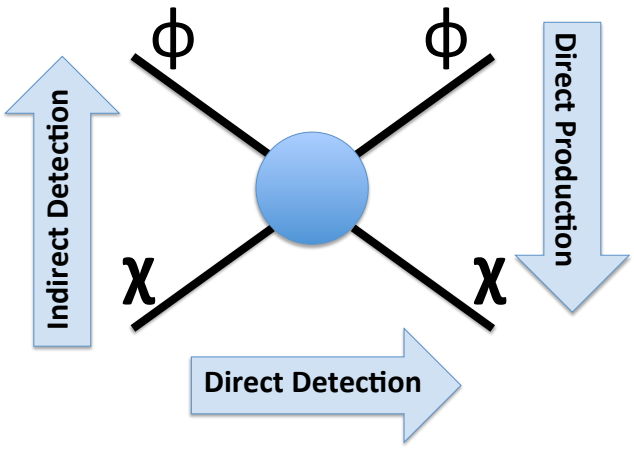

Figure 3.1: Methods for studying WIMPs. In indirect detection, dark matter particles (χ) self-annihilate and create observable Standard Model particles (ϕ). In direct production, two Standard Model particles combine in a high-energy collision to create dark matter. Direct detection searches for the effects of dark matter particles scattering off of Standard Model particles.

rest of this chapter.

3.2 Direct Detection of Dark Matter

The direct detection of dark matter depends on the coupling of dark matter particles to the nuclei of a detector's target material. Such interactions are expected to be rare, so great care must be taken to understand and reduce backgrounds that may muddle a WIMP signal. For this reason, dark matter detectors are typically deep underground, where the rock overburden shields against cosmic ray backgrounds. Detectors are also constructed and placed in radioactively clean environments, built with materials that are low in radioactivity. Semiconductor detectors and noble liquid detectors are the two primary detector types used to try and find energy depositions by WIMPs; bubble chambers are also used but to a lesser extent. Making detectors larger increases chances of interaction, so advancement in detector technology often involves scaling up the amount of target material. Tonne scale experiments are currently being developed.

3.2.1 Standard Halo Model of WIMPs

In order to study dark matter via direct detection, a set of assumptions must be made about dark matter locally and in our galaxy. Based on observations of other spiral galaxies, the Milky Way is expected to have its own spherical dark matter halo. In the Standard Halo Model (SHM), the Milky Way's dark matter halo is isothermal and isotropic and follows a density profile $\rho(r) \sim r^{-2}$. While greatly simplified, the SHM is adopted by most

cosmologists in dark matter rate and cross section calculations, and this standardization allows for easy comparison between different experiments and methods.

The dark matter density in our galaxy is estimated to be ~ 0.3 GeV cm^{-3} in the vicinity of the earth. The dark matter velocity is usually modeled as a Maxwell-Boltzmann distribution $f(v) \propto \exp(v^2/v_0^2)$, with characteristic velocity $v_0 = 220$ km s^{-1} and a velocity cutoff at the galaxy escape velocity $v_{esc} = 544$ km s^{-1}. The velocity is relative to the rest frame of the galactic halo. To utilize the distribution for terrestrial detectors, the movement of the earth within the galaxy can be taken into account with the transformation $\vec{v} \rightarrow \vec{v} + \vec{v_E}$, where $v_E = 232$ km s^{-1} is the velocity of the earth relative to the galactic halo.

The SHM suffers from some large uncertainties because it is difficult to measure the rotational properties of a galaxy from inside that galaxy. Other popular halo models have been developed, for example the Navarro/Frank/White profile [30] is based on careful observation and simulation, and may more accurately describe our galaxy. A better understanding of the distribution of dark matter near Earth will aid in interpretation of direct detection results, but conversely, direct detections could reveal the shape and distribution of the dark matter halo.

3.2.2 The WIMP Recoil Spectrum and Cross Section

More details on the following calculations can be found in the seminal paper by Lewin and Smith (Reference [31]). The astrophysical parameters described in the previous subsection can be taken together with detector target properties to calculate a differential scattering rate, wherein a WIMP scatters off a target particle. We start by defining the differential number density of WIMPs dn:

$$dn = n_0 f(\vec{v}, \vec{v_E}) d^3v \tag{3.1}$$

where f is the normalized velocity distribution function and $n_0 = \rho_0/m_\chi$ is the average WIMP number density. The event rate depends on the atomic mass of the target nucleus A, the WIMP-nucleon cross section σ, the WIMP density n, and velocity v, and is given by

$$dR = \frac{N_A}{A} \sigma \langle v \rangle dn \tag{3.2}$$

where N_A is Avogadro's number. Accounting for the dependence on the energy of a collision, we have the differential energy rate

$$\frac{dR}{dE_R} = \frac{N_A \, \rho_0}{A \, m_\chi} \int \frac{d\sigma}{dE_R} \, v \, f(\vec{v}, \vec{v_E}) \, d^3v, \tag{3.3}$$

which is typically expressed in terms of events kg^{-1} day^{-1} keV^{-1}, also known as the differential rate unit or dru.

The integral is bounded below by v_{min}, determined by scattering kinematics to produce minimal recoil energy E_{th}, a limitation imposed by detector threshold:

$$v_{min} = \sqrt{\frac{m_N \, E_{th}}{2 \, \mu_{N,\chi}^2}} \tag{3.4}$$

where m_N is the mass of the target nucleus and $\mu_{N,\chi} = \frac{m_\chi m_N}{m_\chi + m_N}$ is the reduced mass of the system. The integral's upper limit is normally taken to be the local galactic escape speed v_{esc}. As described in Section 3.2.1, dark matter velocities are usually modeled as a Maxwell-Boltzmann distribution, so $f(\vec{v}, \vec{v_E}) \propto \exp((\vec{v} - \vec{v_E})^2/v_0^2)$.

The WIMP-nucleus cross section is expressed as the product of the zero momentum cross section σ_0 and nuclear form factor F:

$$\frac{d\sigma}{dE_R} = \frac{m_N}{2\,\mu_{N,\chi}^2\,v^2}\,\sigma_0\,F^2(E_R) \tag{3.5}$$

The cross section can be broken down into spin-independent (SI) and spin-dependent (SD) components. Focusing on the SI component, we consider the total cross section as the sum of interaction couplings with the individual protons and neutrons within the nucleus. We're able to simplify by using the fact that the couplings to protons and neutrons, f_p and f_n, are approximately equal.

$$\sigma_0^{SI} = \frac{4\,\mu_{N,\chi}^2}{\pi}[Z\,f_p + (A - Z)\,f_n]^2 \approx \frac{4\,\mu_{N,\chi}^2}{\pi}\,A^2\,f^2. \tag{3.6}$$

The cross section in Equation 3.6 is for a WIMP interacting with the entire target nucleus. Since different experiments use different target materials, a WIMP-nucle*on* cross section σ_n is more appropriate for comparison, and can be related to σ_0^{SI}:

$$\sigma_0^{SI} = \frac{\mu_{N,\chi}^2}{\mu_{n,\chi}^2}\,A^2\,\sigma_n \tag{3.7}$$

where $\mu_{n,\chi}$ is the reduced mass of a WIMP-nucleon scatter.

With the components of Equation 3.3 characterized, it can now be expressed as

$$\frac{dR}{dE_R} = \frac{1}{2}\frac{\rho_0\,A^2\,\sigma_n}{m_\chi\,\mu_{n,\chi}^2}\int_{v_{min}}^{v_{esc}} F^2(E_R)\,\frac{f(\vec{v})}{v}\,d^3v. \tag{3.8}$$

The important takeaway from this expression is that due to the A^2 dependence, interaction rates will be higher for heavier target nuclei. Also of importance is the form factor F, where usage of the Helm form factor (Reference [33]) is standard. These form factors typically decrease for larger recoil energies, and also account for loss of coherence when the deBroglie wavelength of the incoming WIMP becomes comparable to the size of the target nucleus. Equation 3.8 can be numerically integrated for various targets, allowing for predictions of rates as a function of recoil energy (see Figure 3.2).

3.2.3 Direct Detection Channels

Figure 3.3 shows some direct detection experiments and the detection channels utilized by each. Direct detection experiments identify scattering of WIMPs of targets through the

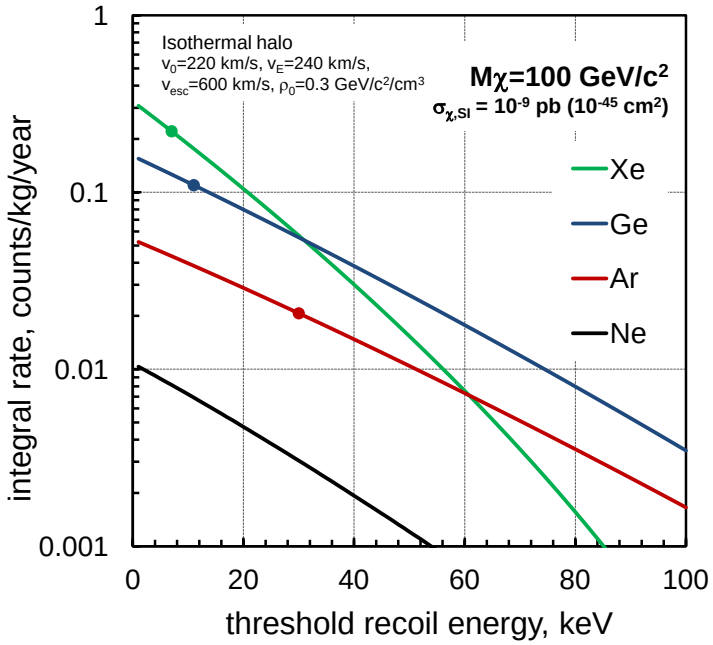

Figure 3.2: WIMP scattering rates as a function of energy threshold for different targets. Notable features: Larger target nuclei (larger atomic mass) generally lead to larger interaction rates. However, larger nuclei also cause sharper declines in rates at higher recoil energies due to their nuclear form factor. Perfect energy resolution and detection efficiency assumed, halo and WIMP parameters as listed, figure from Reference [32].

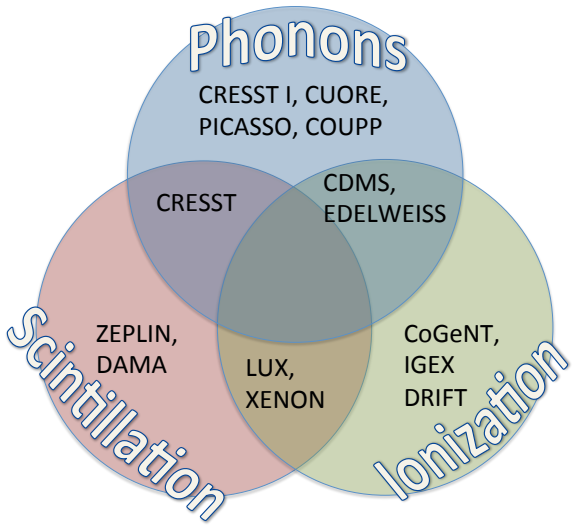

Figure 3.3: Direct detection channels, sample of experiments utilizing one or more channels.

detection channels of scintillation, ionization, and phonons/heat deposition. *Scintillation* occurs when a recoil excites electrons, resulting in the emission of light when the electrons return to lower energy states, and is the process underlying the ZEPLIN-I experiment (Reference [34]). When the target receives enough energy to be stripped of electrons, *ionization* occurs, as utilized in CoGeNT (Reference [35]). Phonons can be measured when energy is deposited that causes a change in temperature or phase, detectable by a crystal (CRESST [36]) or bubble chamber (COUPP [37], PICASSO [38]).

Most experiments will utilize multiple detection channels, helping to more fully capture the nature of the type of recoil. WIMPs are expected to interact via the nuclear weak force with nuclei, while most other background radiation will interact via the electromagnetic force with electrons. Being able to distinguish between nuclear and electron recoils enhances background rejection, and using more than one detection channel allows for better discrimination. LUX, ZEPLIN-II [39], and XENON100 [40] are liquid noble detectors that identify recoils through scintillation and ionization. CDMS [41] and EDELWEISS [42] measure ionization and phonons in cryogenic germanium detectors.

Annual Modulation

Annual modulation offers a unique way to look for WIMPs. Instead of depending on the distinction between nuclear and electron recoils, annual modulation uses the motion of the Earth through the WIMP sea to determine a WIMP signal. As the solar system orbits about the Milky Way center, it moves through the dark matter halo, creating a "WIMP wind" of ~ 220 km s^{-1}. The magnitude and direction of this wind affects the expected rate of WIMP interactions on Earth, as seen in Section 3.2.2. The orbit of the Earth around the sun adds another component to the detector's motion through the WIMP wind. When the earth's velocity has a component that is opposite the direction of the WIMP wind, a WIMP "headwind" results, increasing the flux of WIMPs incident upon the detector. Similarly, when the earth and wind share velocity components in the same direction, a tailwind and reduced flux results. This means that WIMP rates in terrestrial detectors should experience an *annual modulation*, a yearly periodic variation, which is maximal in June and minimal in December. Observing a modulation with these properties could be interpreted as a signal originating from WIMPs.

3.2.4 Current State

DAMA/LIBRA [43] has observed an annual modulation as described above (see Figure 3.4). Together with its predecessor, DAMA/NaI, data from 13 annual cycles has been collected. The experiment utilizes NaI crystals as its detection medium and measures scintillation light and its modulation, rather than using multiple detection channels or pulse shape discrimination to identify nuclear recoils over electron recoils. The modulation signal appears in a low-energy recoil bin, has been interpreted as evidence for low-mass (~ 10 GeV) WIMPs.

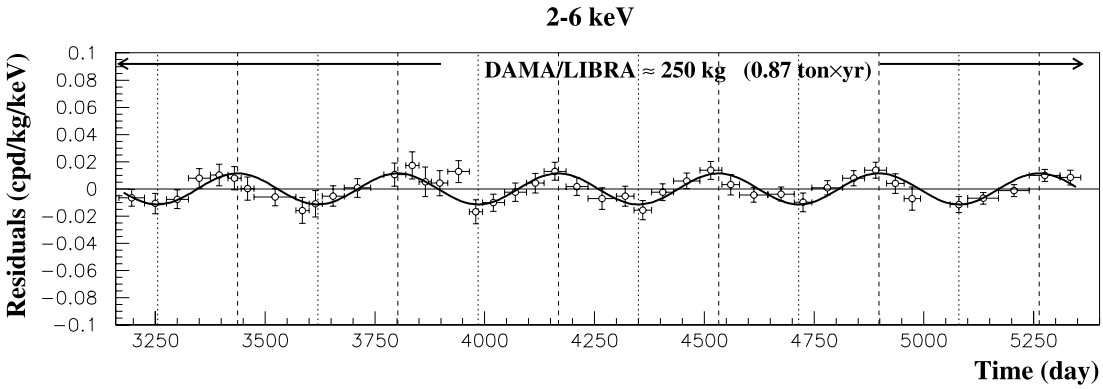

Figure 3.4: DAMA/LIBRA annual modulation. Figure from Reference [43].

This potential discovery is the source of considerable tension in the field of dark matter searches (References [44], [45], [46], [47], [48], [49]). CoGeNT, utilizing a point-contact germanium detector, had also observed an annual modulation with ionization charge, again through a single channel ([50]), though subsequent analysis did not reproduce a significant modulation. LUX and XENON have excluded the WIMP parameter space favored by the DAMA/LIBRA, indicating either that WIMPs couple differently to NaI than to xenon, or that the modulation is caused by some unknown, non-WIMP background. CRESST and CDMS also found evidence for possible low-mass WIMPs, but as the observations were at energies near the detector thresholds, the signals could instead be attributed to unfamiliar background radiation, and the phenomenom was never deemed a significant signal. Figure 3.5 displays the low-mass WIMP region containing the contradictory results, with limit curves drawn for experiments without WIMP observations, and favored region contours for experiments with potential discoveries.

Recall how it is important to study dark matter through production, indirect detection, and direct detection. In the same way, within direct detection, it is important to utilize many different detection methods, materials, and locations. The usage of semiconductors and liquid nobles are truly complementary. Semiconductors excel in energy resolution, thresholds, and discrimination. Liquid nobles can be scaled up easily, offering a simple way to increase exposure.

It is also important to have redundancies in experiments as a check for reproducibility. In particular, a check on the DAMA/LIBRA modulation using the same detector material would help to interpret the observed modulation. Such an effort is currently underway with DM-ICE (Reference [51]), where NaI detectors are deployed in the southern hemisphere. If the annual modulation observed by DAMA/LIBRA is caused by dark matter, the phase should be the same in both northern and southern hemisphere. If instead it was caused by other seasonal effects, the modulations would appear out of phase, since the seasons on opposite hemispheres are inverted.

There is currently considerable experimental effort to try and directly detect dark matter. The current status is a feeling of excitement - there are many experiments at play, and all

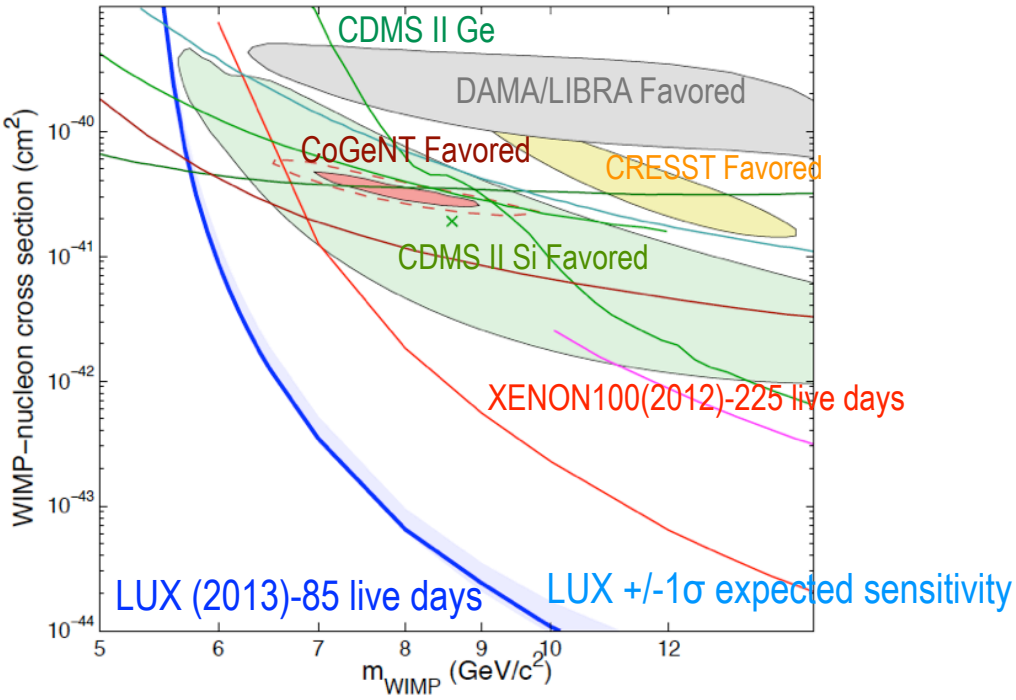

Figure 3.5: Tension between WIMP discovery and limits. Limit curves are displayed for LUX(2013) and XENON100(2012), no WIMPs observed. Contours are drawn for potential discoveries, most notably the annual modulation signals from DAMA/LIBRA and CoGeNT. Signals from CDMS II Si and CRESST have been walked back, and probably result from backgrounds. The discovery regions occupy a space excluded by the LUX/XENON results, and has been the subject of considerable controversy.

	Atomic Number Z	Atomic Mass A	Boiling Point at 1 atm [K]	ρ at BP [g cm^{-3}]	Scintillation λ [nm]
Ne	10	20	27.1	1.21	85
Ar	18	40	87.3	1.40	125
Kr	36	84	119.8	2.41	150
Xe	54	131	165.0	3.06	175

Table 3.1: Properties of noble gases for dark matter detection.

are pushing their technologies further to try to be among the first to discover dark matter. There is also a bit of frustration, with confusion arising from conflicting results, and decades-long searches still coming up empty. The general sentiment is that no WIMPs have yet been found, and as experiments get more sensitive, more of the potential WIMP parameter space gets ruled out. As the parameter space for WIMPs shrinks, so does the case for the supersymmetric LSP being the explanation for dark matter – but more worlds have opened up as physicists look more deeply into the model assumptions made in both the galactic dark matter halo and the particle interactions between WIMP and nuclei. A change to the model assumptions could lead to larger changes in predicted rates. With so little known still about dark matter, there remains a great incentive to keep exploring and keep pushing detector limits.

3.3 Noble Gas Detectors: Xenon

The usage of noble liquids has one major advantage in WIMP search detectors: scalability. But there are a variety of other properties that make noble liquids an ideal detection medium, and some specific to xenon will be described here. Xenon has a large atomic mass with 131 nucleons in its dominant isotope, which enhances interaction rates as shown in Subsection 3.2.2. As a noble element, xenon is chemically non reactive and will not bond with other potentially radioactive materials, helping to keep backgrounds low. With xenon's boiling point at 165K, it can be liquefied with relatively easy cryogenics, achieved with liquid nitrogen. A dense target is created when liquefied, allowing large detector masses to fit in reasonably sized vessels. Properties of other noble gases that can be used as detection media are listed in Table 3.1.

Much of the power of using xenon comes from its recoil discrimination properties. An incoming particle can interact with xenon via electron or nuclear recoil. In electron recoils (ER), an incoming gamma or electron manages to eject a bound electron from a xenon atom. This ejected electron interacts with nearby xenon atoms, losing energy along its track until it eventually stops. Nuclear recoils (NR) behave in a similar fashion, but are usually caused by a neutron (or WIMP) that causes the xenon nucleus to recoil (instead of the electron). The length of the track, electron or nuclear, depends on the stopping power dE/dx of the xenon. Stopping power is higher for nuclear recoils since more energy of the recoiling nucleus is lost with each interaction, and so nuclear tracks are usually shorter and denser than

electron tracks. The nature of the recoil (nuclear or electron) will manifest itself in other ways as well. The affected xenon atoms can either be ionized (Xe^+) or excited to a higher electron state (Xe^*). An excitation caused by a NR will populate triplet and singlet electron levels differently than an ER, and the de-excitations will occur with different timescales and observed pulse shapes. This makes *pulse shape analysis* one way of distinguishing between ER and NR.

A far more powerful method for xenon detectors is to use the ratio of ionization to scintillation, the *charge to light ratio*, for NR/ER discrimination. When excited Xe^* decays and emits photons, the photons tends to diffuse within the detector. However, the addition of another Xe atom can create the excimer (excited dimer) Xe_2^* which can also decay and scintillate:

$$\begin{aligned} Xe^* + Xe &\rightarrow Xe_2^* \\ Xe_2^* &\rightarrow 2Xe + h\nu \end{aligned} \tag{3.9}$$

The photon ν resulting from this process is 175 nm and observed as *prompt* or *primary scintillation*, denoted S1. This photon will travel freely through the detector medium without danger of being absorbed or re-emitted because it corresponds to energy levels of the Xe_2 dimer, and won't match the energy levels of the single Xe atoms that make up most of the detector. This highlights another desirable property of xenon detectors: they are transparent to their own scintillation light, so with careful design, most of the light from a recoil event can be reliably collected.

The ionized atoms Xe^+ can also contribute to the prompt scintillation through the process:

$$\begin{aligned} Xe^+ + Xe &\rightarrow Xe_2^+ \\ Xe_2^+ + e^- &\rightarrow Xe^{**} + Xe \\ Xe^{**} &\rightarrow Xe^* \text{ (vibrational de-excitation, no light emitted)} \\ Xe^* + Xe &\rightarrow Xe_2^* \\ Xe_2^* &\rightarrow 2Xe + h\nu \end{aligned} \tag{3.10}$$

However, an electric field can be used to suppress the above process by drifting ionization electrons away from the recoil site. The drifted electrons can then be collected and measured to determine recoil properties. In the LUX detector the drifted electrons are manifested as a *secondary scintillation* S2. More details about LUX's operation as a dual-phase time projection chamber will be detailed in the next chapter. See Figure 3.6 for diagram depicting the xenon scintillation process.

Some of the energy from the recoil will be also lost to heat, which does not produce a detectable signature in the detector. Thus, the energy of a recoil can be partitioned into heat, ionization, and excitation channels, and the distribution between these partitions will differ between electron and nuclear recoils. Because NRs lose more energy to heat than ERs, two different energy scales are used to describe *observed* recoil energies, keV_{nr} and keV_{ee},

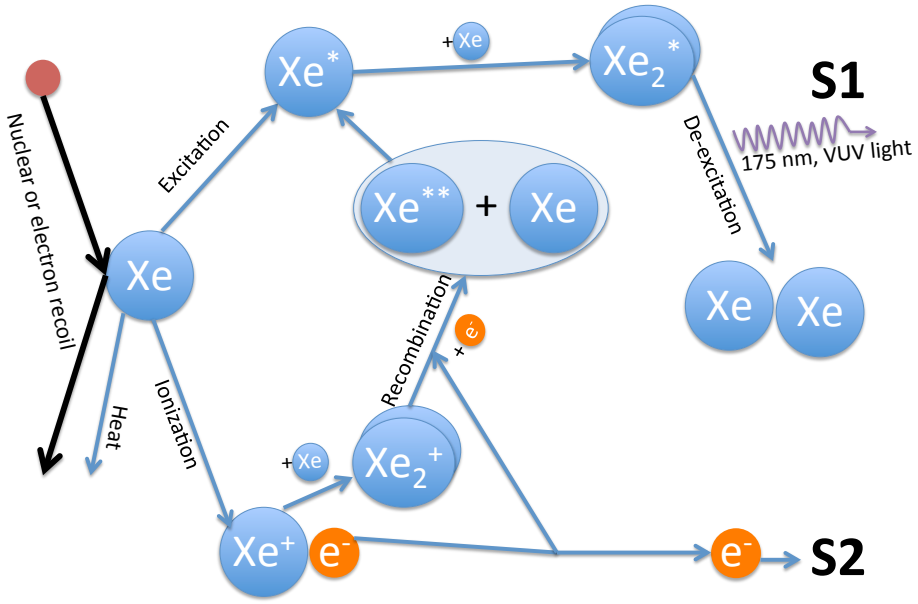

Figure 3.6: Xenon recoil process. Energy is initially partitioned into the three channels of heat, ionization and excitation, in differing proportions for ER and NR. Scintillation light is produced by the de-excitation of the Xe_2^* excimer. Ionized Xe^+ can also contribute to this scintillation through recombination with ionized electrons, unless the electrons are drifted away by an electric field.

with subscript *nr* denoting nuclear recoils and *ee* denoting electron equivalents. In order to determine correct comparisons between ER and NR energies, careful calibrations must be performed.

For a more comprehensive review of detectors or scintillation detectors specifically, refer to References [52] and [53]. A deep dive into noble gas detectors can be found in the authoritative Reference [54]. The next chapter will describe the LUX experiment, including more specifics on the operating principles behind the detector.

Chapter 4

The LUX Detector

The Large Underground Xenon (LUX) detector is a 370-kg dual-phase (gas and liquid) time projection chamber that uses the scintillation of xenon gas and liquid to identify particle interactions. The LUX detector has been specifically tuned for the search of dark matter interactions. This chapter will go over the detector design, details of which can also be found in Reference [55].

The detector is located 4850 feet underground in the Davis Campus of the Sanford Underground Research Facility (SURF), at the same site where Ray Davis' solar neutrino experiment took place (Reference [56]). The facility has been repurposed from the former Homestake gold mine, and is located in the town of Lead, South Dakota. The underground placement is crucial for a rare event search, as the rock overburden greatly reduces the background radiation caused by cosmic rays. Reference [57] provides a thorough overview of the facility.

4.1 A Dual-phase Time Projection Chamber

The primary component of the LUX detector is a large volume of liquid xenon, where incident radiation interacts with xenon atoms. A layer of gaseous xenon sits atop the liquid volume and is also utilized, making the detector *dual-phase*, with both the gas and liquid phases present and critical for particle identification. LUX identifies incident radiation through scintillation and ionization channels as described in Section 3.3. A recoiling electron or nucleus will create primary scintillation light, also known as S1, in the large liquid xenon target volume, which is detected by photomultiplier tube (PMT) arrays above and below the active detector region. The recoil also produces ionization electrons, which are drifted with a relatively weak electric field up to the liquid xenon surface. A strong electric field concentrated about the gas-liquid interface extracts the ionization electrons from the liquid to the gas phase of the detector, where scintillation light (referred to as S2 for secondary scintillation) is created in the gas and also detected by the top and bottom PMT arrays. Thus two light signatures are created for an interaction, with S1 light being a measure of the excitons created by the recoil, and S2 a measure of the ionization.

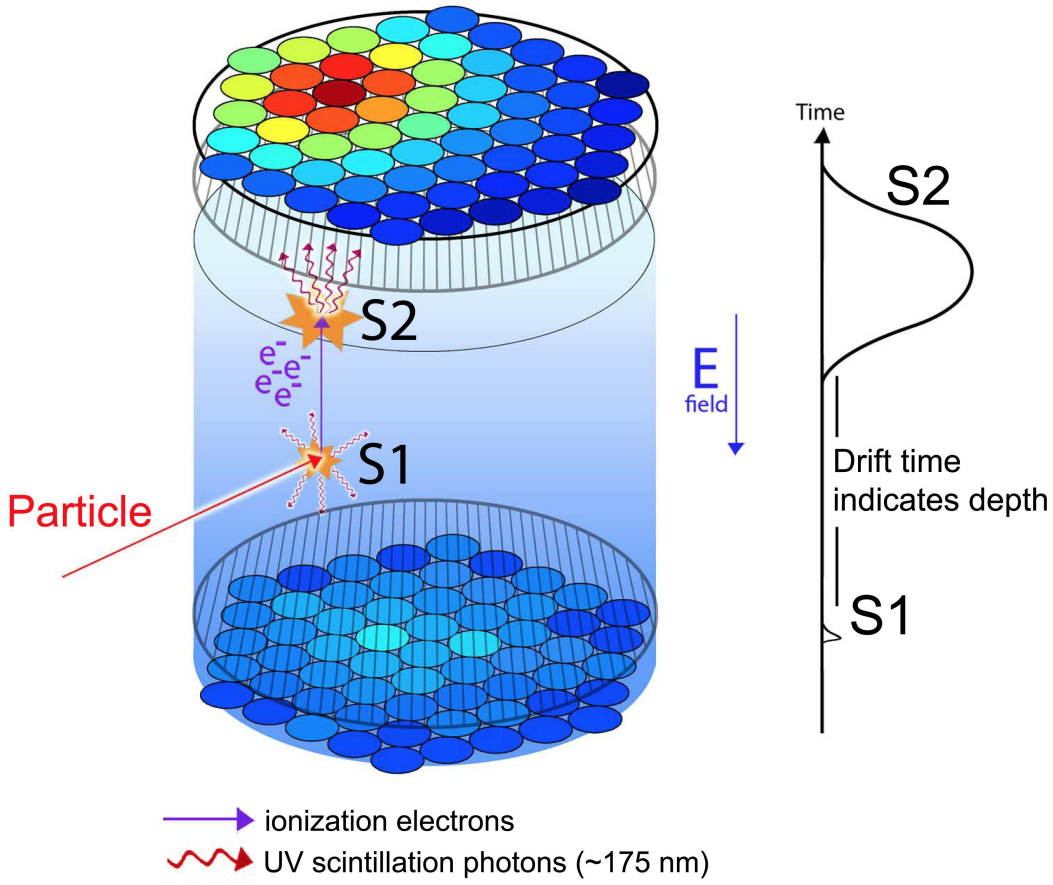

Figure 4.1: LUX: a dual-phase time projection chamber. S1 light is detected immediately upon an interaction within the detector, while S2 appears after ionization electrons have been drifted and extracted into the gaseous xenon region. Depth can be extrapolated from the difference between S1 and S2 times (drift time), while x-y position can be determined through the intensity distributions of readings in the arrays of PMTs.

S1 light is created immediately upon an interaction and will be detected by the PMTs at essentially the same time as the interaction. S2 light is created afterwards due to the time it takes to drift ionization electrons from the recoil site to the extraction region. The duration of this journey depends on the electric field strength, electron mobility in xenon, and of course, the depth at which the interaction occurred: further down the detector makes for a longer drift time. Subsequently, the timing between associated S1 and S2 signals can be used to extrapolate a z-position of the interaction within the detector. This position reconstruction from time is one of the hallmarks of a *time-projection chamber* (TPC), a novel detector design invented by David Nygren in 1974 (Reference [58]). Since they are drifted vertically, the ionization electrons will be extracted at the same $x - y$ position as the interaction site. PMTs closer to the extraction site will collect more photons than PMTs further away, creating a hit map that is more intense around the $x - y$ position of the extraction and allowing for measurements of the $x - y$ position of the recoil. Drift time together with PMT hit maps achieve full 3-D position reconstruction of an interaction within the detector.

Figure 4.1 shows S1-S2 creation within the detector together with the associated light pulses observed, and illustrates the 3-D reconstruction of event position. With this basic picture of the detection principle behind LUX, some context is provided for the description of the detector components that occurs in the next section. More applications of the detection principles will be presented afterwards.

4.2 LUX Detector Components

At its core, the idea behind the LUX detector is very simple: it is a giant vat of liquid xenon. However, many components must come together to keep the detector running smoothly. Figure 4.2 features a diagram of some of the components.

Care must be taken to regulate the temperature of the detector so that xenon remains in a liquid state. A thermosyphon cooling system was developed (Reference [59]) to continuously cool the detector using the gas and liquid phases of nitrogen. The detector also consists of two cylindrical titanium vessels, with the inner cryostat containing the liquid xenon, and a vacuum insulated layer between the inner and outer cryostats. A number of sensors measuring pressure, temperature, and liquid levels are placed throughout the detector internals to monitor and help maintain appropriate conditions.

A circulation system continuously pumps xenon in and out of the inner cryostat. The xenon is passed through a hot getter that purifies the xenon, ridding it of electronegative (non-noble) impurities. If left in the detector, these impurities shorten the *electron lifetime* within the detector, the time it takes for a free electron to recombine. Long electron lifetimes are preferable to preserve the ionization electrons that result from a recoil. As they get drifted up to create S2, some of these electrons will get lost by combining with impurities, with interactions occurring nearer the bottom of the detector losing more electrons. Impurities may be introduced by leaks or outgassing of components within the detector, so constant purification combats this and keeps S2 signals true to their origins. The circulation path

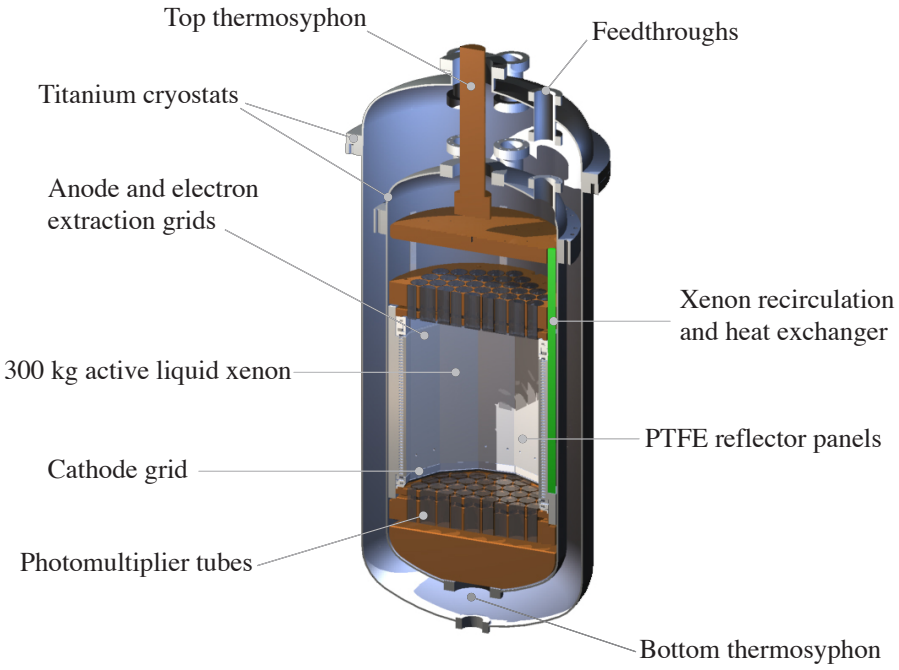

Figure 4.2: Internal view of LUX components. From Reference [55].

also has inlets that allow for calibrations by purposefully injecting radioactive sources into the stream. Samples of xenon can be taken from circulation outlets to measure impurities (Reference [60]).

Within the inner cryostat, polytetrafluoroethylene (PTFE) panels are arranged in a do-decagonal structure around the active region. The panels reflect scintillation light, allowing for 99% efficiency in light collection. By retaining as many scintillation photons as possible, the detector can more accurately measure energy depositions within the detector.

Four copper pieces span the horizontal cross section of the inner cryostat. Two of them are the top and bottom PMT holders, which establish the detector active region in between. The other two flank the top and bottom of the inner cryostat and act as radiation shields as well as large thermal masses that regulate temperature via the thermosyphon system.

4.2.1 Grids and Electric Fields

Electric fields are required to drift and extract ionization electrons for the creation of S2. Fields are created using a series of stainless steel wire grids that stretch across the detector area horizontally, as seen in Figure 4.3. The topmost and bottommost grids serve as PMT shields, regulating fields near the PMTs (which are biased at ~ -1.4 kV) so as not to affect their gains. Ionization electrons are initially drifted upward toward the gate grid, in the

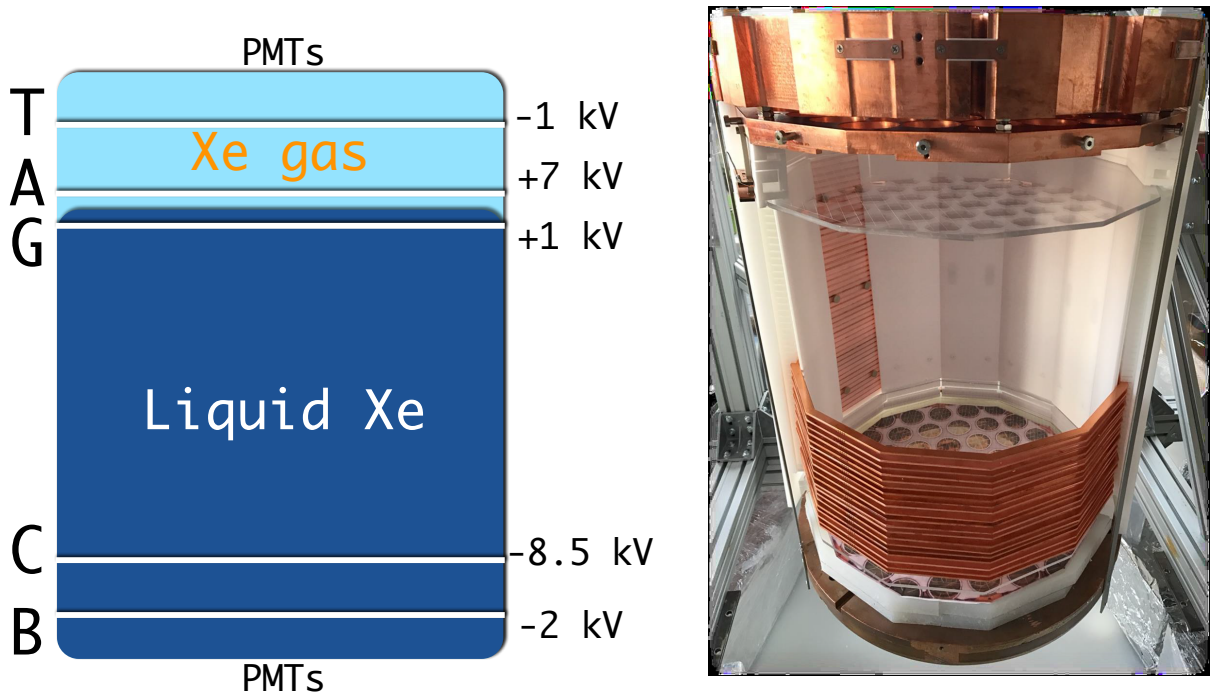

Figure 4.3: Grid arrangement and field-shaping rings. Left: arrangement of grids within cryostat containing liquid and gaseous xenon. Grids from top to bottom: top PMT shield, anode, gate, cathode, bottom PMT shield. The liquid-gas interface lies halfway between anode and gate. Right: construction of copper field-shaping rings, stacked vertically to surround the active region.

drift region between cathode and gate, a distance of 48 cm. The *extraction region* is the 1 cm high detector slice that straddles the liquid surface, and lies between the gate and anode grids. A relatively strong field is required in this region to extract electrons and create S2 in the gas.

To help keep electric fields vertical, 47 copper field shaping rings encircle the detector active region from cathode to gate. Rings are connected by a chain of resistors that determine the electric potential of each ring (and consequently, of each corresponding height), from cathode to gate. A picture of the construction of the field-shaping rings is shown in Figure 4.3; in the finished product the rings are sandwiched between ultra-high molecular weight polyethylene (UHMWPE) panels.

The operating grid voltages for LUX Run04 (which corresponds to the data used in this dissertation) were -1 kV and -2 kV for the top and bottom PMT shields respectively, +7 kV for the anode, +1 kV for the gate, and -8.5 kV for the cathode. The resulting electric fields in the regions between the grids are listed in Table 4.1. Of particular importance is the field between gate and liquid surface, 3.684 kV/cm. This field determines the electron extraction efficiency, with stronger fields better able to overcome the work function binding electrons to the liquid. Extraction starts to occur at a field strength of 1.75 kV/cm, with full extraction achieved at 5 kV/cm. At LUX's Run04 operating voltages, $\sim$ 75% extraction

Region	Electric field [kV cm^{-1}]
Top PMT array to Top PMT shield	0.605
Anode to Top PMT shield	2.081
Liquid surface to Anode	-7.213
Gate to Liquid surface	-3.684
Cathode to Gate	-0.208
Bottom PMT shield to Cathode	1.592
Bottom PMT array to Bottom PMT shield	0.620

Table 4.1: Electric fields in bulk detector regions (Reference [63]).

efficiency is achieved (References [61],[62]), which is taken into account when reconstructing energies from S2 emissions. The partial extraction also leads to anomalous electron emissions due to the buildup of unextracted electrons on the liquid surface. While a nuisance, most of these are easily distinguishable from typical S2 signals and can be eliminated or considered in post-processing as the analyst desires.

Grid High Voltage

The task of supplying voltage to the grids highlights the challenges of accessing the detector internals while operational. The detector is kept over 100° below room temperature, and xenon must be contained and well separated from the air to avoid contamination by radioactive and electronegative agents. Furthermore, the detector cryostats are submerged underwater within the LUX water tank, which serves as an active shield. Cabling for supplying power and reading out instrumentation is passed through three feedthroughs in the cryostats, passing from inside the detector through conduits into the *breakout cart*, which abides in the laboratory above the water tank (see Figure 6.1 for a rendering). The breakout cart is at room temperature and connects an enclosed space containing xenon gas and internal cabling to the front-end electronics of the outside environment - it is where the instrumentation and power cables "break out" of the protected xenon space. To prevent air leakage into the xenon space, cart components were constructed using with pieces utilizing ConFlat (CF) flanges. ConFlat achieves an ultra-high vacuum seal, so leak-tight connections protect the xenon from impurities. CF feedthroughs then allow for connections to the outside.

The following journey applies to the top, anode, gate, and bottom grids. Figure 4.4 displays corresponding pictures. The cathode was intended to operate at an extremely high voltage, so its design required more precautions regarding safety and arc prevention, and aren't included in this grid high voltage chain description.

The grids' connection to the outside starts with a connector that inserts into the stainless steel grid frames. The connector is also soldered to the internal grid cable, GORE F01A070 wire rated to 9 kV DC (see Figure 4.4a). The wire consists of a central conductor and a

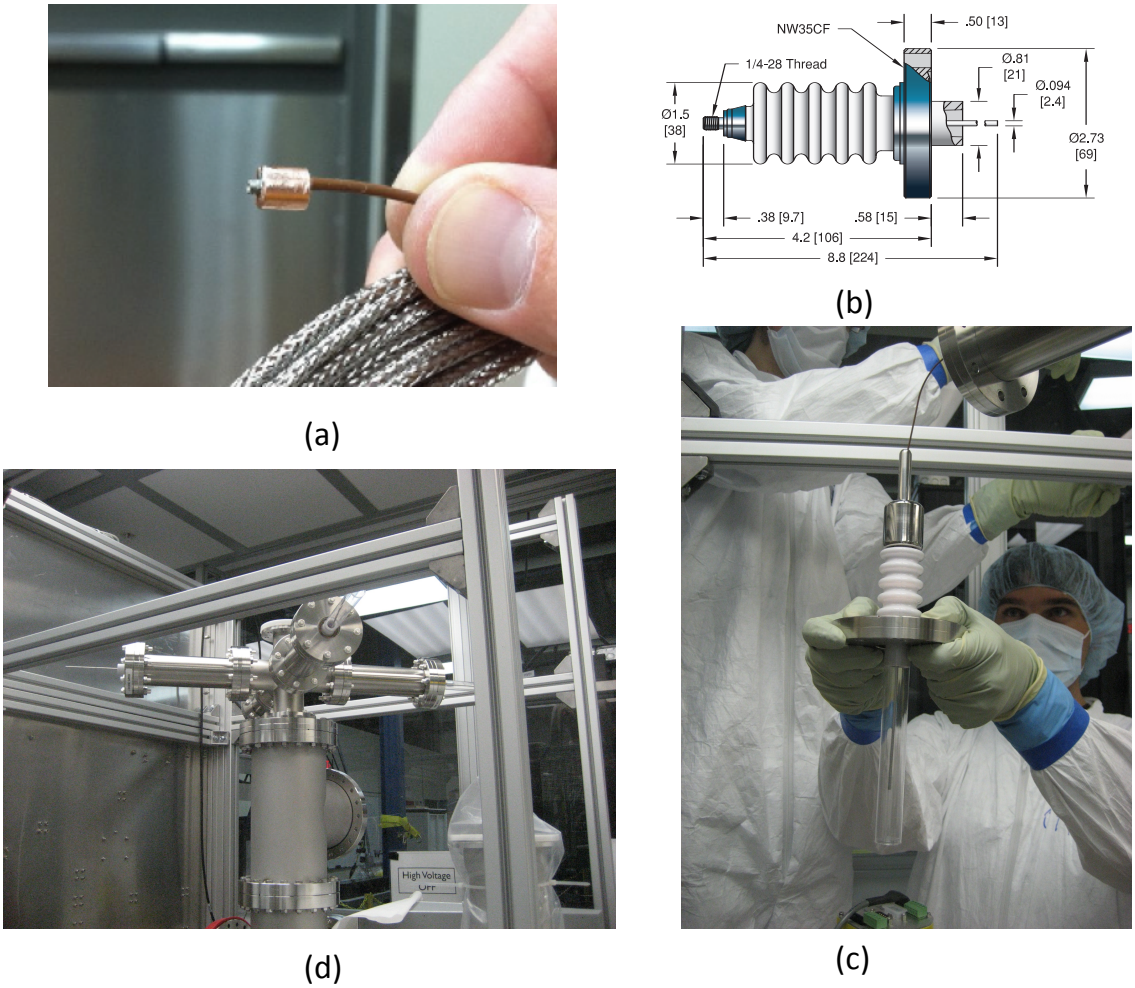

Figure 4.4: LUX grid HV components. The copper barrel in (a) is attached to the high voltage GORE internal cable, and inserts into the grid frames to form an electrical connection. The CeramTec ceramic standoff is displayed in (b) with dimensions labeled in inches, and in (c) it is shown during construction. The "chopper" configuration on top of the breakout cart structure separates the four HV connections for the four grids to prevent sparking.

Teflon dielectric. Each cable has been covered with a stainless steel braid shield.

The four grid cables snake through the detector and conduits up to the breakout cart. Still within the xenon space in the breakout cart, the cables are clamped to a strain relief mechanism as they go through an 8-inch ConFlat nipple. Then they are split into four different arms of a CF cross, separating the four high voltage (HV) connections to safeguard against sparking (see structure on top of breakout cart in Figure 4.4d). The breakdown voltage in xenon is much lower than that of air, so electrical breakdown inside the xenon space is a valid concern, and the "chopper" design separating the HV connections is the result of many HV tests and design iterations.

The grid cables are each then connected to a CeramTec fluted ceramic standoff 22973-01-CF, a high voltage feedthrough welded in a CF flange. The feedthroughs were special ordered, reverse-welded so that the fluted ceramic is on the vacuum/xenon side of the flange rather than the air side (see Figure 4.4b/c).

The feedthroughs are the grids' interface between xenon space and the outside world. On the air side, HV filter boxes are mounted directly to the feedthrough flanges and connect to the CeramTec air-side connectors. The boxes provide filtering and monitoring circuits, as well as SHV-10 connections to accept power from the HV power supplies. Low-smoke HV cables were special made from Reynolds 167-2669 cable, as fire safety must always be respected when working deep underground. These connect the HV filter boxes to the power supplies: two SRS PS365 +10 kV supplies and two SRS PS350 ±5 kV supplies. The supplies are mounted in the LUX electronics rack, which lives right next to the breakout cart and houses the equipment necessary to power and read out all the instrumentation inside the detector. See Figure 4.5 for a sketch of the grid HV system.

4.2.2 PMTs

The scintillation light from interactions within the detector is read out by 122 Hammamatsu R8778 PMTs. The PMTs are arranged in two arrays of 61, looking in on the active detector region from above and below (see Figure 4.6). The manufacturer specifically used low-radioactivity components to build the PMTs, which is important for LUX as a rare-event search; backgrounds must be reduced as much as possible, especially for internal detector components such as the PMTs. Screening took place to quantify the PMT radioactivity (Reference [64]), and by design, the PMTs are the dominant source of radioactivity inside the detector. All other internal components were carefully chosen to contribute backgrounds that are subdominant to PMT activity.

The PMTs were also chosen for their sensitivity to xenon scintillation, with 33% quantum efficiency (QE) for 175 nm light. Scintillation photons are converted into a readable electrical signal through the photoelectric effect and charge multiplication through a series of dynodes.

High light output signals can cause saturation effects. The output current of the PMT is usually proportional to the incident light, but if too many electrons are created at later stages, nonlinearities can arise due to their repulsive field. This typically occurs at the anode, after many stages of electron multiplication have occurred. Anode saturation depends on

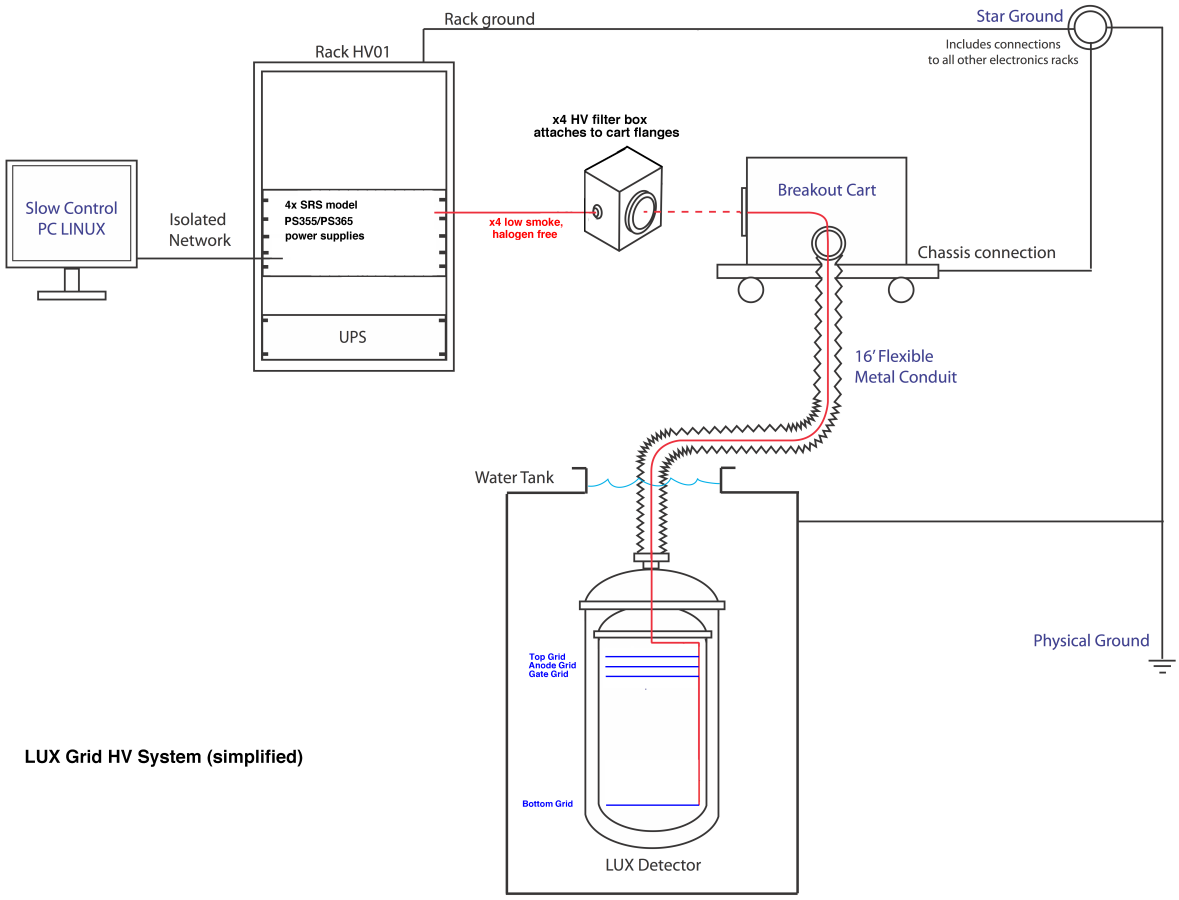

Figure 4.5: LUX grid HV system. For top, anode, gate, and bottom grids only.

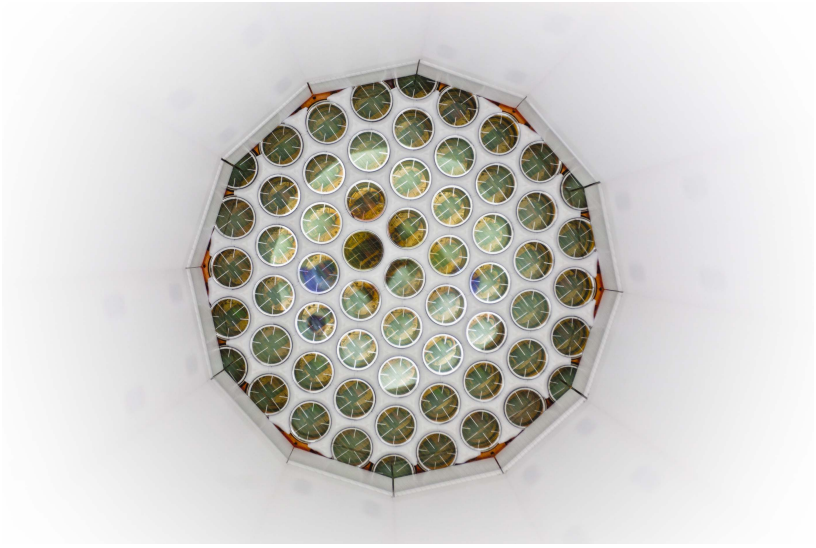

Figure 4.6: Bottom up view of top PMT array. Photo courtesy of Matt Kapust.

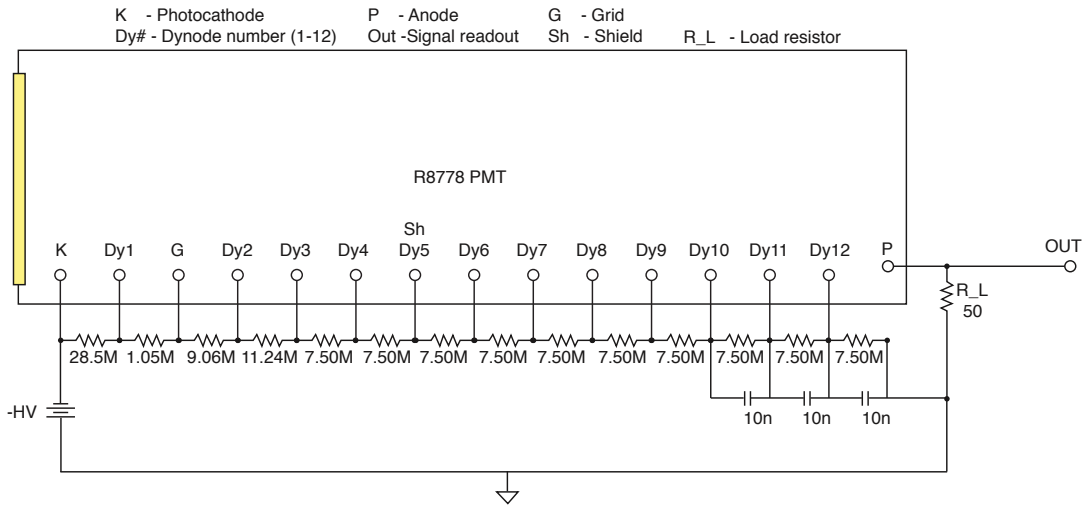

Figure 4.7: Circuit diagram for the LUX PMT base. 10 nF capacitors are placed across the last 3 dynode stages to provide reserve charge for large signals. Figure from Reference [65].

the instantaneous value of the output current. The anode is fully saturated when output signal cannot increase in size at all and may appear as a large pulse signals that "flatlines" at the point of anode saturation.

Since PMTs output current, a large output signal can counteract the bias current that powers multiplication in the last stage dynodes, decreasing or completely stopping the multiplication process. Decoupling capacitors are used to combat this by providing reserve charge to the last stages of multiplication, and are added to the last 3 dynodes of LUX PMTs (see Figure 4.7). However, the capacitors may be insufficient for especially bright signals and start to show saturation effects (a decrease in signal caused within the PMT). Capacitor depletion can also be an issue for high-rate data, if capacitors don't have sufficient time to recharge between consecutive pulses. Saturation effects are mentioned here because they become very apparent in signals generated by throughgoing muons, the subject of the next part, and will be referenced again in Section 7.2.

The PMTs the windows to all the signals coming from within the detector, making them the most crucial of detector components in terms of obtaining an interpretable signal. LUX PMTs are described in great detail in Reference [65].

4.3 Background Mitigation

As mentioned before, LUX is a rare-event search, and reducing and understanding backgrounds is of utmost importance. LUX's location deep underground shields it from most of cosmic rays that bombard the surface of the earth. Radioactivity from the rock and cavern walls surrounding the detector is mitigated by the LUX water tank, which is the focus of

Chapter 6.

The shields of water and earth address most external backgrounds, so now the worry turns to internal backgrounds, or the intrinsic radioactivity of the detector components themselves. As mentioned in Section 4.2.2, PMT radioactivity is expected to be the dominant background source of γ's and neutrons from within the detector. PMT radioactivity was carefully measured in order to understand what type of background signals to expect, and similar counting campaigns were carried out for all internal detector components. The detector was assembled in a clean room environment to prevent contamination, and low-radioactivity materials were chosen to construct LUX. While xenon itself has few worrisome radioactive isotopes, commercially available xenon usually includes trace amounts of air, including the noble radioactive isotope ^{85}Kr. If untreated, these impurities would be the dominant background in the detector. Prior to WIMP search and filling the detector with xenon, krypton levels were reduced from 130 ppb down to 3.5 ppt using a charcoal column chromatography technique to separate out the unwanted elements (Reference [66]). During detector operation, the xenon undergoes continuous purification from non-noble impurities via circulation through a getter.

One of advantages of using liquid xenon as a detector medium is its relatively high density and its *self-shielding* properties. The outer layers of the xenon volume act as a shield, leaving the center radioactively quiet. Since the detector reconstructs the 3-D positions of interactions, a *fiducial volume* in the shielded center can be selected as the region of interest for WIMP search. Figure 4.8 displays the measured and predicted activity levels in the detector as a function of position. Most interactions occur near the edges (the shield), and few events penetrate to the center of the detector (the fiducial volume). By only considering events from this dull region in the center, there is less chance for a background event to be mistaken as a WIMP.

A thorough study and simulation of radiogenic backgrounds in LUX has been conducted (Reference [67], also [68]). A comprehensive background model is needed to interpret results and to identify WIMP signals (or lack thereof). The process of searching for an unknown particle requires that everything that is "known" is understood extremely well.

Since WIMPs will cause nuclear recoils, and most backgrounds are expected to produce electron recoils, ER/NR discrimination is one of the most powerful tools used for identifying backgrounds. The next section will further expand on this concept.

4.4 ER/NR Discrimination

As described in Section 3.3, nuclear and electron recoils will partition their energy differently between the channels of heat, excitation, and ionization. The ratio of an event's two scintillations (S2/S1) holds the key to distinguishing between nuclear and electron recoils. This difference is typically depicted in a plot of $S1$ light vs $\log_{10}(S2/S1)$ (see Figure 4.9). Two distinct bands appear, with one corresponding to ER and the other to NR. Extensive calibrations were performed using sources of known energy and radiation type. Tritiated methane (CH_3T) was injected into the detector (see Reference [70]) to observe tritium β-

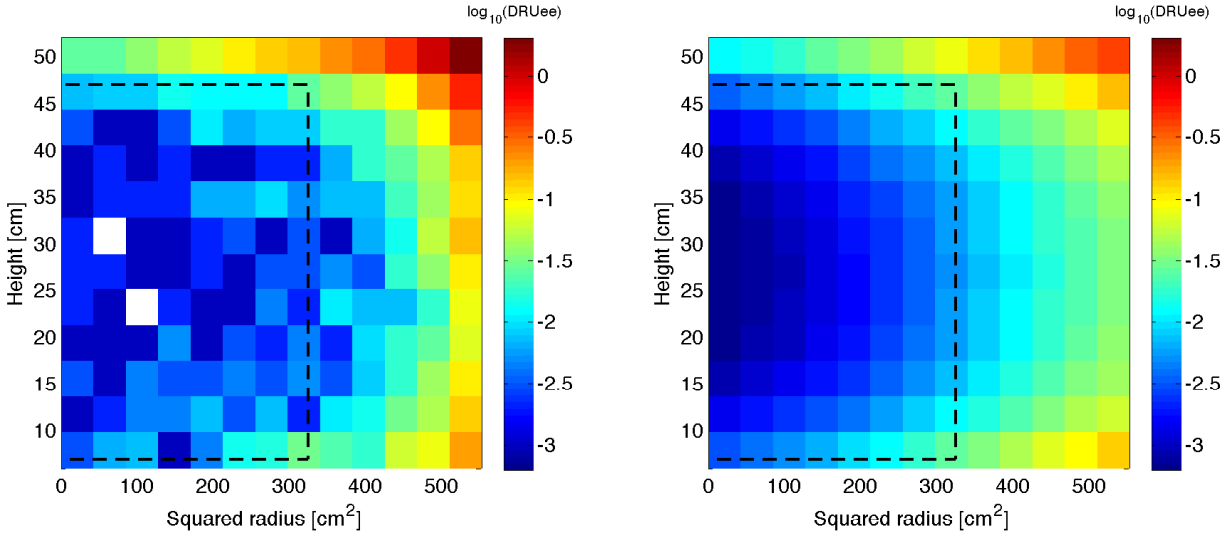

Figure 4.8: Self-shielding: background distributions in detector from measured data (left) and model predictions (right). Fiducial volume outlined in dashed black line. Figure from Reference [67].

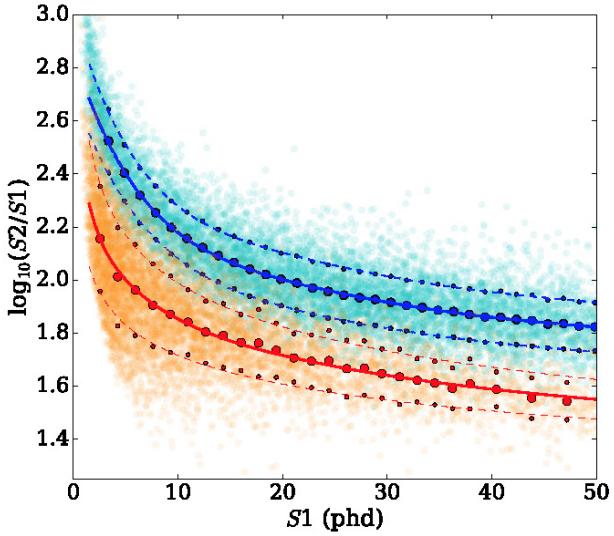

Figure 4.9: Electron and nuclear recoil bands. ER calibration is plotted in cyan, NR in orange. The calculated band mean is plotted with large circles, blue for ER, red for NR. The $\pm 1\sigma$ from the fitted gaussian at band slices is marked by the small circles. Figure from [69]

decays, a spectrum that is well known. A similar ER calibration procedure was also done using a metastable state of krypton $^{83}Kr^{m}$ (Reference [71]), which emits two conversion electrons of energy 32.1 keV and 9.4 keV. The NR band was found using AmBe and Cf-252 neutron sources, and more recently, using a D-D neutron generator (Reference [72]). The calibrations have provided a thorough understanding of what low-energy ER and NR look like in the LUX detector, allowing for informed judgement as to whether an event looks WIMP-like or not. Typically, a 50% NR acceptance is adopted when looking for WIMP-like (NR) events. This cut still contains half of the NR event space while avoiding possible leakage events from the ER band. Because of fluctuations from the mean $S2/S1$ ratio, overlap between ER and NR bands exist. Due to the possibility of ER event signatures fluctuating into the NR region, it is still of course prudent to reduce ER backgrounds as much as possible.

A general look at what calibrations revealed about the LUX detector can be found in Reference [69].

4.5 DAQ

The LUX electronics chain reads out signals from the PMTs with the goal of resolving over 95% of single photoelectrons in any PMT from 5σ baseline noise fluctuations. PMT signals are first sent through preamplifiers for 5x amplification, and then through post-amps which shape and send the signal to three outputs: the Struck digitizer, the trigger, and CAEN discriminators. The digitizer-bound signal from the post-amp (122 PMT channels, now amplified and shaped) is fed into Struck ADC modules that accept 8 channels each. The modules digitize the signals at 100 MHz and a voltage resolution of 0.122 mV/ADC. The 100 MHz sampling rate corresponds to a 10 ns sample width, which should be kept in mind when considering timing properties of signals. In this dissertation, signal times will be described both in terms of samples and μs, and a conversion factor of 10 ns/sample is implied.

Each Struck channel has two memory banks that alternate in storing digitized output. When one memory bank fills completely, data recording switches to the other memory buffer for all channels and all boards, with a deadtime of 17-290 μs associated with each switch.

The trigger system is typically used in an offline fashion, where trigger data gets recorded but does not affect the data acquisition. A variety of trigger conditions can be employed. The postamp output is digitized by the trigger system to identify basic shapes of signals, giving the ability recognize S1 and S2 - like signals. This enables S1, S2, and S1+S2 trigger modes. The water tank is also instrumented with PMTs, and its signal can be used for trigger conditions. Finally, LEDs inside the detector are routinely used to calibrate PMTs and monitor health. They are powered by a pulser outside the detector, and the pulser output can also be used as a trigger input.

The data-acquisition (DAQ) and trigger systems utilize a "Pulse-Only Digitization" (POD) mode where baseline data is suppressed, greatly reducing storage needs. In this mode, a pre-trigger time period and post-trigger time period are defined as well as detection

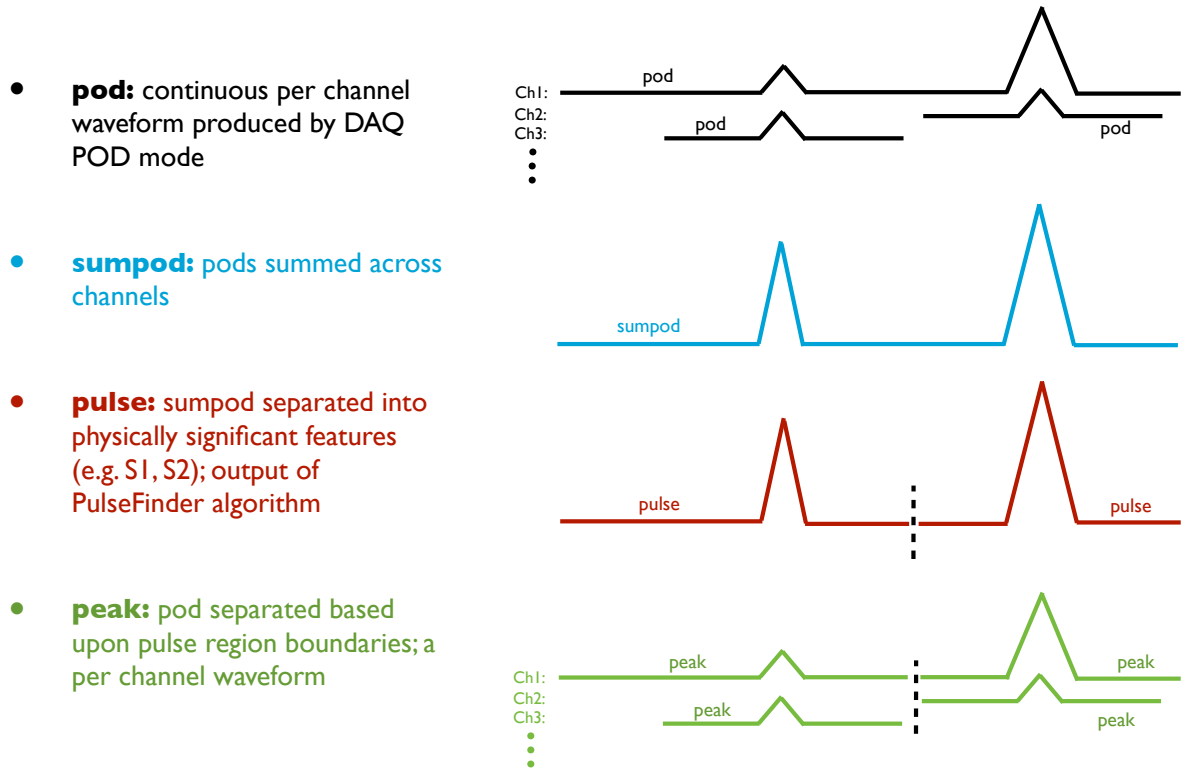

Figure 4.10: LUX waveform terminology. Diagram courtesy of James Verbus

and end thresholds. Data are only recorded to buffer if the signal rises above the detection threshold. The "POD" written to disk consists of the signal from the time it breaks the detection threshold to the time it falls below the end threshold, plus the signal from the pre-trigger time period immediately before and post-trigger after.

More details about the LUX DAQ can be found in Reference [73], and the LUX trigger in Reference [74]. The subject will be revisited in the context of the water tank veto in Chapter 6.

4.6 Data Processing

The raw output from the DAQ is is written to .dat files. Data about trigger conditions and the timing of certain signals are used to create .evt files, where PODs are grouped together into "events" if they occur within 50000 samples of each other and if they are associated with a trigger.

The .evt files are further processed into .rq ("reduced quantity") files, using algorithms that have been developed to extract values of interest for data analysis. One such algorithm is the PulseFinder, which splits a raw waveform into appropriate, separate regions corresponding to separate pulses. Some of the terminology applied to signals in LUX is

illustrated in Figure 4.10. "Pods" are the raw, per-channel waveform collected by the DAQ, and "sumpods" are the "pod" waveforms aligned in time and summed across all 122 PMT channels. Processing leads to separation, which leads to "peaks" as the per-channel output, now separated out by PulseFinder, and "pulses", the sum of "peaks" over all channels. General usage of the term *pulse* does not always match with the LUX meaning of pulse, and care will be taken in this dissertation to be clear when the more formal LUX version of the word is being used.

Other important quantities found through processing include pulse or peak start/end times and pulse or peak *areas*, where the raw electric output is converted to photoelectrons detected by PMTs and integrated for the pulse or peak duration. Top-bottom asymmetry is also used in this dissertation. It considers the sum of the areas for all the peaks coming from the top PMTs (as opposed to all the PMTs as in a pulse), and the sum of all the bottom peaks. Top-bottom asymmetry is defined as

$$\text{TBA} = \frac{(\text{top sum}) - (\text{bottom sum})}{(\text{top sum}) + (\text{bottom sum})}. \tag{4.1}$$

TBA is a measure of which PMT array, if either, sees more light, and can be useful for characterizing pulses. S2s are created in the gas region and are typically very bright, and seen well by both top and bottom PMT arrays. On the other hand, S1s occur within the liquid, where reflections off the gas-liquid interface cause more light to be captured in the bottom PMTs.

Part II

Detecting Cosmic Ray Muons with LUX

Chapter 5

Cosmic Ray Muons

In 1912, Victor Hess set out in a balloon to investigate ionization that had been observed in the air. At the time it was believed that the Earth was the source of the ionizing radiation, and therefore that ionization should decrease with altitude. Hess took measurements up to altitudes of 5 km and found that instead, ionization clearly increased with altitude (Reference [75]). This led him to conclude that some penetrating radiation must enter the atmosphere from above - the radiation was soon after named "cosmic rays". Hess had thus started the the study of cosmic ray physics.

Many questions about the nature and origin of cosmic rays still remain today. Most cosmic rays are thought to be extrasolar in origin, but still from within the galaxy, however extremely high energy cosmic rays of extragalactic origin also exist. There are many processes that can create cosmic rays, including supernovae explosions. The supernova remnants are then accelerated to high energies via interactions with shock waves and magnetic fields. These initial particles have similar make up to the makeup of stars (protons, helium, carbon oxygen) and are considered "primary" cosmic rays, while the interaction of primaries with the interstellar medium create more exotic secondaries. Both primaries and secondaries are incident upon the earth's atmosphere.

Cosmic rays (CRs) follow an inverse power law energy spectrum, with differential flux

$$\frac{dN}{dE} \propto E^{-(\gamma+1)}. \tag{5.1}$$

For energies up to $E \sim 10^6$ GeV, $\gamma \approx 1.7$, while for higher energies the spectrum steepens and $\gamma \sim 2$. About 79% of cosmic ray nucleons are free protons, about 15% are in alpha particles, and the rest are bound in heavier nuclei. A review of cosmic rays can be found in References [15] and [76], Reference [77] is a manual full of useful cosmic ray data, and Reference [78] contains many of the foundational principles of cosmic ray physics.

Figure 5.1: Cosmic Ray's

5.1 Cosmic Ray Muons in Earth's Atmosphere

Cosmic rays are particles that bombard the Earth's atmosphere at a rate of 1000 m^{-2}. As they hit Earth's atmosphere, they can cause electromagnetic and hadronic showers. Protons collide with nuclei in the upper atmosphere to create charged mesons (secondaries), and in particular pions and kaons can be produced.

Cosmic ray muons are primarily generated through pion decay:

$$\begin{aligned} \pi^+ &\to \mu^+ + \nu_\mu \\ \pi^- &\to \mu^- + \nu_\mu \end{aligned} \tag{5.2}$$

Kaons also produce muons ($K \to \mu\,\nu$) but to a lesser extent, with a more significant kaon contribution to cosmic ray muons at higher energies. The extinction of pions and kaons consists of two competing modes: decay into $\mu + \nu$ (Equation 5.2), and interaction with the medium being travelled through.

The flux of cosmic ray muons depends on the production mechanism, energies of their parents, and the depth traveled in the atmosphere. Although the average lifetime of muons is short, 2.2 μs, most CR muons are highly relativistic and survive down to sea level and beyond. Gaisser works through particle cascade equations to describe muon spectrum at the bottom of the atmosphere (at the surface of the earth) as:

$$\begin{aligned} \frac{dN_\mu(E_\mu,\theta)}{dE_\mu d\Omega} &= A\,E_\mu^{-\gamma_\mu}\left(\frac{1}{1+\frac{aE_\mu\cos\theta}{\epsilon_\pi}}+\frac{B}{1+\frac{bE_\mu\cos\theta}{\epsilon_K}}\right) \\ &= 0.14\,E_\mu^{-2.7}\left(\frac{1}{1+\frac{1.1E_\mu\cos\theta}{115\ \mathrm{GeV}}}+\frac{0.054}{1+\frac{1.1E_\mu\cos\theta}{850\ \mathrm{GeV}}}\right)\ \mathrm{cm}^{-2}\ \mathrm{s}^{-1}\ \mathrm{sr}^{-1}\ \mathrm{GeV}^{-1} \end{aligned} \tag{5.3}$$

where the first term in parentheses arises from pion decay contributions, and the second from kaon. At high energies, the zenith angle of the parent cosmic ray starts to be important, as seen by the inclusion of the $\cos\theta$ term. The steepness of the muon spectrum is represented by power index γ_μ.

A muon moving through matter loses energy, and that energy loss is proportional to the amount of matter traversed. This amount is described by the term *interaction length*, which is expressed as a density times path length in units of [g cm^{-2}]. Interaction length can also be expressed as meters of water equivalent (m.w.e.), where 1 m.w.e equals 10^2 g cm^{-2}, given that the density of water is 1 g cm^{-3}. Muons typically lose energy at rate of about 2 MeV per g cm^{-2}. The interaction depth of the atmosphere is 1000 g cm^{-2}, so muons traveling through the atmosphere lose about 2 GeV once they reach the surface of the earth.

At sea level, the average muon energy is $\langle E_\mu \rangle \simeq 4$ GeV, and the flux for $E_\mu > 1$ GeV is $\Phi_\mu = 70$ m^{-2} s^{-1} sr^{-1} , or 1 cm^{-2} min^{-1}(Reference [77]). This flux becomes greatly reduced underground, once muons interact with the denser matter making up the earth's crust. The overall angular distribution goes as $\cos^2\theta$, an angular dependence which flattens at higher energies and larger zenith angles.

5.2 Cosmic Ray Muons Underground

The same processes that govern cosmic ray energy loss in the atmosphere apply to cosmic rays propagating through the earth. However, since the earth is much more dense than the air, unstable particles such as pions and kaons are much more likely to interact than to decay. Stable hadrons and electrons are quickly stopped or absorbed. Indeed, the elimination of these cosmic ray particles is why rare-event searches occur deep underground. However, cosmic ray muons and neutrinos can still survive to great depths. The properties of CR muons that penetrate to deep underground will be explored in this section.

5.2.1 Muon Energy Loss

Cosmic ray muons lose energy through a variety of processes as they travel through matter. The processes can be categorized into discrete and continuous energy loss mechanisms. Ionization occurs continuously and has only a weak dependence on energy. It is the dominant process for muon energy loss through the atmosphere (Section 5.1) where the loss was described with a constant 2 MeV per g cm^{-2}.

For muons continuing past the surface of the earth, radiative processes become important in energy loss. Radiative energy losses depend on the energy of the traveling muon. *Bremsstrahlung* occurs when charged particles interact with the electric fields of nuclei, generating photons. In *pair production*, the muon emits a virtual photon which produces an electron-positron pair. *Photoproduction* is a similar process to pair production in that a virtual photon is involved, but the photon instead interacts hadronically and produces secondary hadrons.

The rate of energy loss can be described as

$$\frac{dE_\mu}{dX} = -\alpha - \beta E_\mu \tag{5.4}$$

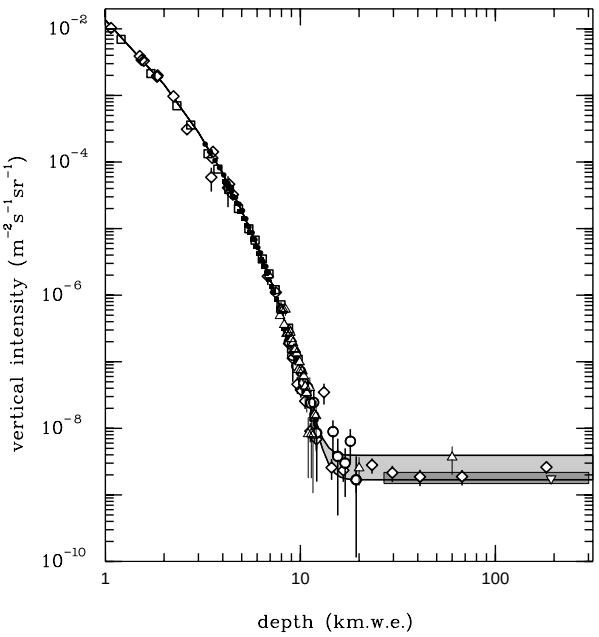

Figure 5.2: Depth-intensity relation for underground muons. Experimental data from References [79], [80], [81], [82], and [83]. The shaded area above $\sim$ 10 km.w.e. represents the contribution from neutrino induced muons. Figure from Reference [15].

where $\alpha = 2$ MeV per g cm^{-2} encapsulates the continuous, ionization losses, and βE_μ represents the discrete, radiative energy losses ($\beta = \beta_{brem} + \beta_{pair} + \beta_{photo}$). One can deduce that at critical energy $\epsilon = \alpha/\beta \simeq 500$ GeV, radiative energy loss equals ionization energy loss. For energies $E_\mu \gg \epsilon$, radiation losses dominate, and for $E_\mu \ll \epsilon$, ionization dominates. With these relations, rough estimates of muon energy spectra and ranges underground are achievable through integration of Equation 5.4. A muon of initial energy $E_{\mu,0}$ that propagates through interaction depth X will have average energy E_μ, related by:

$$E_{\mu,0} = (E_\mu + \epsilon)\, e^{\beta X} - \epsilon. \tag{5.5}$$

The minimum energy required for a muon to penetrate depth X is thus:

$$E_{\mu,min} = \epsilon(e^{\beta X} - 1). \tag{5.6}$$

5.2.2 Depth-Intensity Relation

The *depth intensity relation* is traditionally how muon spectra underground are described, where the integral flux of muons is a function of depth (see Figure 5.2). The shape of the depth-intensity curve can be understood as the surviving muons ($E \geq E_{\mu,min}$ in Equation 5.6) resulting from the energy distribution of muons at the surface. For depths greater than 10 km.w.e., a muon "floor" is created, where the muon flux remains constant regardless of depth due to neutrino-induced muons in the surrounding rock.

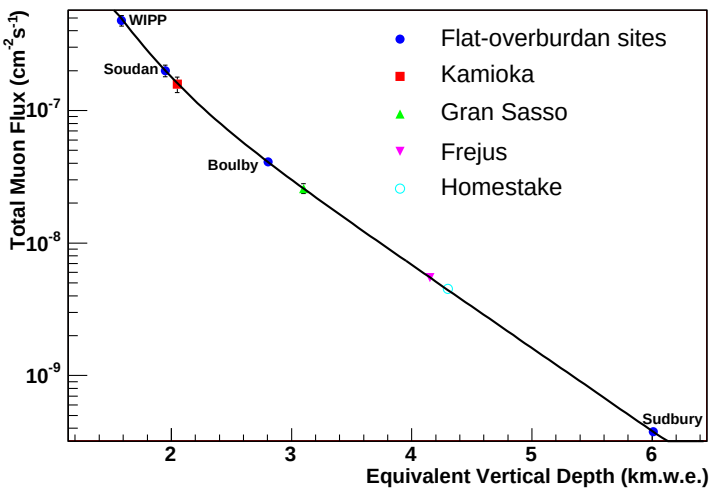

Figure 5.3: Measured muon flux for various underground labs. The fit function Equation 5.9 is shown in solid line. Figure from Reference [85].

The empirical depth-intensity relation was described by Miyake in Reference [84]:

$$I(X, 0^\circ) = (X + a)^\alpha \, (\frac{K}{X + H}) \, e^{-\beta X} \tag{5.7}$$

where a, K, H, α, and β are empirically fitted parameters.

For large depths (below 4000 m.w.e) the third term in Equation 5.7 dominates. Energy loss is proportional to muon energy (the second term in Equation 5.4), and the depth-intensity relation is approximately

$$I(X, 0^\circ) = A \, e^{-X/\Lambda} \tag{5.8}$$

where A and Λ are empirically determined constants, both of which may depend on depth X.

The muon intensity function has more recently parameterized by Mei and Hime in Reference [85]:

$$I_\mu(h_0) = 67.97 \times 10^{-6} e^{\frac{-h_0}{0.285}} + 2.071 \times 10^{-6} e^{\frac{-h_0}{0.698}} \tag{5.9}$$

where h_0 is depth in km.w.e. and I_μ is in units of $\mu\text{cm}^{-2}\text{s}^{-1}$. This fit function is plotted in Figure 5.3 along with the measured values of several underground mines. The equivalent vertical depth is defined as the flat overburden depth that would result in the observed muon intensities. The definition is necessary to compare sites of flat overburden to those surrounded by more complicated mountain profiles. The equivalent vertical depth of the 4850 level of SURF is estimated at 4.3 ± 0.2 km.w.e.

5.2.3 Angular Distribution

Assuming a flat earth topography, a muon penetrating underground will have to travel through slant depth $X_s = X \sec\theta$ at a zenith angle of θ. Combined with the depth-intensity

relation in Equation 5.7, Miyake (Reference [86]) described whole depth range as:

$$I(X,\theta) = \frac{174}{X\,\cos\theta + 400}\,(X + 10\sec\theta)^{-1.53}\,(\frac{X+75}{X+50+25\sec\theta})\,e^{-8\cdot10^{-4}(X+10\sec\theta)} \quad (5.10)$$

At very large depths the distribution can be approximated as

$$I(X,\theta) = I(X,0^\circ)\,\sec\theta\,e^{-X(\frac{\sec\theta-1}{\Lambda})} \quad (5.11)$$

Equation 5.11 was tested in Reference [87] with the Homestake Muon and Neutrino Detector at the 4850 level of Homestake Mine (home of LUX). The observations were in good agreement with the suggested distribution by Miyake, up to a zenith angle of 60° according to the angular acceptance of the detector. A Λ of 700 m.w.e. was found to be accurate to 5%.

5.2.4 Multiple Muons

Cosmic ray muons that survive to deep underground must have been produced by a very energetic primary. It is therefore possible to observe more than one muon in one underground event, all born from the same parent. The study of *multiple muons* can reveal the nature of extremely high-energy cosmic rays, and has been a subject of interest for many decades. Recently, the MACRO experiment observed that about 6% of the muon events in their detector had multiplicity greater than one, and that multiplicities of more than 35 (!) could be achieved in a single event (Reference [88]). In order to observe such multiplicities, a relatively large detector area must be used (12m × 76.5m in the case of MACRO).

5.2.5 Stopping Muons

Stopping muons are muons that have lost nearly all their kinetic energy by the time they reach the underground depth of interest, thereby "stopping" inside the detector. While most muons underground will be of very high energy, the very tail end of the distribution corresponding to low energies will lead to some fraction of muons stopping. Once stopped, the muon can decay into an electron and associated neutrinos with characteristic lifetime 2.2 μs: $\mu^- \rightarrow e^- + \bar{\nu_e} + \nu_\mu$. The muon could also capture onto a nucleus, causing decay and potentially generating a source of neutron backgrounds.

Underground stopping muons can be categorized into two populations. One originates from cosmic ray muons slowed down appropriately by the rock overburden, and the other comes from the decay of local pions which have themselves been created from scattering processes of high energy muons off surrounding rock (see Reference [89]).

Stopping muons are usually described as a ratio R of stopping to *through-going* muons (detailed calculation in Reference [90]). The ratio is estimated to be less than 0.5% at depths below 1 km.w.e. (see Figure 5.4). However, at $\sim$ 4200 m.w.e., known as the Turin point, an anomalous excess of stopping muons has been observed (References [91], [92]). A muon production or extinction process may be uniquely sensitive to this depth, which is very close to the equivalent depth of the 4850 level at SURF.

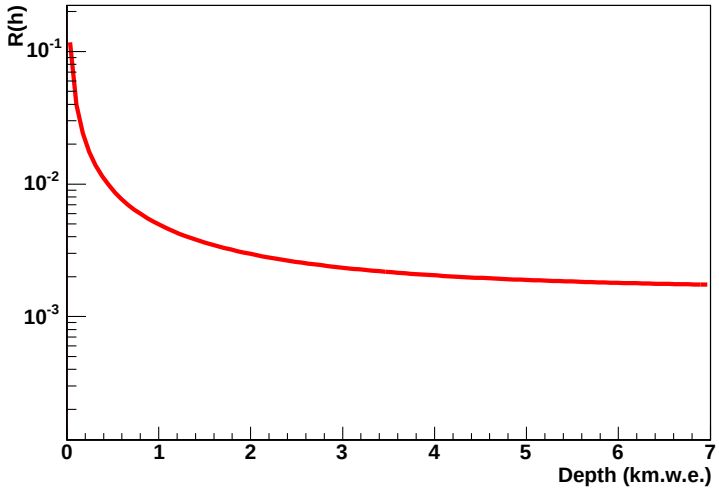

Figure 5.4: Stopping muon ratio. Ratio of stopping to through going muons decreases with greater depth. Figure from Reference [85].

5.2.6 Seasonal Variation

It has been seen that fluctuating atmospheric temperatures lead to variations in muon intensity, both on the surface of the earth and underground (see Global Muon Detector Network [93], MINOS [94]). As temperature increases in the atmosphere, air becomes less dense, leading to a higher number of pion and kaon decays into muons before interacting. The effect is more pronounced for detectors deeper underground. This is because muons that reach great depths come from high-energy pion and kaon parents, which are more likely to interact in the atmosphere and be affected by temperature fluctuations, as opposed to decay.

For temperatures T and temperature coefficient α, the variations in muon intensity I are described as

$$\frac{\Delta I_\mu}{I_\mu^0} = \int_0^\infty dX\, \alpha(X)\, \frac{\Delta T(X)}{T(X)} = \alpha_T\, \frac{\Delta T_{eff}}{T_{eff}} \tag{5.12}$$

MACRO observed this variation from 1991-1994 in Reference [95]. Temperatures and variations in the muon rate were found to be highly correlated, with a correlation coefficient of 0.91 and a calculated temperature coefficient α_T of 0.98. The 1993-1994 data is shown in Figure 5.5.

5.2.7 Muon-induced Neutrons

Muon rates are of great interest to rare-event searches underground because they are a potential source of neutron backgrounds. Studies of underground backgrounds can be found in References [96] and [85].

Muon induced neutrons can be formed in the rock overburden penetrated by the muon,

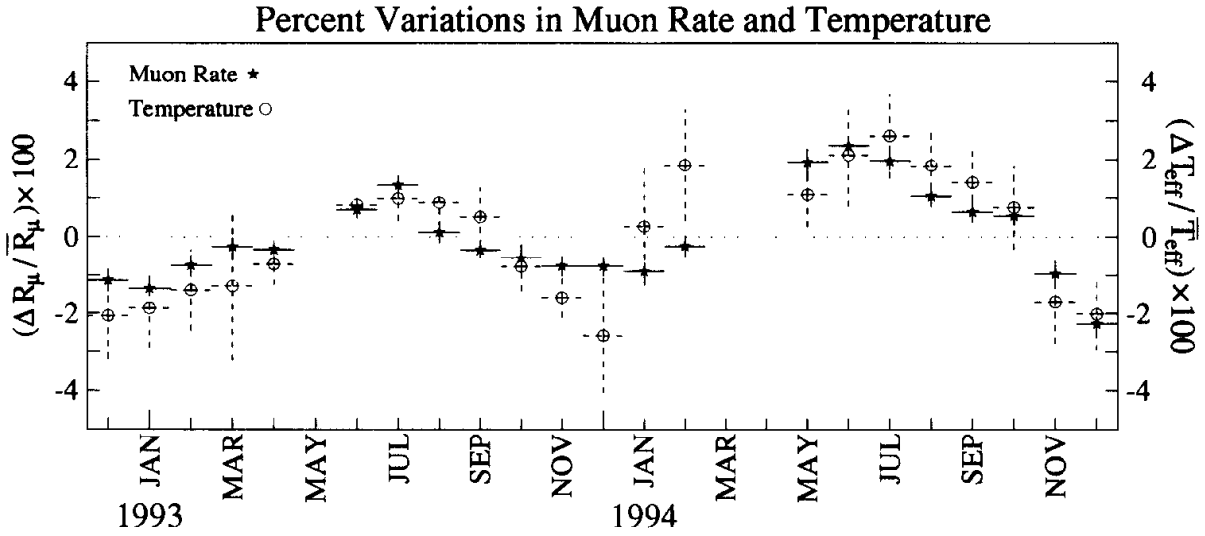

Figure 5.5: MACRO: Muon intensity variation and atmospheric temperature variation superimposed. Figure from Reference [95].

or in any detector or shielding materials the muon may pass through. Cosmic ray muons can produce neutrons through several different processes:

- *Muon capture* onto nuclei (as mentioned in Section 5.2.5).
- *Electromagnetic showers* originating from muons. Photons and electrons from bremsstrahlung and pair production can cause particle showers. Cross sections grow with Z^2 and muon energy.
- *Interaction with nuclei* via virtual photon exchange, also referred to as muon *spallation* or photoneutron production..
- *Quasielastic scattering* between muon and nucleon, where a neutron is knocked out of the nucleus by an incident muon.
- *Secondary production* resulting from the above processes.

According to theory, the neutron production rate should grow with muon energy as $\sim E_\mu^{0.75}$. Simulations done by Wang et al in Reference [97] agree with this, finding the neutron yield per muon to be:

$$N_n = 4.14\, E_\mu^{0.74} \times 10^{-6} \text{ neutrons/(muon g cm}^{-2}) \tag{5.13}$$

5.2.8 Simulation

Although some of the expressions presented in the subsections above (Equations 5.4, 5.8) lend themselves to analytic solutions, they will not adequately characterize the muon flux at

large depths. More powerful predictions are made with detailed simulations. Many packages exist to simulate particle propagation through matter, some are multipurpose (GEANT4 [98], FLUKA [99]). MUSIC (References[100], [101]) is a simulation package that has specifically been developed to describe 3D muon transport. Utilizing these simulations allows for the consideration of different overburden profiles beyond a flat-earth simplification, and of differing detector and shielding geometries.

Chapter 6

The LUX Water Tank

The LUX detector and cryostat are placed within a cylindrical water tank with height 6.1m and diameter 7.6m (see Figure 6.1). The tank is filled with 270 metric tonnes of water, which is continuously circulated and purified to reduce backgrounds and impurities that may creep into the water from the surrounding air and tank walls. A N_2 gas purge fills the air gap between the water surface and the top of the tank to further keep the area free of impurities. The water shields the detector, and the tank also houses 20 PMTs that serve as an active muon veto, detecting the Cherenkov light that is emitted by high energy muons traveling through the water.

6.1 Passive Shielding

On the 4850 level at SURF, the LUX detector is shielded from most cosmic rays that bombard the surface of the earth. The 4,850 feet of rock overhead is also expressed as ~ 4200 meters of water equivalent (m.w.e.), a common way of describing overburden interaction depth in a way that is comparable between different shielding materials. Deep underground, despite escaping cosmic rays, external backgrounds can still plague a detector. The rock of the surrounding mountain itself is radioactive, emitting γs and neutrons. Also, high energy cosmic ray muons can still penetrate down to this depth. While the muons themselves will be easy to identify and discount in the detector, they can also produce neutrons when passing through the mountain rock and passing through the water of the shield. Since neutrons produce nuclear recoils just as WIMPs are expected to, neutron backgrounds must be reduced as much as possible to enable a clear WIMP signal.

The water acts as an effective shield against the remaining external backgrounds that come from the cavern walls. A 20 tonne inverted steel pyramid lies immediately underneath the water tank, providing extra shielding from below. This extra protection on the bottom lets the LUX detector sit lower inside the water tank to enhance the protection by water from above. The cryostat is positioned in the tank so that the LUX detector is shielded by a minimum water thickness of 3.5 m radially, 2.75 m overhead, and 1.2 m from underneath.

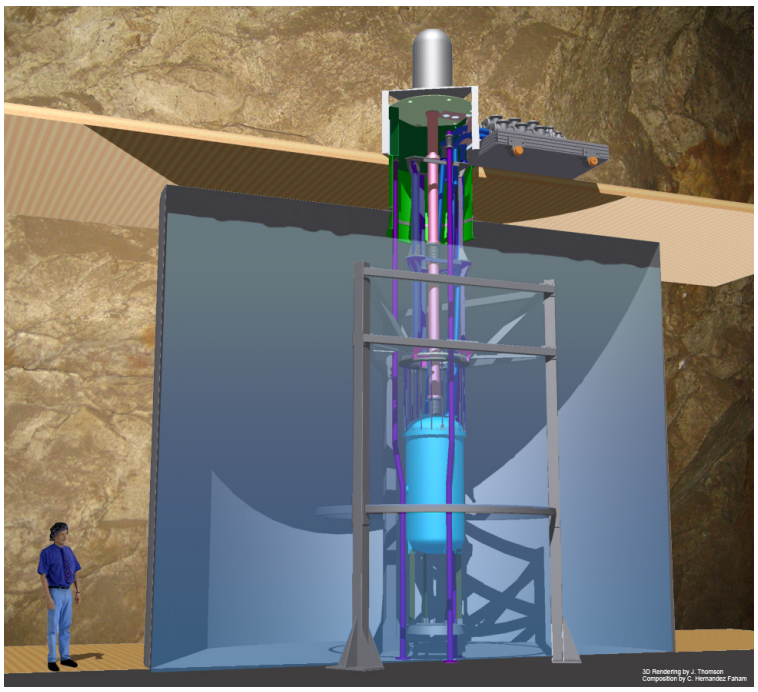

Figure 6.1: LUX inside water tank at Davis Campus.

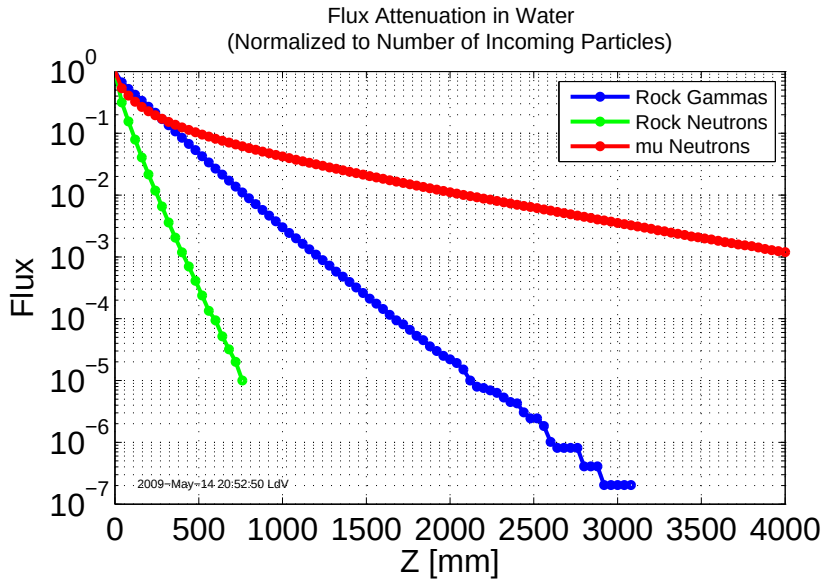

Figure 6.2: Attenuation of external backgrounds in water. 2.75 m of shielding (the minimum height of the water layer above LUX) virtually eliminates rock neutrons and reduces rock gammas by a factor of over 10^6. Muon induced neutrons experience a flux reduction of over a factor of 100. From Reference [102].

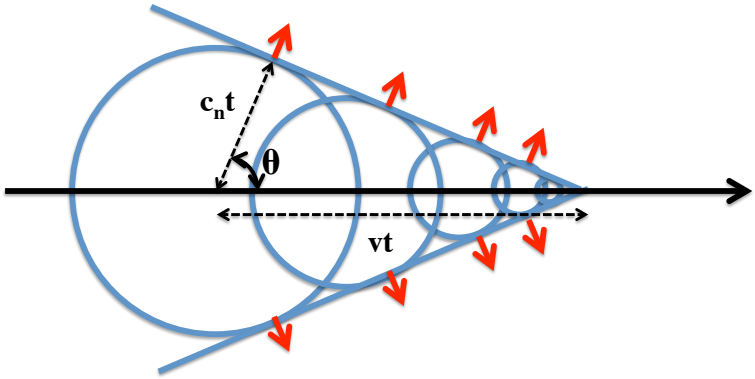

Figure 6.3: Cherenkov radiation: light cone from relativistic particle traveling from left to right. Small, red arrows indicate the emission of Cherenkov light, which is at an angle θ to the motion of the particle.

The dimensions of the water tank were chosen and optimized based on GEANT4 simulations of attenuation of neutron and γ backgrounds by water (see Reference [102]). In Figure 6.2, standard models of neutron and γ distributions in the Davis cavern were used and set to be incident upon a semi-infinite wall of water. The attenuation is calculated as the number of particles that travel beyond a depth of water Z, divided by the initial number of incident particles. Pronounced reductions in flux for rock γs and neutrons are seen, with a more modest reduction for the higher-energy muon induced neutrons. Further simulations were performed using several shielding geometries mimicking LUX in the water tank. The tank dimensions were determined based on the activity levels reaching the detector, and by requiring that sensitivity goals for the detector be met and that external backgrounds are subdominant to the internal backgrounds originating from the PMTs. The current tank dimensions lead to an expected $\sim 1 \times 10^{-3}$ external γs and $\sim 1 \times 10^{-1}$ external neutrons reaching the detector fiducial volume for a 30,000 kg-day exposure.

6.2 Cherenkov Radiation

In addition to providing shielding, water can reveal the passage of high-energy particles by their production of Cherenkov radiation. The Cherenkov effect was first observed by Cherenkov and Vavilov (Reference [103]), and later interpreted by Frank and Tamm (Reference [104]). The phenomenon occurs when a charged particle travels through a transparent, dielectric medium at a velocity $v = \beta c$ greater than the speed of light within that material c_n. The phase velocity of light within a material is related to the material's refractive index n and the speed of light in vacuum c by $c_n = c/n$. The charged particle disturbs the electric field in the medium, and it travels quickly enough that it leaves an electromagnetic shock wave in its wake, similar to a sonic boom from a supersonic jet. Successive wavefronts interfere constructively to produce a light shock front, emitting Cherenkov radiation at an angle θ to the direction of the charged particle's motion – a cone of light with opening half-angle

Particle	E_{thresh} [MeV]
μ	54
electron	0.26
proton	475
deuteron	960
α	2000

Table 6.1: Minimum energy required to produce Cherenkov radiation in water (n=1.33).

θ. According to the geometry of the process (see Figure 6.3), the angle θ is given by

$$\cos\theta = \frac{1}{n\beta}, \tag{6.1}$$

giving the limit for highly relativistic particles ($\beta \to 1$):

$$\theta_{max} = \cos^{-1}\frac{1}{n}. \tag{6.2}$$

In the case of water ($n = 1.33$), highly relativistic particles emit a Cherenkov cone of angle $\theta_{max} = 41°$, and the minimum speed required to produce Cherenkov radiation is $\beta_{min} = 0.75$. Relativistic muons traveling through water would then require a minimum energy of 54 MeV to be detectable by a Cherenkov detector. The threshold energies of other charged particles are displayed in Table 6.1

The number of photons emitted in this process is usually expressed as a number per unit length, per unit photon energy. The early work of Frank and Tamm describes this as

$$\frac{d^2N}{dEdx} = \frac{\alpha Z^2}{\hbar c} \approx 370\, Z^2\, \sin^2\theta\ \mathrm{eV}^{-1}\ \mathrm{cm}^{-1} \tag{6.3}$$

where Z is the charge of the primary particle. Muons traveling through water are expected to produce ~ 200 photons per cm traveled (Reference [105]).

Cosmic ray muons reaching the 4850 level of Homestake are highly relativistic, with an average expected energy of 321 GeV. By instrumenting the water tank with PMTs, Cherenkov light can be collected, tagging the passage of nearby muons and alerting observers to the possible presence of muon-induced neutrons.

A review of Cherenkov counting can be found in [106], and was referenced here.

6.3 LUX VETO PMTs

The LUX water tank is outfitted with 20 10-inch Hamamatsu R7081 PMTs, which will be referred to as the water or veto PMTs when necessary (as opposed to the xenon space PMTs). Since this chapter is primarily concerned with water tank components, any references to

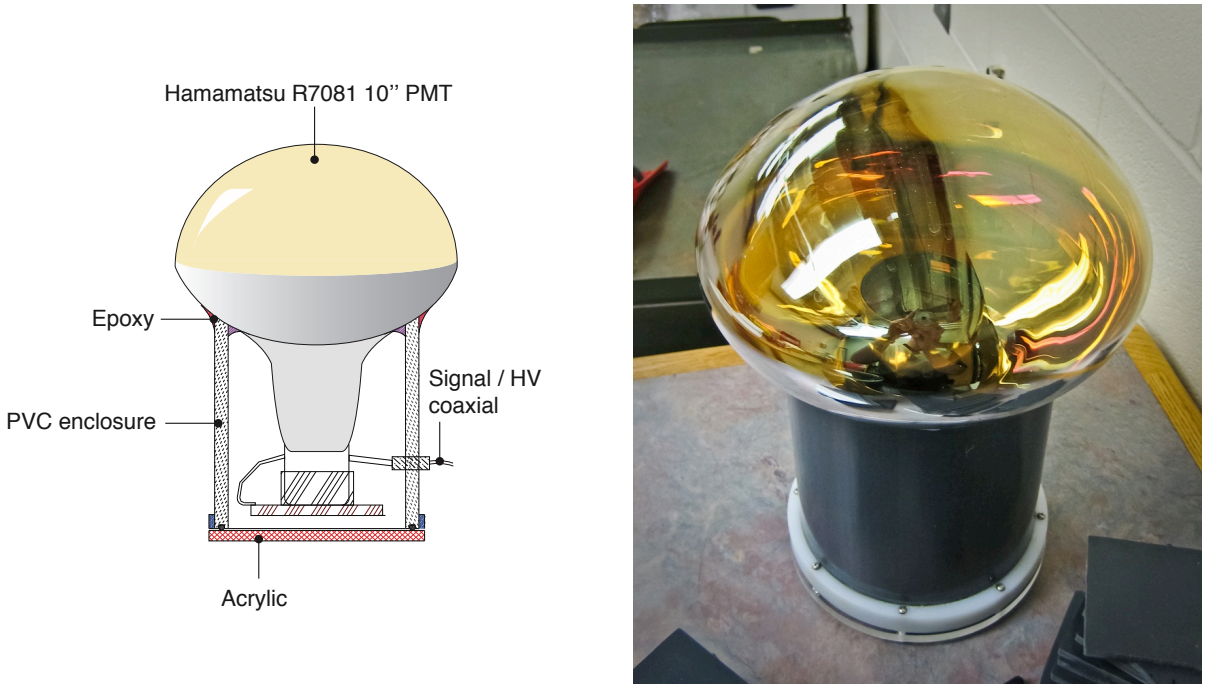

Figure 6.4: LUX VETO PMT.

PMTs should be assumed as veto PMTs, and references to xenon space PMTs will be explicitly stated. The PMT coverage of the water tank is relatively sparse compared to some other Cherenkov detectors. For example, Super-Kamiokande utilizes over 13,000 PMTs to cover their cylindrical detector of height 40 m and diameter 40 m. However, the walls of the LUX water tank are also lined with Tyvek sheets, which are highly reflective to Cherenkov light, and increase the detection efficiency of the PMTs when considering multiple photon bounces off of the Tyvek walls. As a muon veto, the PMT coverage suffices, and is actually comparable to the Super-K veto which boasts 99.99% efficiency. The veto PMTs are 10 inches in diameter, and their lower halves are housed in a PVC pipe enclosure, which is epoxied to the PMT body to form a water tight seal. A single RG58 cable both provides power and reads out the signal for each PMT. See Figure 6.4.

The 20 PMTs are arranged in four vertical columns of five PMTs, with the four columns corresponding to the cardinal directions North, East, South, West. In each column, four PMTs are along on the water tank wall, looking radially inward. The fifth PMT lies on the water tank floor, two feet away from the wall, looking upwards. Four pairs of steel cables run up the length of the water tank, and the wall PMTs are clamped to the cables via attached "wings." The floor PMTs are weighted down to keep them anchored to the ground when underwater. A view of this arrangement can be seen in Figure 6.5

Each veto PMT can be identified by its cardinal direction and vertical position. Row 1 describes the topmost PMTs, with position number increasing downward until reaching the floor PMTs at row 5. The PMT identifier consists of cardinal direction plus row number,

Figure 6.5: Inside the LUX water tank.

for example N1 is the top-most PMT in the string on the north side of the tank, W3 is the third PMT down in the west string, and S5 is the upward-facing floor PMT on the south side.

The signals of the 20 veto PMTs are read into one Struck board with 8 channels on the DAQ, requiring some combining of signals. Each wall ring (N1, E1, S1, W1 for example) is summed and fed into one Struck channel (rings 1-4 correspond to channels 129-132 respectively), while each individual floor PMT enjoys its own channel (channels 133-136). When looking at data from the water PMTs, it's important to remember that four of the per-channel waveforms are the summed responses of the PMTs grouped within the same wall ring height.

The water tank contains four blue LEDs that can be powered using a front-end pulse generator. The LEDs are used to calibrate the single photoelectron (sphe) responses of the PMTs. This pulse generator also services LEDs in the xenon space, and is used to calibrate and monitor the health of the xenon space PMTs. Timing between xenon space and veto signals can thus be tested by sending simultaneous pulses to LEDs using the same input from the pulse generator.

There are three nominal bias voltages for each veto PMT: low, medium and high. The low gain setting corresponds to a single photoelectron (sphe) height of $\sim$15 mV, and the high gain to sphe height of 30-40 mV. The sphe spectra for all three gain settings are displayed for 8 veto PMTs in Figure 6.6. A POD threshold of 8 mV was enforced to reduce pickup

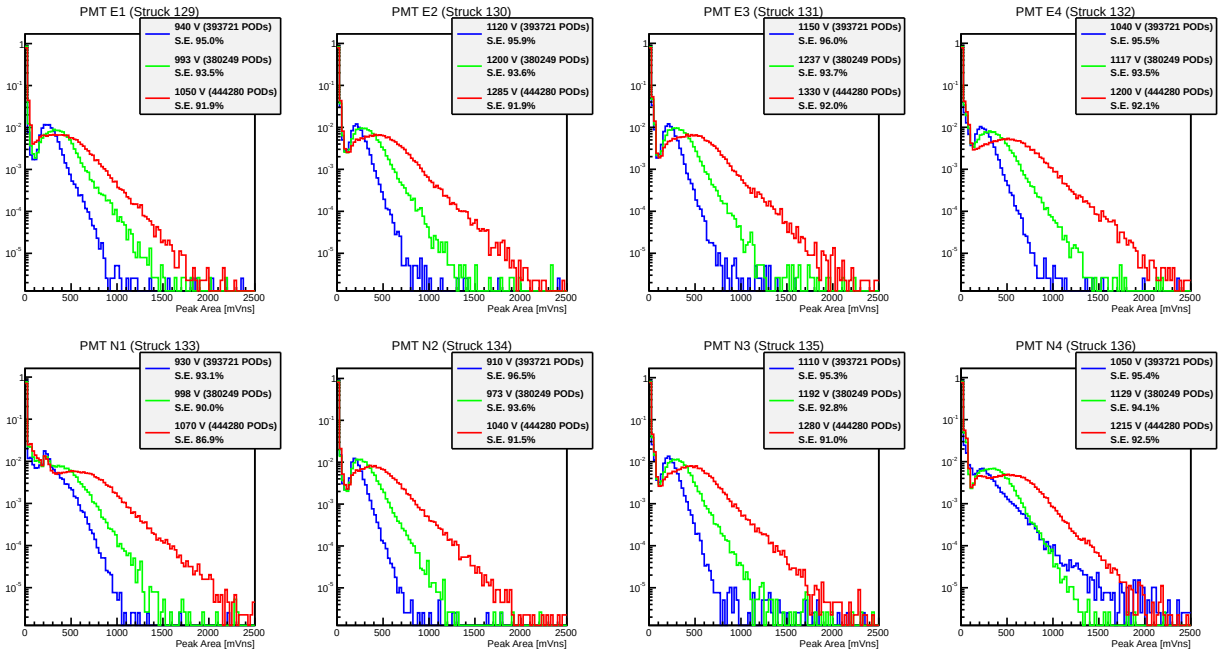

Figure 6.6: LED single photoelectron spectra as a function of gainfor water tank PMTs. 3 gain levels used, north and east PMTs 1-4 displayed.

noise contributions in the veto signals, and a pulse amplitude of 1.5 V powered the LEDs.

6.4 LUX VETO Trigger

This section will expand on the LUX trigger, introduced in Section 4.5. The trigger scheme for LUX encompasses multiple components, allowing for varied sources and uses of a trigger. A trigger event results in a pulse in the Struck trigger channel (ch. 128) and a pulse in the Struck trigger type encoder (TTE) channel (ch. 126). Ordinarily, trigger information is not used by the data acquisition system until the Event Builder program processes .dat files. As mentioned in Section 4.5, .evt files containing events are produced at this stage, and only the data surrounding trigger pulses is stored, and the trigger is utilized in an offline fashion. The exception to this is when data is being acquired in Valid Pulse Trigger Gate (VPTG) mode. In this configuration, PODs are only written to .dat files if they occur within a certain time window of a trigger pulse. Thus, as with traditional hardware triggers, data is only collected when a trigger is detected.

The veto system runs permanently in VPTG mode to suppress noise and low-energy backgrounds that would otherwise flood the DAQ. A further subtlety to veto system triggering is the usage of a trigger hold-off, the subject of Section 6.4.2.

6.4.1 Trigger Sources

A trigger pulse in channel 128 can be produced by 3 distinct sources: the LUX DDC8 trigger, the LED sync trigger, and the veto system MAjority Logic Unit (MALU) trigger. Trigger channel 128 treats each of these sources equally, and a pulse of the same shape is produced in each case. However the accompanying pulse in Ch. 126 (the trigger type encoder) discriminates between different trigger sources with pulses of different amplitudes.

- DDC8: this trigger uses groups of Xe PMT channels and user-defined logic to generate triggers. It does not use veto system information, nor does it affect veto system data collection. A trigger generated by the DDC8 does not trigger the veto system VPTG.
- LED: this trigger occurs whenever the pulse generator powering the calibration LEDs is in "sync on" mode. This trigger DOES feed into the veto system VPTG: any water tank PODs digitized in proximity of an LED pulse will be written to .dat files.
- MALU: this trigger unit is a MAjority Logic counter of water PMTs. A copy of all 20 water PMT amplifier outputs is passed to 20 discriminators with a pre-defined threshold. The output of all 20 discriminators is fed to the MALU, which produces a NIM logic pulse when $> N$ channels break threshold in a 400 ns time window. The value of N can be adjusted, and $N = 4$ and $N = 5$ requirements were both used throughout the run. The veto system VPTG accepts this trigger as well as the LED trigger.

6.4.2 Trigger Hold-off

The trigger hold-off prevents the event builder from building multiple events that contain the same POD data. This is implemented on the hardware level by suppressing triggers arriving before a user-specified time after a registered trigger.

For example, without a trigger hold-off: signal A produces a MALU trigger at $t = 0$ ms, causing a pulse in Struck channel 128. Any water PODs within .5 ms of $t = 0$ ms are included in this event by the event builder. If a second signal "B" occurs at $t = 0.1$ ms, another pulse is sent to channel 128, and thus another event will be built. However, signal A (being < 0.5 ms before signal B) would be included in Event B by the event builder. Thus, the PODs within signals A and B will appear in 2 distinct events and .evt files.

The suppression of the channel 128 pulse corresponding to signal B is possible while still allowing for the operation of the VPTG. The trigger hold-off only affects the Struck channel 128 activity, and does not suppress water tank data from being written to disk. In the above scenario: signal A produces a trigger pulse in channel 128, and activates the VPTG, allowing water data to be written to disk. Signal B does not produce a channel 128 pulse, but still turns on the VPTG, so water PODs would still be written to disk. Now the event builder only builds one event, containing the PODs from both signals A and B.

The VPTG is the default running mode for the veto system: no PODs are written to disk unless they fall in the VPTG window, as created by a trigger from the MALU. This gate is generated regardless of the trigger hold-off.

6.5 Coincident Timing Between Xe and Water Signals

In order to better characterize events with both xenon detector and veto signals, coincidence timing was studied utilizing the LEDs in both spaces. A pulse generator output was fanned out to power both xenon LEDs and water tank LEDs, sending signals into both spaces simultaneously. A 1.58 V signal was sent to the spaces at a rate of 1 Hz, and triggers were generated "naturally" on the water and xenon tank signals, meaning no sync from the LED signal generator was used. Coincident veto-xenon pulses were observed with a consistent 147 sample offset that arises from differing delay buffer settings between veto and xenon PMTs when writing data to the DAQ (see Figure 6.7). Events triggered on the generated veto PMT pulses with an efficiency of $> 99\%$. It was demonstrated that coincident events in xenon detector and water veto will appear in the DAQ data stream with a 147 sample difference, with the veto data appearing first and xenon detector signal afterwards.

6.6 Signals in the LUX VETO

While the LUX detector is searching for WIMPs, the veto PMTs will detect Cherenkov light created by passing high-energy muons. Figure 6.8 displays a signal generated by a through-going muon. Most of the light appears within the first 10 samples, but the signal is prolonged due to multiple photon bounces off of the Tyvek water tank walls. Since most cosmic ray muons and their associated Cherenkov cones will be downward-going, more light appears in the lower PMTs than the upper PMTs.

The water tank is also sensitive to beta decays. As shown in Table 6.1, a 0.26 MeV (or greater energy) electron will generate Cherenkov light. In particular, if Radon plating onto tank surfaces has occurred or radon gas accumulates in the air gap at the top of the tank, the long lived radon daughter Pb^{210} can emit relativistic betas that will also appear in veto data.

A small fraction of cosmic ray muons are expected to lose all of their energy while inside the water tank (recall stopping muons in Section 5.2.5). Muon decays within the water tank will be observable as double pulses: first from the muon which stops, and then a second signal from resultant electron, piling up at a characteristic time 2.2 μs afterward.

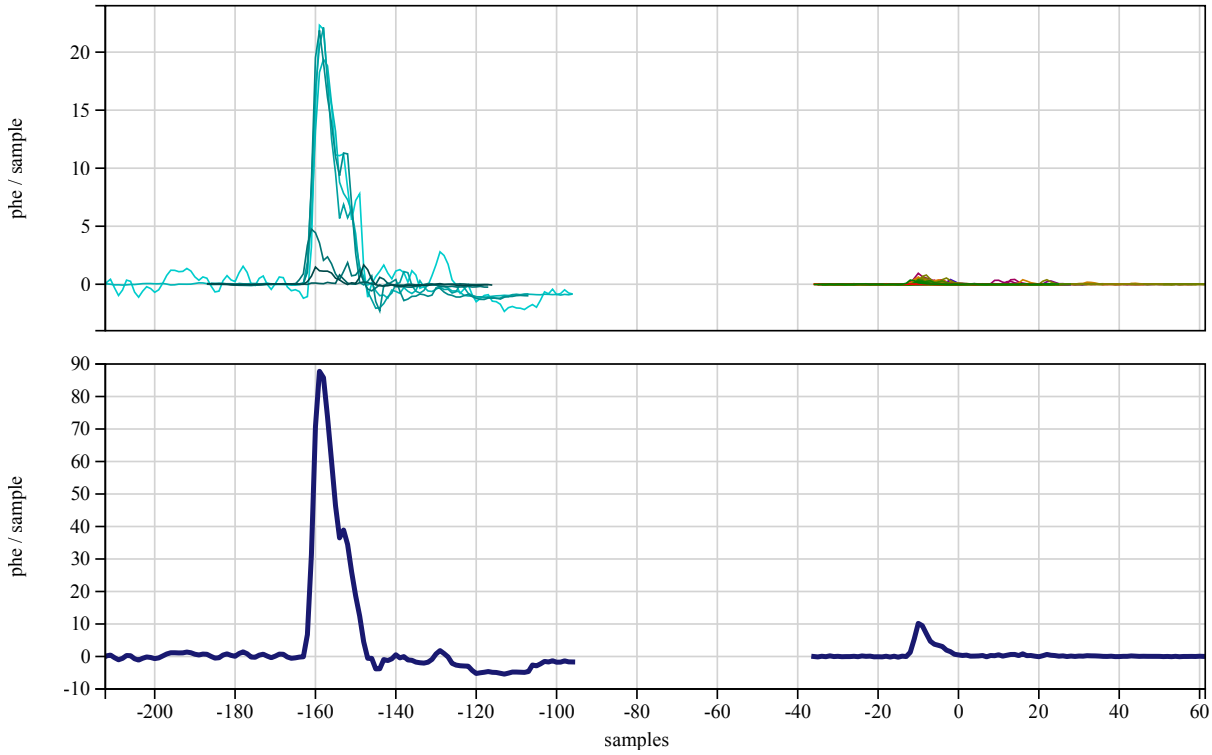

Figure 6.7: Waveforms for coincident Xe-veto signals: LED pulsing. The signals in water and xenon spaces were generated by LEDs within both spaces that were powered by the same signal generator. The signal from the veto PMTs appears first, at -160 samples. The xenon PMT signal appears at -10 samples, 150 samples afterward. Differing delay buffer settings in the DAQ causes this 150 sample offset between xenon and veto signals. Individual PODs are displayed on top, sumPODs on the bottom.

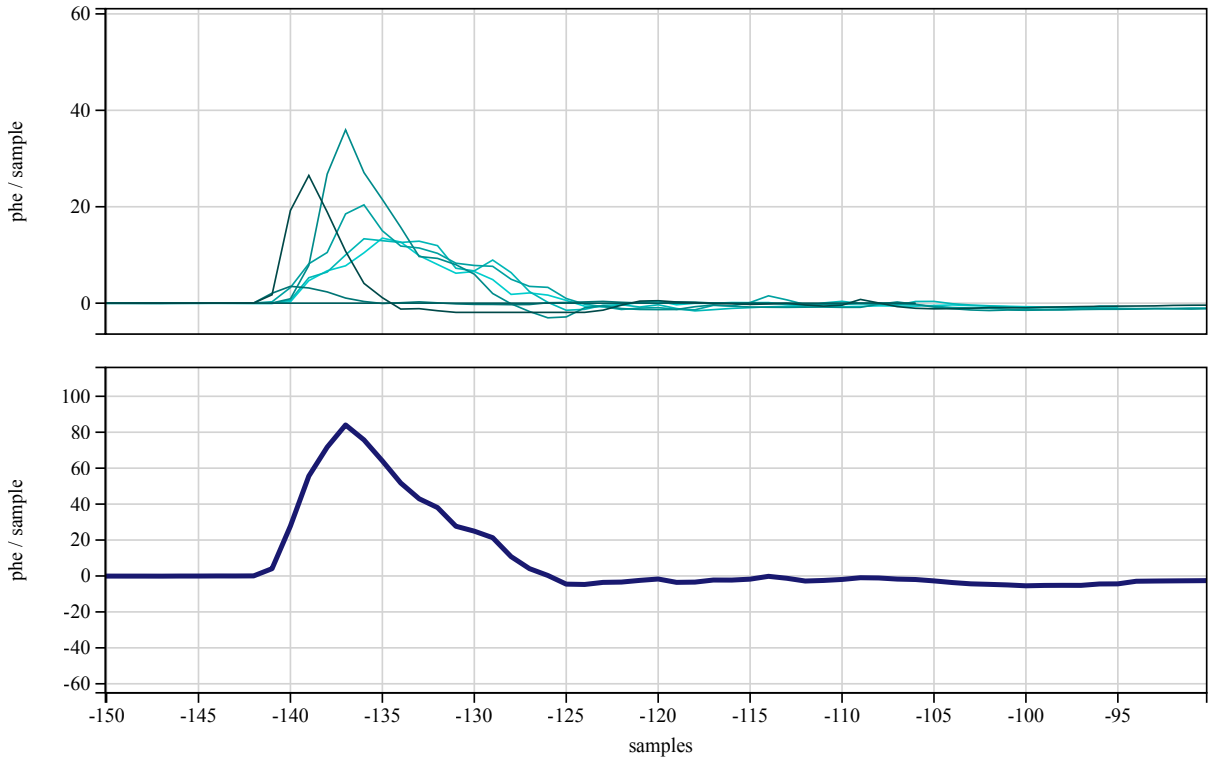

Figure 6.8: Veto signal. Cherenkov Light was generated by a throughgoing muon, captured by veto PMTs. Top: individual POD waveforms from 8 veto DAQ channels; 4 channels of summed PMT "rings," 4 channels from individual floor PMTs; not all channels written due to not breaking above POD threshold. Bottom: veto SUMPOD.

Chapter 7

Cosmic Ray Muon Signals in LUX

A method for identifying muons in LUX is described in this chapter. Coincident signals between the water tank and xenon detector are identified, and a series of cuts employed to reveal events that are cosmic ray muons whose paths traverse both the water tank and the xenon volume. The LUX detector's extraction region provides a unique pulse signature in response to passing high energy muons, so the xenon gas/liquid interface provides the fiducial surface through which muon flux is determined.

7.1 Data Selection

Data for this analysis was taken from the 300 live-day science run of LUX, dubbed Run04, which occurred from December 2014 to May 2016 at the Davis Cavern of SURF. Data was collected in datasets lasting up to 8 hours, with interruptions for calibrations and the resolving of technical issues. Consistency was ensured by only using data taken in "WIMP search mode." Trigger conditions were thus identical throughout all the datasets. Detector purity and stability goals were met. The absence of calibration sources reduced the occurrence of random coincidences between the veto and xenon detectors.

During Run04, the 20 LUX veto PMTs were in several different on/off configurations. At some points during Run04, extremely high POD rates caused by a single veto PMT were detected. The high rates were sometimes simply caused by faulty cable connections, solved by re-seating cables securely, but sometimes the problem was identified as a sparking PMT, at which point the PMT was turned off for the remainder of the run. High-POD rate datasets determined to be caused by faulty instrumentation were thrown out.

The W5 PMT detached from its anchor point before the start of Run04 and was turned off for the entire run since its position and orientation were uncertain. The W1 PMT was also off for the duration of Run04 due to sparking concerns. In June 2015 the bottom E5 PMT could not bias, and remained off for the rest of the run. During the diagnostic tests for E5, PMT S5 was unplugged and forgotten, and plugged back in when this was discovered 2 months later.

This analysis only used water tank data obtained from the four top rings of PMTs, 15 in

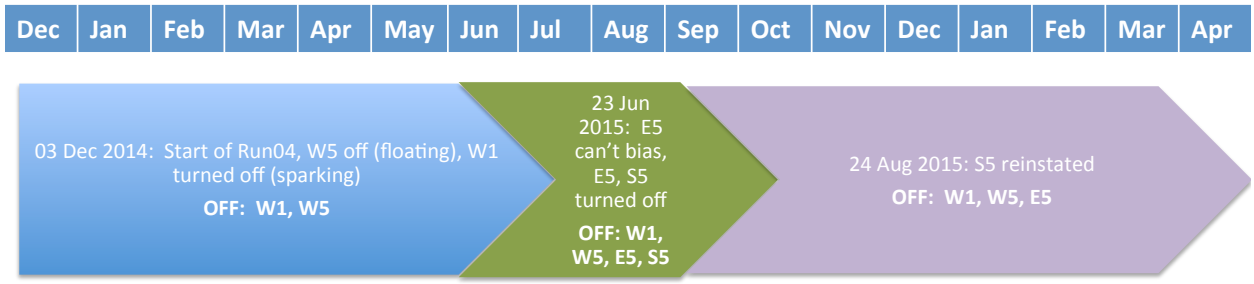

Figure 7.1: Timeline of PMT states in Run04

all (N1, E1, S1, N2, E2, S2, W2, N3, E3, S3, W3, N4, E4, S4, W4) divided across 4 channels in the DAQ. By eliminating the irregular X5 (bottom) PMT configuration from consideration, the water tank data was thus consistent throughout the entire run when looking at summed total pulse areas and heights.

Imperfections in the data processing stream resulted in corrupt data files and in some cases, loss of evt data. Since this analysis used both processed RQ data and raw evt waveforms, any cases of corruption in the data processing were thrown out by eliminating the entire corrupt dataset from consideration.

7.2 Muons in the Xenon Volume

Most recoil interactions in the LUX detector occur at a simple point in the detector, resulting in the typical S1-S2 signature described in section 4.1. However, a throughgoing muon in the active xenon volume exhibits a unique pulse shape. A high energy cosmic ray muon interacts and excites throughout its entire path through the detector, creating a line source of ionization. The S1 height will be large, since excitations are occurring along the muon's entire path, instead of in some localized region. The S1 light emitted will be proportional to the track length of the muon in xenon. Because the gains of the PMTs aren't specifically tuned for such high energy interactions, the actual signal will saturate or at least exhibit a nonlinear PMT response for any muon tracks of non-negligible length. While energy information can't be easily extracted for muon events, S1s can still be easily identified based on their timing quantities and top-bottom asymmetry, and used as a reliable high-energy muon counter.

If the muon path intersects the gas-liquid interface, part of the track will include the high-field extraction region (between the liquid surface and gate grid), resulting in a large, immediate S2 following the event's S1. At high fields, electron mobility in liquid xenon reaches a terminal velocity of $2.6 \times 10^5 \pm 10\%$ cm/s [107]. The 0.5 cm high liquid level in the extraction region corresponds to a drift time of 1.9 μs from gate to liquid level, a minimal bound on the timing width of the immediate S2. The S2 will actually last longer due to the decay constants of the electron states (24 ns for electrons in triplet state) and diffusion of the ionization electrons in the direction (vertical) of drift. The portion of the track in the

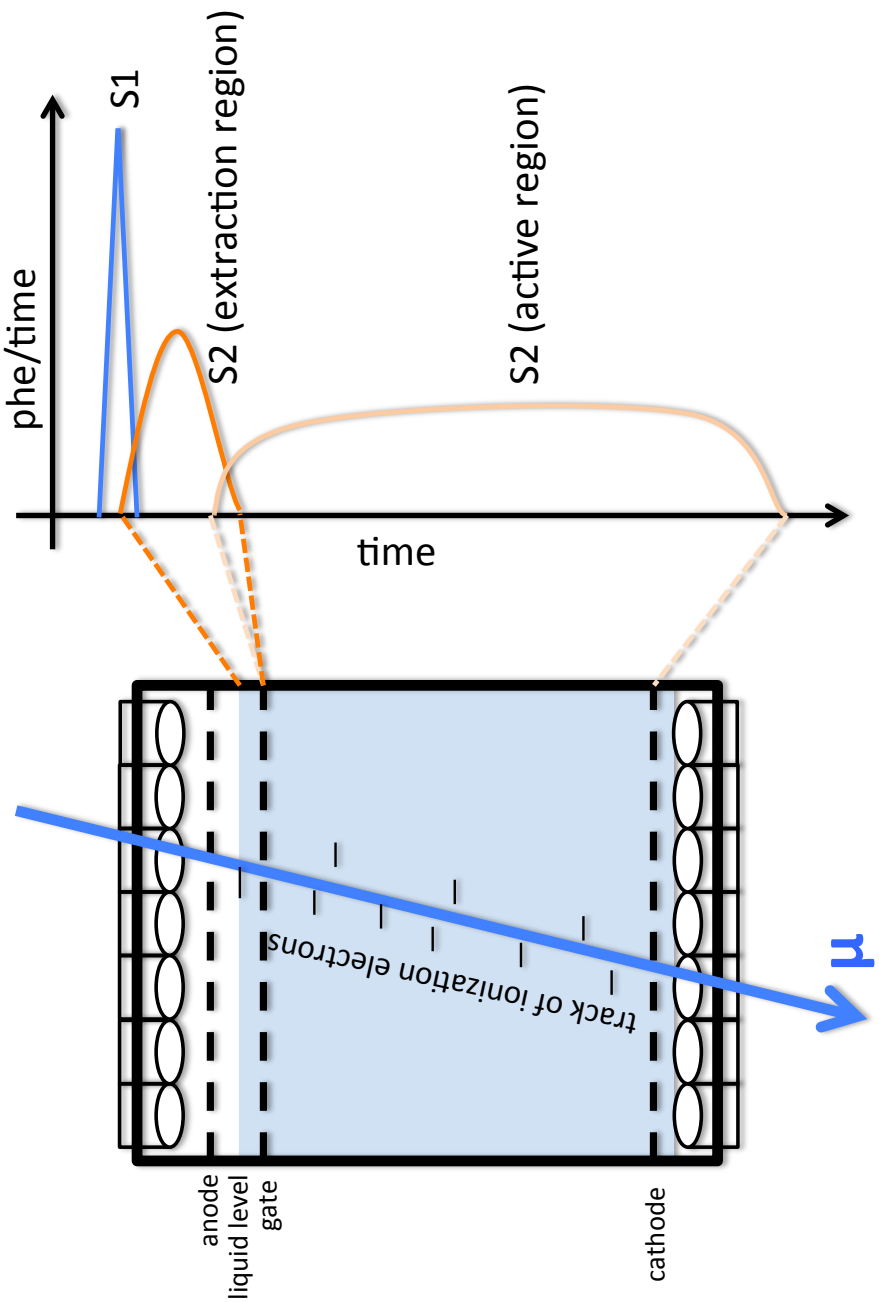

Figure 7.2: Signal from throughgoing muon in LUX Xenon volume. A large S1 pulse is generated from every point of interaction along the muon track through the xenon. A large S2 follows immediately, caused by the ionization in the extraction region. A lower yield, long S2 follows from the ionization in the active region.

active region (between gate and cathode grids) will then have its ionization electrons drifted to the extraction region, creating a prolonged S2 signal that provides the projection of the track along the z-axis (See Figure 7.2). Real event waveforms are illustrated and described in Section 7.5.

A muon path through the liquid leaves a line of ionized electrons, creating a continuous stream of drifted electrons that create S2 light for an extended period of time. However, the corresponding signal recorded in LUX exhibits an obvious decay in the S2 signal from the active and extraction regions, instead of a continuous, constant-height S2 that might be expected from a steady stream of electrons entering the extraction region. Two factors contribute to this decay. The first occurs within the xenon, due the finite electron lifetime of the detector. Ionization electrons are lost as they recombine with other charge-seeking components within the detector. Electrons caused by events occurring at the bottom of the detector have further to drift, and are more likely to be lost to recombination due to this increased drift time. Thus S2 signal size will be reduced depending on the depth of its origin and the electronegative purity of the detector. This effect is also accounted for in analyzing regular S2s from single-scatter events, and are used to make corrections to an event's calculated energy, based on drift time with respect to the corresponding S1 and the measured purity of the detector, which is obtained from regular calibrations and samples.

The second, more prominent factor contributing to the decay of muon S2 signals occurs within the circuitry of the PMT itself. A photomultiplier tube converts photons to a readable electrical signal through the photoelectric effect and a series of dynodes that amplify ejected electrons via secondary emission. For particularly high energy events that emit a lot of light, the last stage dynodes can create enough electrons to counteract the bias current of the PMT, unbiasing the PMT and (temporarily) halting the multiplication of electrons. Capacitors were put into place in the last 3 dynode stages to allow for reserve charge that maintains the voltage across dynodes, but even these will be limited by the charge that can be held on the capacitors. The decoupling capacitors discharge when necessary to "recharge" the system, but the finite capacitance of the system limits the recharge rate, which is seen in the S2 decay in prolonged muon events.

7.3 Simulation of Muon Track Geometries

A simple Monte Carlo simulation was used to study the effect of the angular distribution of muons underground on track geometries through the xenon detector. A sample of $N = 10^6$ muons was generated uniformly on the top surface of a cylindrical detector. The detector shape and size mimics LUX, and is simplified to a cylinder of radius 23.65 cm, height (cathode-gate distance) of 48.32 cm, and drift speed of 0.15 cm/μs, making the entire drift length of the detector 323 μs. For each muon, an azimuth angle ϕ was selected from a uniform distribution on $[0, 2\pi]$, and zenith angle θ was selected from the Miyake angular distribution appropriate for the depth of Davis campus as described by References [86] and

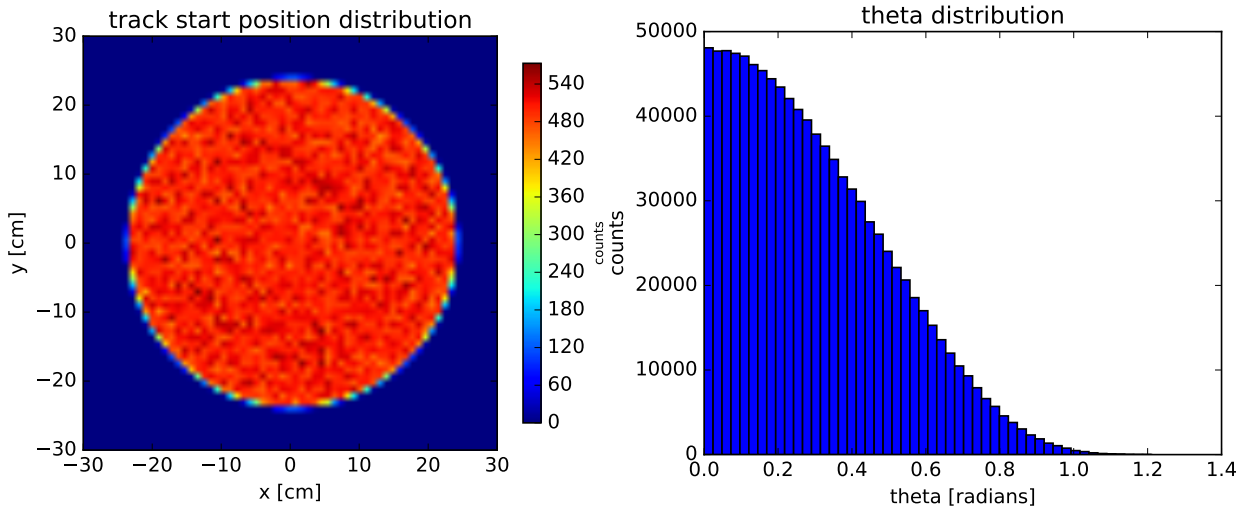

Figure 7.3: Starting positions were populated uniformly on a circle of radius 23.65 cm, the top surface of a cylindrical detector (left). The zenith angles were chosen from the Miyake angular distribution (right).

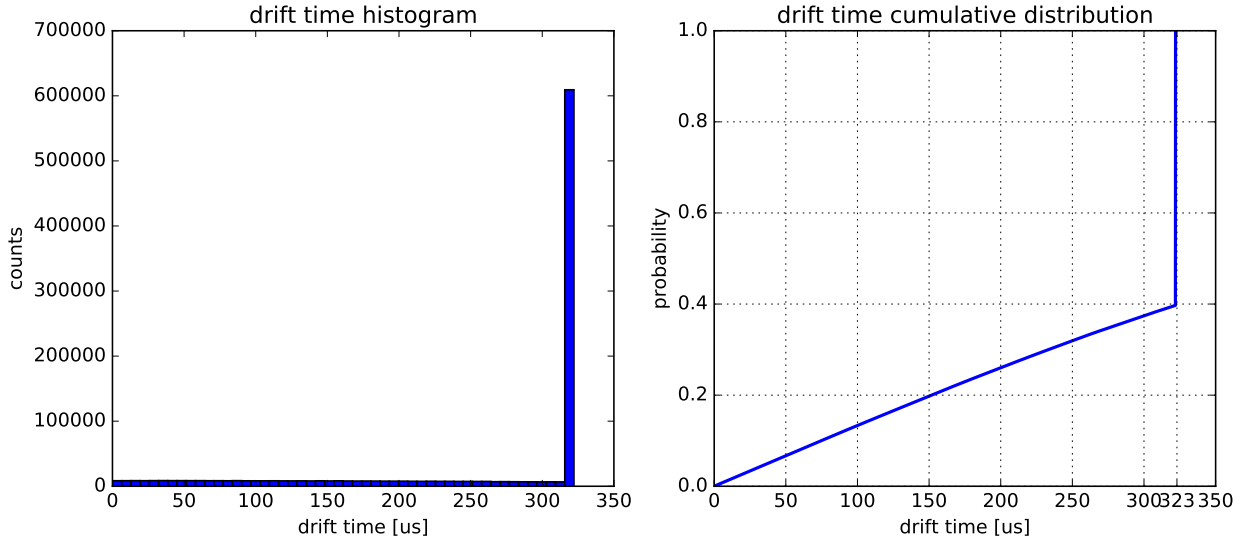

Figure 7.4: Left: Histogram of simulated drift times of muon tracks through detector. Drift time is directly related to the z-projection of the track in the detector. Right: Cumulative distribution of simulated drift times. 40% of the events are "clipping" events that do not traverse the entire drift length (cathode to gate) of the detector.

[77]:

$$I(\theta) = \sec\theta\, e^{-X(\frac{\sec\theta - 1}{\Lambda})}, \tag{7.1}$$

where X is the detector depth of 4200 m.w.e. and Λ is the empirically derived, depth dependent value of 700 m.w.e.

The muon either (a) exits through the side of the detector, resulting in a z-projection less than the detector height (drift time less than 323 μs), or (b) traverses the whole length of the detector. The simulated distribution of drift times is displayed in the left of Figure 7.4. Normalizing the total histogram area to one and calculating the integral up to each time t results in the cumulative distribution function (CDF). The CDF describes the probability that a muon's total drift time is less than or equal to a given value of t between 0 and 323 μs. We see 60.0% of muons entering through the top of the detector exiting through the bottom, and few have extremely short track lengths, shown in Figure 7.4. As seen in the zenith angle distribution, cosmic ray muons at this depth tend towards vertical orientations, even more so than at the Earth's surface where the CR muon zenith angles follow a $\cos^2\theta$ distribution. This results in very few muons at glancing angles with short drift times. Since "normal" S1-S2 events occurring near the top of the liquid Xe can be mistaken for these short-track muons, a cut on track durations will be made (Section 7.6.1) with little effect on detection efficiency.

7.4 Primary Cut: Simultaneous PODs

As discussed in Section 6.5, the timing of simultaneous events in the water and xenon was studied using LED pulses in both xenon and water spaces, signals originating from the same pulser. Due to differing delay buffer settings, water pulses appear approximately 150 samples (1.5 μs) before the xenon pulses in the DAQ, when in fact they are actually simultaneous. To start the search for simultaneous events in the Run04 data, events of interest were first chosen based on the presence of both a water POD and xenon POD, and their relative timing. Timing quantities are found in rq files, as calculated by the standard LUX processing pulse finding algorithms. If an event contained both a xenon POD and a water POD whose DAQ recorded start times were within a 100 sample window: 100 samples $< t_{0,Xe} - t_{0,water} <$ 200 samples, it was considered as possibly containing a Xe-water coincidence caused by a cosmic ray muon. Here, t_0 is the pulse start time as calculated by the standard LUX data processing PulseFinder algorithm. A total of 23,299 pairs passed this first timing cut, the vast majority of which are random in nature and later removed as a result of secondary cuts. A peak appears where coincident PODs are assumed to be around a timing difference of 147 samples, as seen in figure 7.5. This excess exposes a population of possible through-going muons, most with large event areas in the xenon detector.

Paired xenon-water PODs whose start times are within 101 and 110 samples of each other almost exclusively consist of PODs paired together through random chance, while pairs within 144 to 153 samples of each other will include most of the "true" coincidences caused by muons. Random coincidences are dominated by single photoelectron ($\sim$ 1 phe

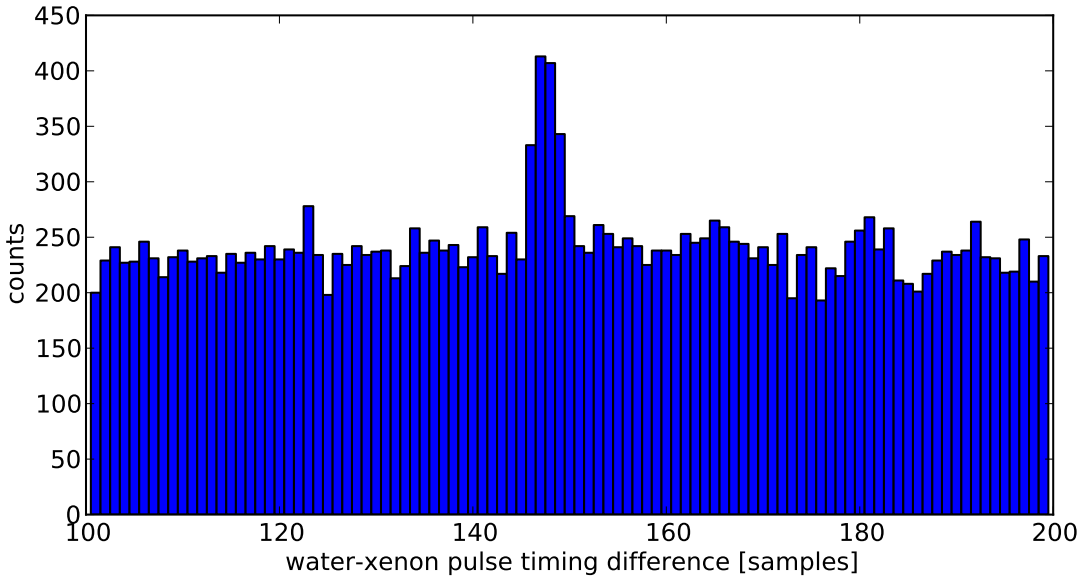

Figure 7.5: Histogram of time differences between water and Xe PODs recorded in the same event. The 150 sample offset has not been subtracted out here. A clear signal is seen around 150 samples, indicating "true" coincidences that may be caused by a throughgoing muon.

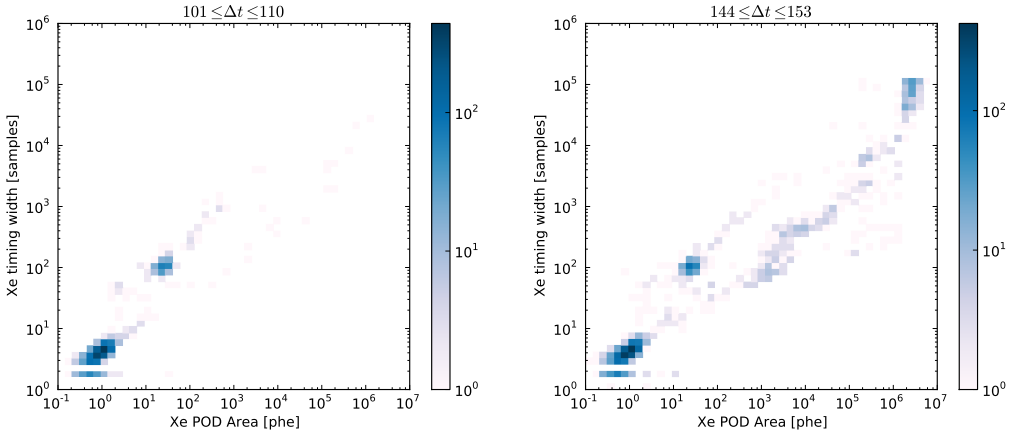

Figure 7.6: 2D histogram of Xe area vs. width for true and random coincidence timing windows. Left: Xe pulse quantities for Xe PODs paired with a water tank signals in the window 101 samples $\leq \Delta t \leq$ 110 samples, showing prominent single photelectron and single electron populations, pairs formed due to random chance. Right: window of 144 samples $\leq \Delta t \leq$ 153 samples, exposes larger xenon pulses belonging to true coincidences, originating from the same source as the water tank signal. The populations clustered around 1 phe Xe POD area correspond to single photoelectrons, while single electron emissions from the liquid xenon surface are seen clustered at 10 phe.

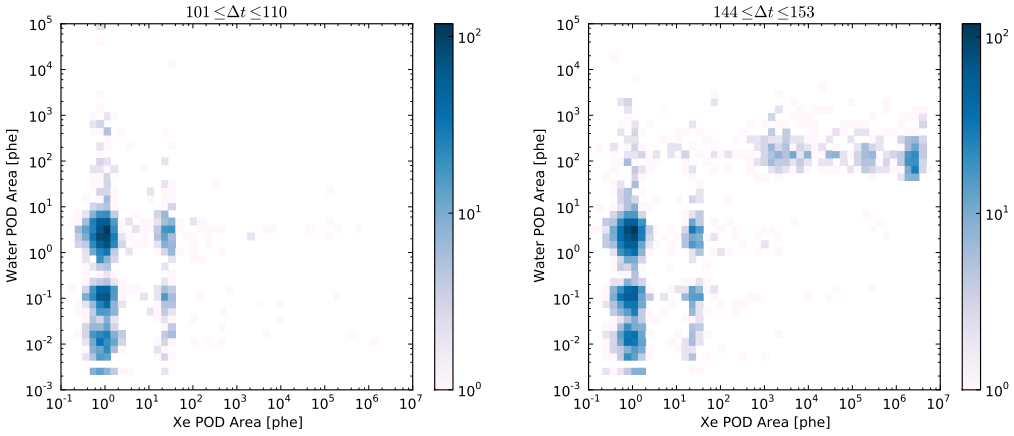

Figure 7.7: Similar to Figure 7.6, comparing areas of paired Xenon and water pulses. Population caused by throughgoing muons seen in the new dense spot that appears on right plot, with much larger Xenon and water areas than random pairs caused by single photoelectrons and single electrons.

area) and single electron ($\sim$ 10 phe area) PODs in the xenon space. Coincidences caused by muons exhibit much larger xenon pulse areas, as seen in Figure 7.6. Background β's and γ's in the water tank are the main causes of random coincidences from the water tank signal, and again, the water tank signals originating from high-energy muons appear with much larger pulse areas (see Figure 7.7).

7.5 Zoology of Simultaneous Events

Several different classes of "simultaneous" events were found, and prominent ones are described below. Plots show raw electronic output of the xenon PMTs in units of mV. The conversion to photoelectrons has not yet been applied, but conversion factors and gains were kept consistent across PMTs. This ensures that comparing raw output between individual PMTs can still describe relative light exposure intensities (when not saturated).

7.5.1 Top-entry Muon

The canonical throughgoing muon exhibits the shape described above in Section 7.2 and shown in Figure 7.2. The immediate S2 resulting from the energy deposition in the extraction region is highly localized in $x-y$ where the muon enters at the top surface, and the electrons originating from the active region appear in a prolonged S2. If the track also goes through the inverse field region (below the cathode), a prominent light signature can appear in a single PMT in the bottom array, though usually this will be undetectable, since S1 created in the active region will saturate the bottom PMTs. A raw waveform, summed across all active xenon PMT channels, is shown in Figure 7.8.

The effects of capacitor depletion are illustrated in Figure 7.9. In the immediate S2, a

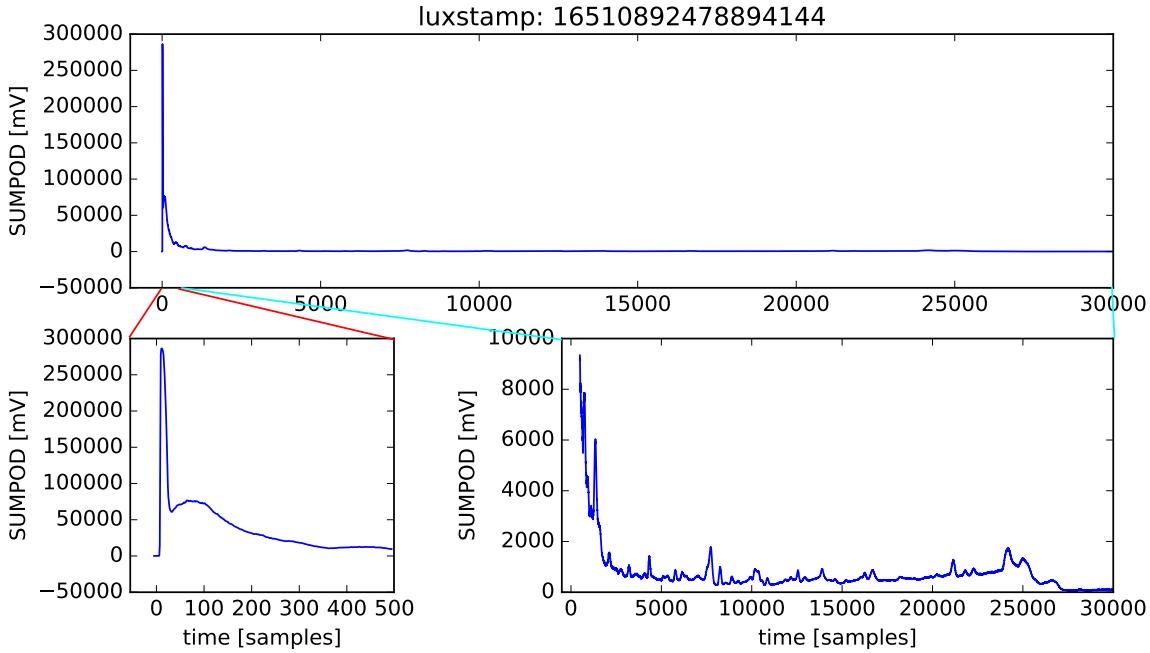

Figure 7.8: Top entry muon. The S2 signal overlaps with the initial S1 (zoomed in bottom left). S2 light continues to be generated until 27000 samples after the POD start (zoomed in bottom right).

cluster of high-output PMTs dominate the signal initially and even exhibit anode saturation when the signals reach a maximal output of 2.5V. These PMTs are closest to the muon entry point at the surface, where electrons are initially extracted, near (x, y) coordinates $(-15\text{cm}, 0\text{cm})$. Since these PMTs and their associated decoupling capacitors cannot maintain the necessary voltage for the duration of the S2, electron multiplication within the PMT will stop. These peaks die off early compared to the shape of the lower intensity peaks of the unsaturated PMTs located further from the extraction site. The PMT hit map at a later stage of the S2 shows an unphysical hit pattern without a clear centroid where extraction is taking place. Instead, an obvious "hole" is left where the signal had been dominant moments earlier, indicating PMTs that have suffered from capacitor depletion.

7.5.2 Side-entry Muon

Muons can also enter the xenon space through the side of the detector, never crossing the extraction region. The muon track still creates a line source in the detector. Instead of an immediate S2, the S2 is separated from the S1, the time gap dependent on the depth of the entry point. Since these events do not cross the Xe gas-liquid interface, they should be eliminated from consideration in the final muon flux calculation.

A raw summed waveform of a side-entry muon is shown in Figure 7.10. The S2 follows 5500 samples after the initial S1, and stops at 34000 samples, corresponding to an entry point of 8.25 cm below the extraction region, and an exit at or near the bottom of the detector.

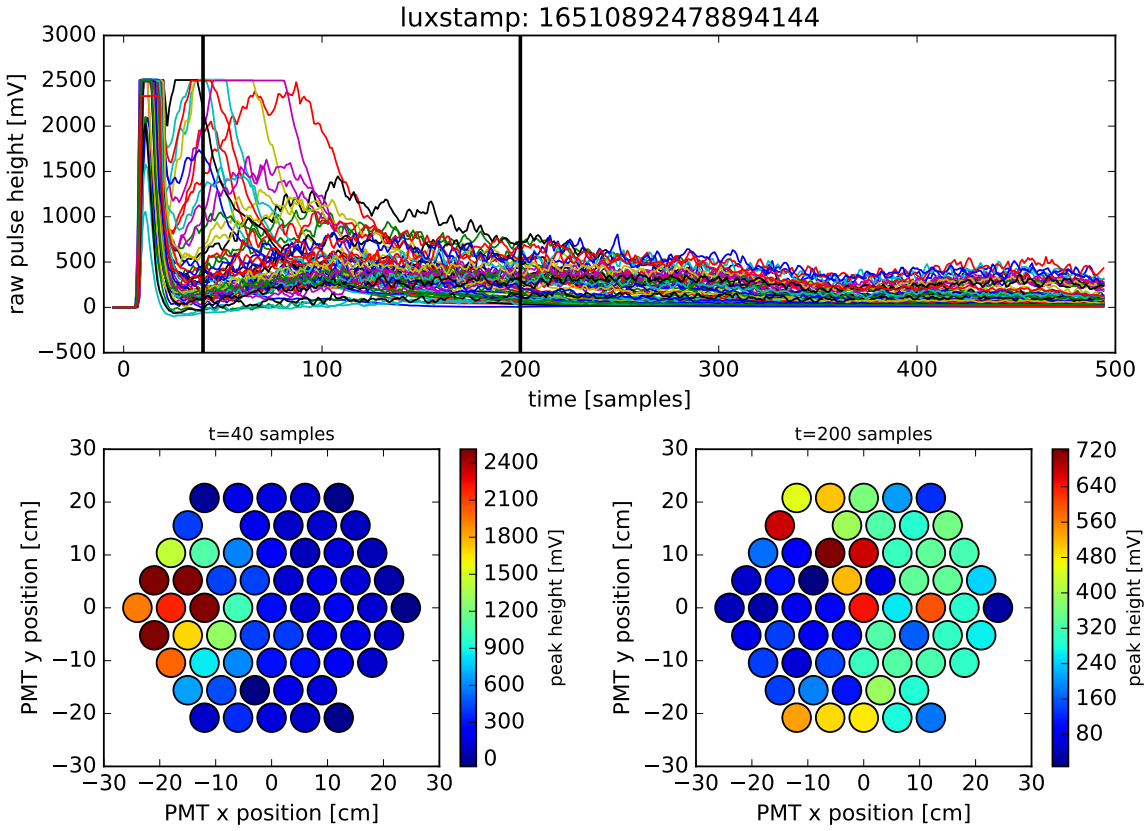

Figure 7.9: Capacitor depletion (top-entry). Individual peaks of the operational top PMTs shown (top). PMT intensity hit maps for the top PMT arrays at times before (bottom left) and after (bottom right) capacitor depletion takes effect. The "extraction site" near xy coordinates $(-15\text{cm}, 0\text{cm})$ initially dominates, but then become greatly suppressed. Bright signals can create enough secondary emission electrons within the PMT to counteract bias current and deplete reserve charge from coupling capacitors.

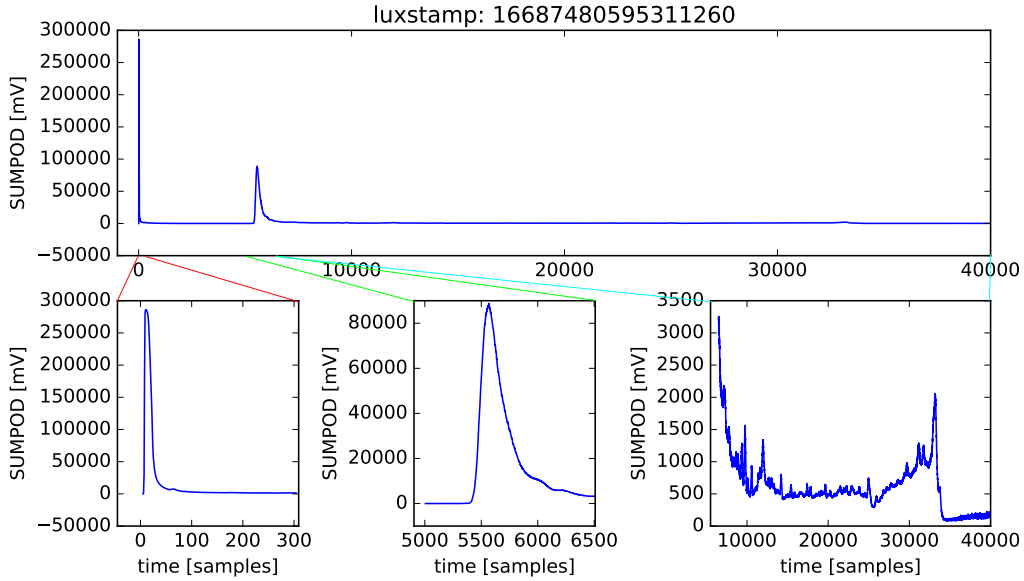

Figure 7.10: Side entry muon. S1 [left], S2 appearing after 5500 sample drift [middle] and suppressed S2 tail ending at 34000 samples [right]. Middle also shows significant decay of S2 signal in first 1000 samples, though the S2 signal will last for almost 30,0000 samples.

Side entry muons suffer from the same S2 decay from capacitor depletion effects described in 7.5.1, and the evolution of top PMT peaks and hit maps is shown in Figure 7.11.

7.5.3 Muon Byproducts

Muons can also create γ's, β's, and undesirable neutrons through interactions with detector components. These events may appear as single scatter or multiple scatter events within the xenon detector. The S1 and S2 sizes here are much smaller than that from a muon track. Part of the water tank veto's purpose is to identify such events as background and exclude them from consideration as WIMPs, especially if the event is caused by a muon induced neutron. Since these events usually don't involve an S1 overlapping with an immediate S2, they can be distinguished from top-entry throughgoing muons and excluded from the flux calculation.

An example of a particularlt complex byproduct coincidence is displayed in Figure 7.12. Several S1s and dozens of S2s appear within 350 μs of the Xenon-water coincidence trigger. With multiple events occurring, it becomes impossible to determine which S1s and S2s are grouped together as originating from the same interaction.

7.5.4 Random Coincidences

With an average trigger rate in the detector of $\sim$ 25 Hz, random coincidences between water and xenon spaces become inevitable. Most of these events in the xenon are single photoelectrons or single electrons, which are not of interest to the muon or dark matter search.

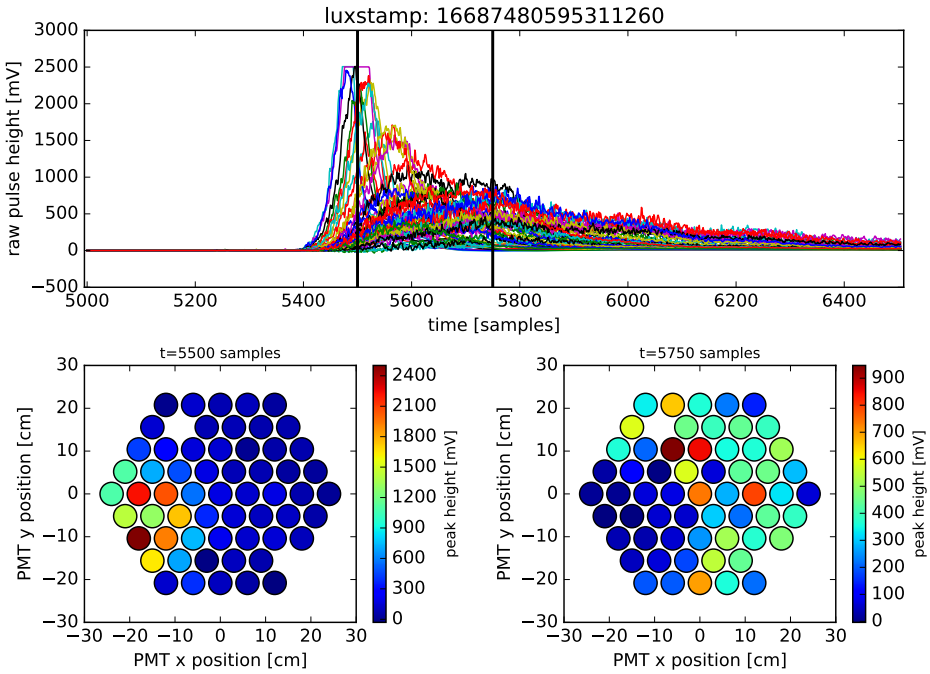

Figure 7.11: Capacitor depletion (side-entry). Extraction site near $(-15\text{cm}, -10\text{cm})$ initially dominates the signal, but then becomes suppressed.

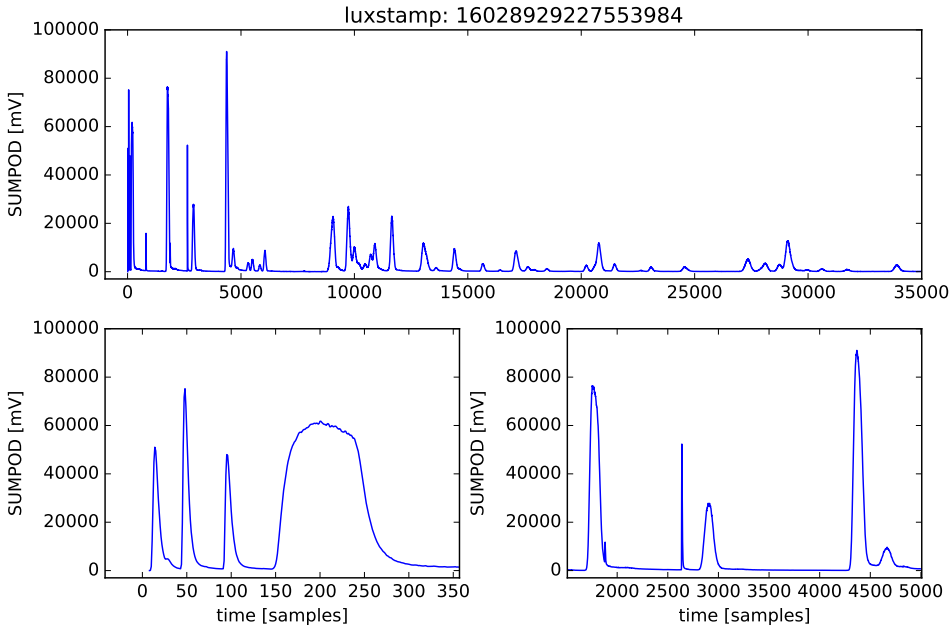

Figure 7.12: Muon byproducts. Several muon byproducts appear and multiple scatter within the xenon detector. A total of 6 S1s are identified in this event and several dozen S2s. Activity persists for 35000 samples after the initial muon trigger from the water tank.

Appropriate cuts on pulse area and timing can eliminate most of these from consideration, and are described in the next section.

7.6 Secondary Cuts

A series of cuts is used to further refine the sample of possible throughgoing muons. Values calculated from LUX rqs are used to eliminate non-top-entry muons. Values are chosen conservatively to keep detection efficiency high, as the main objective of these initial cuts is to obtain a reasonably sized sample of events for the processor-heavy task of examining events in their raw form. Once this sample is identified, raw evts are examined to determine pulse shapes and quantities specific to throughgoing muons.

7.6.1 Xenon Pulse Cuts

Upon applying the first timing cut, a sample is obtained where possibly simultaneous signals in the water and xenon detectors have occurred. Most of these are random coincidences, where the signals were generated independently, not originating from the same source. Inspecting the xenon events, pulse area and pulse duration can be used to identify various populations of xenon events (see Figure 7.6). Single photoeletrons have areas around 1 phe, and single electrons areas of 10-100 phe. S2s and prolonged S2s such as those caused by muon tracks will last over 100 samples and have areas over 100 phe. Requiring that pulse area be greater than 100 phe will help to isolate the prolonged S2 events that are the hallmark of a throughgoing muon and false signals caused by single electrons will be eliminated. The effect of this cut on detection efficiency turns out to be negligible, as only the shortest, corner-clipping tracks through the detector might become eliminated.

By design, the dominant source of radioactive backgrounds in the LUX detector is the xenon PMTs. Activity from the top PMTs can cause ER events near the liquid surface that can potentially look like short-track muons clipping the liquid in the extraction region. A cut requiring that a timing width on the xenon pulse be greater than 500 samples helps to eliminate most of such S2s occurring near the surface. Here the timing width is defined as $t_2 - t_0$, where t_2 is the pulse end time rq determined by the LUX DP PulseFinder, and t_0 the pulse start time.

Assuming that there is no S2 fall time or vertical dispersion for traversing muons, the 500 sample cut eliminates clipping muons with extended drift times less than 5 μs. Simulations show (Section 7.3) that less than 0.42% of muon events will be eliminated as a result of this cut, though due to the uncertain nature of the angular distribution of muons entering the Davis cavern, this warrants further inspection.

7.6.2 Water Pulse Quality Cuts

Figure 7.13 compares water pulse areas to the difference between water and Xe pulse start times calculated in the primary cut. A population of pulses with areas of order 10^2 phe is

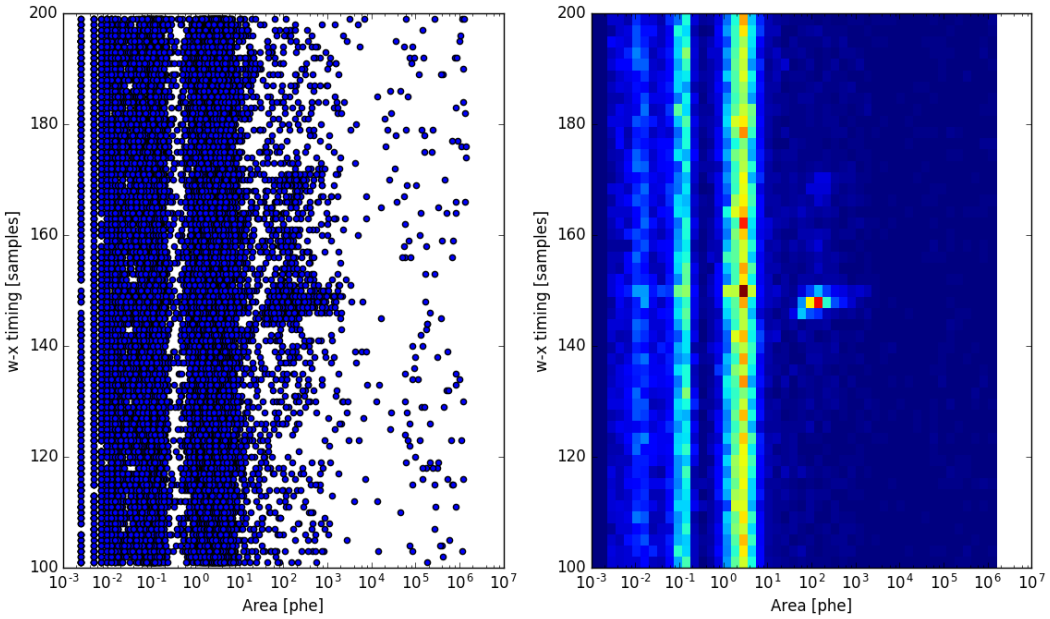

Figure 7.13: Water tank pulse area vs. water/xenon timing difference. The population of 10 phe pulses is spread uniformly in water/xenon timing differences, suggesting that these coincidences are random in nature.

seen distributed closely about 1.5 μs, indicating true simultaneity between xenon and water signals. Another population of water pulses with areas between 1 and 10 phe, attributed to β backgrounds, distributes itself more uniformly in time, indicating that these events occurred within the 100 sample window of a xenon signal by random chance. Similar populations of water pulses with areas less than a phe are indicative of spurious veto electronics noise recorded by the DAQ, as will happen in the presence of a xenon PMT trigger. A cut requiring water pulse area be greater than 10 phe eliminates most of these random coincidences caused by βs, γs, and water PMT noise, while leaving the long-track muons through the water for further study.

When an event is triggered by an interaction occurring in the xenon space, all activity in the water tank will be recorded for the duration of the event. If nothing of interest is occurring in the water tank, readouts still may get recorded as individual water PMT baseline levels spuriously fluctuate. This random noise is cut out by requiring that the water coincidence (number of water pmts above threshold) be at least 5. As described in Section 6.4, the MALU is a coincidence counter for water tank PMTs, and water tank triggers are recorded when some minimum number of PMTs break above threshold. This minimum number varied between 4 and 5 throughout the run, but this variation turns out to have no effect on identifying muons that go through the xenon volume. Because the xenon detector is situated in the center of the water tank, any throughgoing muon will necessarily traverse through at several meters of water, generating enough light to reach much more than 5

water tank PMTs, usually more than 15 (where the coincidence counter maxes out). A cut of $wcoin \geq 5$ maintains consistency in water PMT coincidence minimums for all datasets used.

7.6.3 Top-bottom Asymmetry

The pulse finding algorithm employed in the standard LUX data processing sequence is not entirely suitable for characterizing high-energy muons in the xenon space. However, top-bottom asymmetry (TBA, defined in Section 4.6) can be used to distinguish side-entry muons and muon byproducts from muons that entered from the top surface. A top-entry muon will have S1 and S2 starting essentially at the same time, overlapping so that the pulse finder registers them as a single, long pulse. The top-bottom asymmetry for this smeared-together POD will usually be dominated by the long S2, with a value centered about 0. A side-entry muon and muon byproducts will usually have separation in time between S1 and S2 and be recorded as two distinct PODs, and later the S1 and S2 will be identified as two distinct pulses. In this case, the S1 is the xenon pulse coincident with the signal in the water tank. This S1 will be shorter in duration than the top-entry POD, and more of the light will appear in the bottom PMTs due to reflections occurring at the liquid/gas interface.

While a more liberal cut on pulse duration could have the undesirable effect of cutting out short track-length top-entry muons, a cut on top-bottom asymmetry (eliminating events with tba < -0.50) eliminates many lone S1 pulses in events with with well-separated S1-S2. In Figure 7.14 the lone S1s are seen with t-b asymmetries and areas below the main population of events with values distributed about zero. This cut is expected to eliminate less than 0.5% of top-entry muon events that are dominated by light in the bottom PMT array.

A "trail" appears in Figure 7.14 at around 10^5 phe where TBA appears to grow with pulse area. These correspond to the S1s of side entry muons with their relatively large pulse areas, and the climb in TBA stems from anode saturation in the xenon PMTs. Once a PMT's anode saturates completely, its signal will "flatline" at the PMTs maximum output. For extremely large S1 pulses, many of the bottom PMTs will saturate and artificially alter the observed TBA since the peak areas from the bottom PMT array will be limited by this saturation. Thus for larger and larger S1 pulses, TBA appears more symmetric as top PMT peaks grow and bottom PMT peaks have reached their saturation point, explaining why larger S1s exhibit TBAs approaching zero.

7.6.4 Pulse Shape Analysis

366 water-xenon POD pairs remain after applying the previous mentioned cuts on xenon and water RQs. Since relevant information on throughgoing muons is lost after processing down to the reduced quantities, a closer look at the raw waveforms is required to better identify top-entry muons.

As described before, the light signal can be described in 3 stages: (a) initial S1 with height

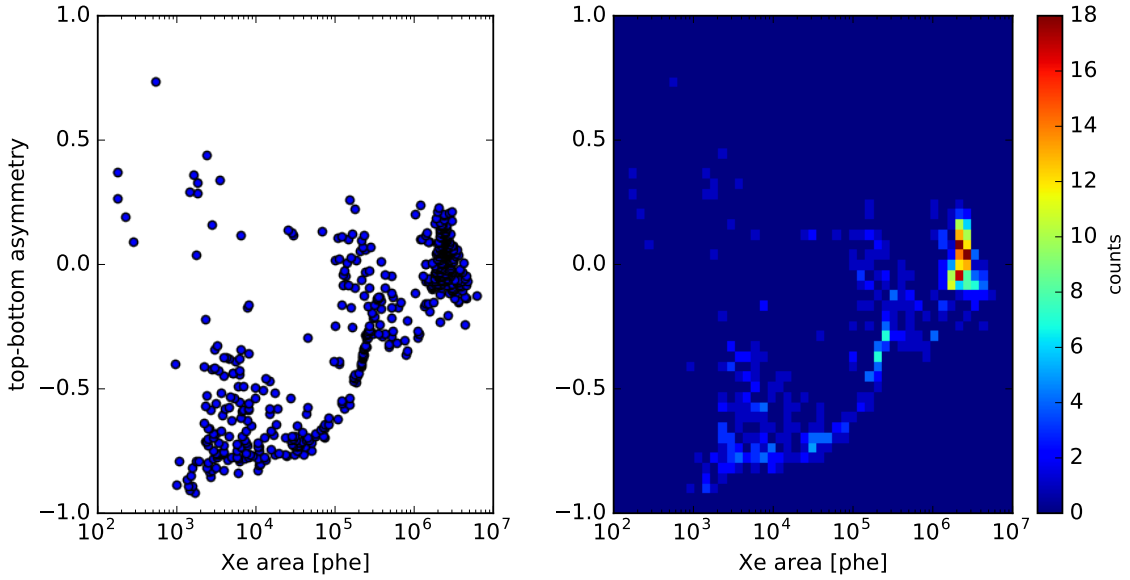

Figure 7.14: Top-bottom asymmetry of Xe pulses found coincident with water pulses, xenon pulse width cut employed. Lone S1s not associated with muons appear with areas around $10^3 - 10^4$ phe, while lone S1s from throughgoing muons have areas $10^5 - 10^6$ phe. Top-entry, throughgoing muons appear in the dense blob above 10^6 phe.

proportional to track length, (b) large, localized in x-y S2 originating in the extraction region, and (c) a long-lasting S2 from the active region, duration proportional to the z-projection of the track in the xenon detector.

Because there is significant overlap between these stages, precise cutoffs don't exist; however, certain signatures of a stage's dominance are observable. In (a), the S1 max occurs within 10 samples of the pulse starting to rise, and more light appears in the bottom PMTs. Often the amount of light created in this stage is enough to completely saturate the anodes of the xenon PMTs. In (b), the immediate S2 from the extraction region peaks around a cluster of top PMTs 100 samples after the pulse start, located at the x-y position of the extraction site. The PMTs closest to the extraction site will often display capacitor depletion effects, and their output dies off despite S2 light still being created, as can be seen in the PMTs further from the extraction site that are not yet saturated. By 200 samples after the pulse start, most of the ionization electrons originating from the extraction region should be extracted, and electrons from the active region drift into the extraction region for stage (c). The active region electrons will enter the extraction region at a slower rate due to the weaker electric field in this region, creating less S2 than the original extraction region electrons. The signal can be further suppressed, again, because of PMT capacitor depletion.

Identifying the overlap between stages (a) and (b) becomes key for tagging top-entry muons. The next subsection describes how the evolution of top-bottom asymmetry can be used to determine overlap between S1 and S2.

Evolution of Top-bottom Asymmetry

In a top-entry muon, S1 initially dominates with its quick rise time, but soon the S1 decays and S2 starts to rise. For shorter height S1s it may be difficult to identify such a switch based purely on sumPOD waveforms, but the differences in top-bottom asymmetry between S1 and S2 offers another way to evaluate the presence of S1/S2 overlap. S1 light is primarily captured in the bottom PMTs resulting in a more negative top/bottom asymmetry, while S2 will be more evenly distributed between top and bottom. When plotted with respect to time, top-bottom asymmetry will exhibit a distinct rise as the negative top-bottom asymmetry of the S1 loses out to the growing S2, see Figure 7.15. Figure 7.16 shows that this method will even help reveal small S1 that may have otherwise been been dwarfed by its associated, immediate S2.

The rise in top-bottom asymmetry occurs within a narrow window, during the fall of the S1, which occurs within 30 samples of the S1 rise with a decay constant of tens of nanoseconds. Top-bottom asymmetry before and after this window will usually be an unreliable indicator of the dominance of S1 or S2 due to saturation effects. The S1 before will usually cause anode saturation in PMTs, concealing information about relative pulse heights. The S2 afterwards can suffer from capacitor depletion, eventually suppressing the most intensely hit PMTs in the top array. Decay from capacitor depletion is seen to start to cause decay after ≈ 35 samples of complete anode saturation, later for lower outputs. Luckily, this occurs after the decay of even the largest S1s observed, allowing for the observation of the transition of power between top and bottom PMT arrays.

POD End Times

The presence of electron trains following a large S2 can hide the actual t_2 end time of an S2. In an effort to reliably reflect a recoil event's energy, the LUX pulse finding algorithm includes these delayed electron emissions. This results in a systematic overestimate of S2 pulse widths, which is unimportant information for WIMP search. While the cut on rqs described in Subsection 7.6.1 will be sure to only eliminate PODs less than 500 samples, many pulses under 500 samples long will remain under consideration as a throughgoing muon due to the stretched timing caused by including electron trains. The search for throughgoing muons depends on these timing widths, so a scan through the raw data is done to determine more accurate S2 end times to further enforce the 500 sample timing cut made on rq values. End times are calculated based on correlations of light signatures between top and bottom PMT arrays, using POD height and instantaneous top-bottom asymmetry.

Light emitted by electron trains can be continuous when considered summed across all PMTs, but the phe per sample created will be less than that from S2s. Also, when examining single PMTs, electron trains will appear as individual single photoelectrons and single electrons popping out of the liquid surface sporadically, creating a spiky "grass" waveform instead of the smoother, continuous forms formed by S1s and S2s. The deviation of top-bottom asymmetry is used to identify when output starts to look like an electron train. Due to the lower output height and sporadic nature of e-trains, tba will start to vary wildly from

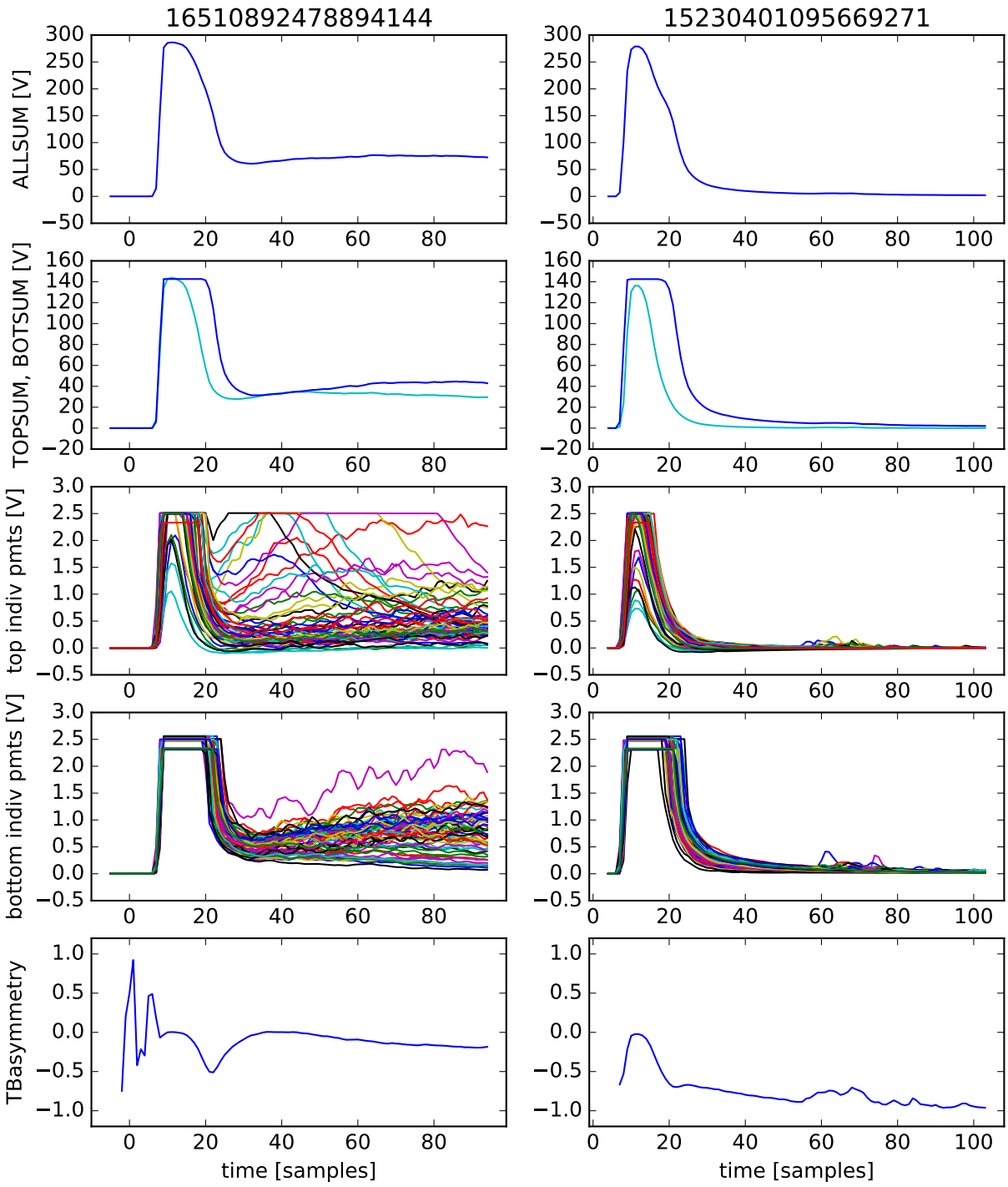

Figure 7.15: Evolution of top-bottom asymmetry: overlap and lone S1. Left: a top entry muon, with S1 and S2 overlap evident during the fall of the S1, [$t = 25$ samples], a concurrent uptick in top-bottom asymmetry is seen. Right: a side-entry muon with well separated S1 and S2, no rise in top-bottom asymmetry occurs during the S1 fall: light continues to only come from S1, dominating the bottom PMT array. In TOPSUM, BOTSUM plots (row 2), summed top peaks shown in teal, bottom in blue.

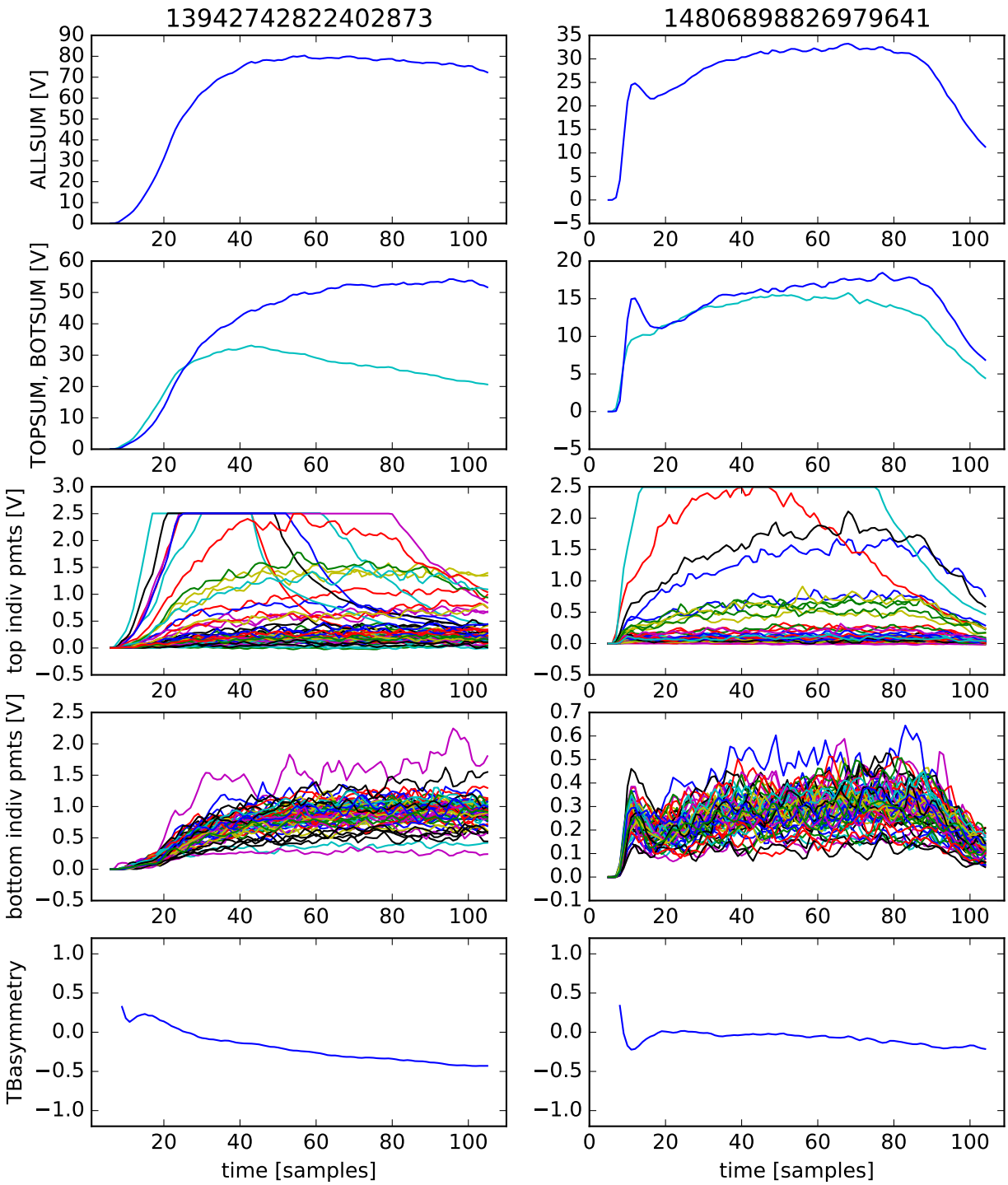

Figure 7.16: Evolution of top-bottom asymmetry: small S1. Small S1 may be hidden by simultaneous large S2, but both displayed events would be considered as possibly containing S1-S2 overlap based on the notched shapes at the start of the tba curve (bottom). Such small S1s probably come from ordinary recoil events instead of throughgoing muons, and can be eliminated with pulse width cuts.

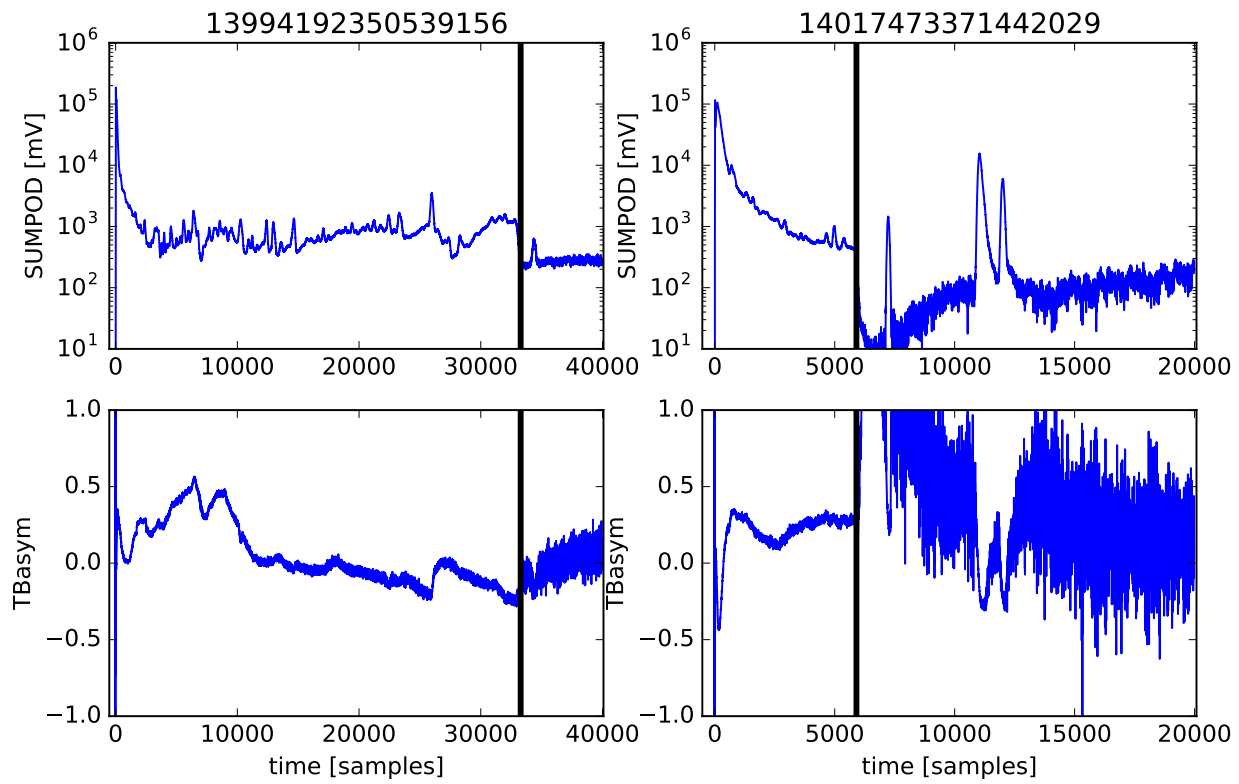

Figure 7.17: POD cutoff (large). POD end times were found using raw waveforms and top-bottom asymmetry, two events shown. Note log scale on y-axis. Calculated end times denoted by black vertical line. Left: rq determined $t_2 = 99984$ samples, re-analysis of waveform yields $t_2 = 33277$ samples. Right: rq determined $t_2 = 36146$ samples, re-analysis of waveform yields $t_2 = 5905$ samples.

sample to sample when an S2 stops and e-train begins. This causes a steep ascent in the tba standard deviation in a given timing window, and the time of this ascent is used to determine a pulse's end time when obscured by e-trains. Examples of end times found with this method are shown in Figures 7.17 and 7.18. Figure 7.18 shows an event with a pulse width greater than 500 samples as calculated by rq values, whose end time is calculated to be less than 500 samples. Such events are eliminated from consideration for top-entry muons.

7.6.5 Summary of Cuts

This chapter has outlined the process of identifying throughgoing muons in the LUX xenon detector. Conservative cuts are first performed on processed rq values, shrinking the sample of events examined for the processor-heavy task of analyzing raw waveforms. A summary of the cuts is displayed in Table 7.1. Finally, 195 throughgoing muons are identified for the full LUX Run04 exposure.

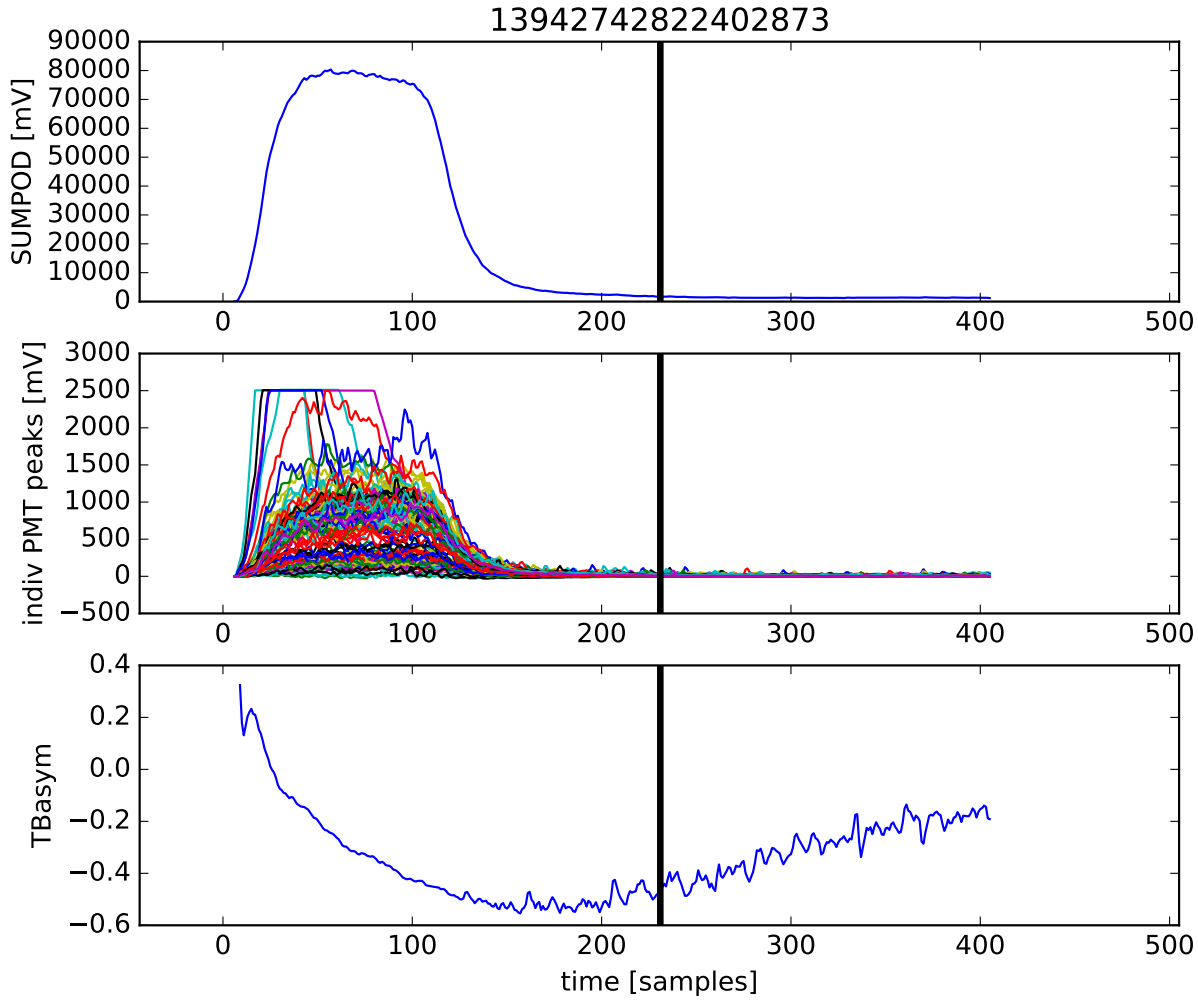

Figure 7.18: POD cutoff (small). Calculated end time: $t_2 = 220$ samples. RQ-calculated end time: $t_2 = 6358$. This pulse passed the initial RQ timing width cut, but was eliminated in the raw-waveform-determined timing cut.

Cut	Criterion	Events remaining
Primary cut: simultaneous water-Xe pulse timing (Section 7.4)	$\lvert t_{0,Xe} - t_{0,water}\rvert < 50$ samples	23 229
Xe pulse area (SE and sphe elimination, Section 7.6.1)	Xe area > 100 phe	1 043
Xe pulse width (Section 7.6.1)	$t_{2,Xe} - t_{0,Xe} > 500$	628
Water pulse area (Section 7.6.2)	Water area > 10 phe	429
Water MAjority Logic Unit (Section 7.6.2)	w_coincidence > 5	425
Xe top-bottom asymmetry (Section 7.6.3)	TBA > -0.5	372
Xe pulse shape analysis (Section 7.6.4)	analysis of raw waveforms	195

Table 7.1: Summary of throughgoing muon identification cuts.

Chapter 8

Muon Flux in LUX

8.1 Counted Muons

A total of 195 pulses were revealed as throughgoing muons using the method outlined in the previous chapter. Datasets and luxstamps specific to the considered events are listed in Appendix A. Distributions of associated pulse values are displayed in Figure 8.1. These distributions can help with future muon identification studies in LUX, and will also indicate the effect the cuts described in Sections 7.4 and 7.6 have on the observed count.

As seen in Figure 8.1, cosmic ray muons going through the xenon volume exhibit total pulse areas of $\sim 10^6$ phe. Xe pulse heights pile up at $\sim 1.3 \times 10^4$ phe per sample where PMT output maxes out. Xe pulse durations range from 500 samples (one of the secondary cuts in Subsection 7.6.4) to $\sim 3.5 \times 10^4$ samples (corresponding to the full drift length of the detector), with the bulk of the events traversing the entire drift length of the Xe volume, as expected from Section 7.3.

Throughgoing pulses in the water Cherenkov detector range from 35 to 1000 phe in pulse area, 5 to 150 phe per sample in pulse height, and 15 to 60 samples in pulse duration. The timing difference between the calculated start times of the xenon versus the coincident water pulse peaks sharply at 147 samples (or 1.47μs), corresponding to the 1.5μs difference in delay buffer settings between water and xenon systems - an indication that the pulses are simultaneous. An additional timing peak occurs at 169 samples, a result of the water pulse classifier including pickup noise as a part of the pulse, identifying a start time up to dozens of samples earlier than the actual pulse rise. The TTE signal for all coincident veto-xenon events identified the veto (and not the xenon PMTs) as the cause for the trigger.

Top-bottom asymmetry in the xenon space is close to zero due to the dominance of the long-lived S2 light, which will register in both the top and bottom PMT arrays somewhat equally. The number of water PMTs active in the waveform, wcoin, ranges from 13 to 15, where 15 is the maximum observable by the MALU output. With the exception of xenon pulse duration, the above pulse quantities come directly from rqs as calculated by the standard LUX data processing scheme. Xenon pulse duration values are as calculated by the additional pulse shape analysis method described in Section 7.6.4.

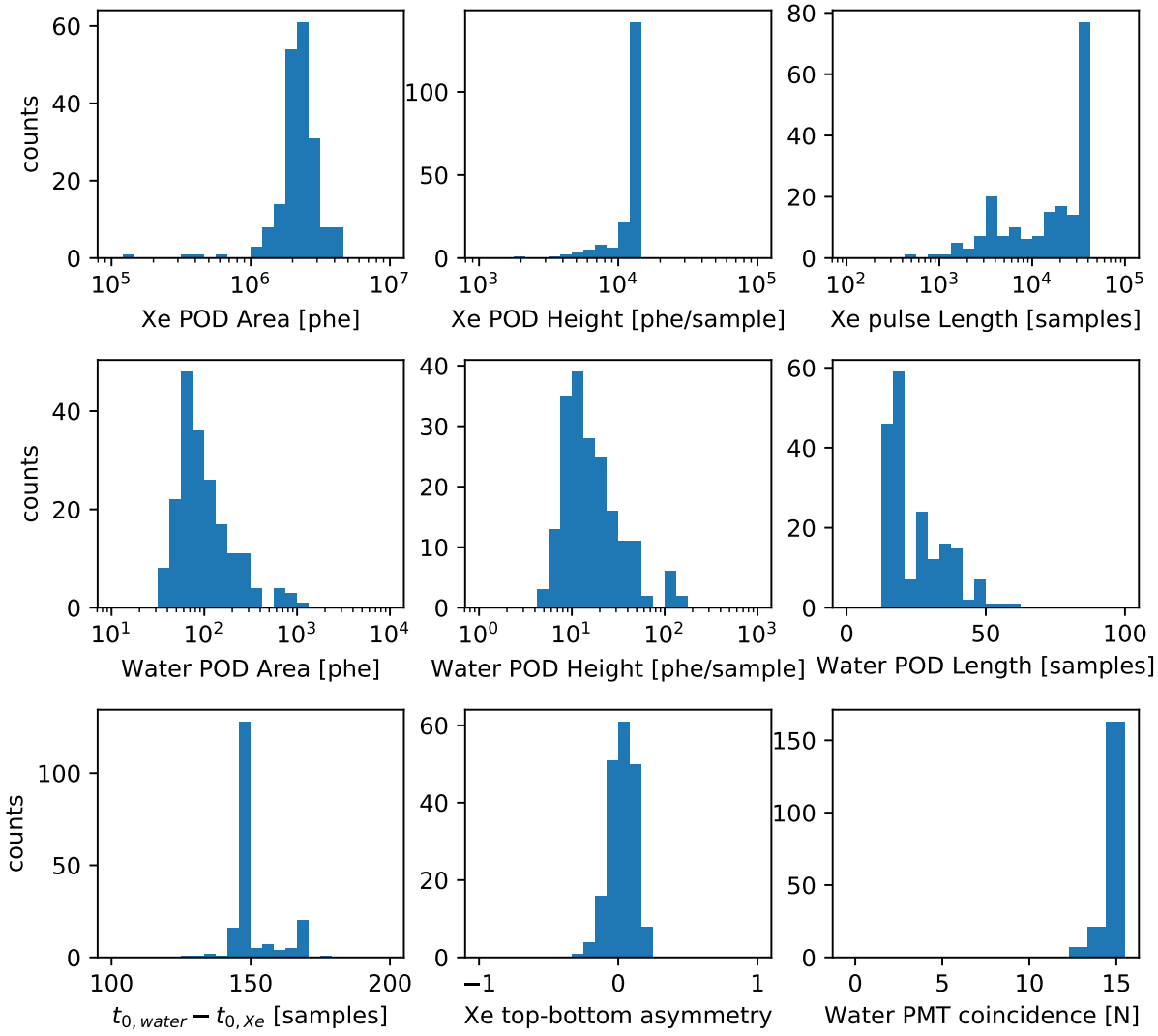

Figure 8.1: Pulse characteristics of throughgoing muons. Distributions of relevant pulse characteristics from the 195 events considered as throughgoing muons are displayed above.

YYYYMM	livetime (s)	deadtime (s)	LIVETIME(DAYS)	DEADTIME(DAYS)
201412	347973.4905	19009.96388	4.027470955	0.22002273
201501	1450842.112	89372.59515	16.79215408	1.034405036
201502	1207550.874	47052.23546	13.97628327	0.544586059
201503	898345.7175	20056.13151	10.39751988	0.232131152
201506	1937905.71	40722.86931	22.42946424	0.471329506
201507	1994719.066	41821.77073	23.08702623	0.484048272
201508	2139574.567	135449.4674	24.76359453	1.567702168
201509	1738833.29	71863.46794	20.1253853	0.831753101
201510	1226631.747	42864.84759	14.1971267	0.496120921
201511	1726177.484	65702.32159	19.97890607	0.760443537
201512	1854738.615	42901.18727	21.46688212	0.496541519
201601	1993000.816	55270.32144	23.06713907	0.639702794
201602	864894.4124	25514.82078	10.010352	0.295310426
201603	2068501.112	53072.0396	23.94098509	0.614259718
201604	2094962.092	60470.44052	24.24724643	0.699889358
TOTALS	23544651.11	811144.4801	272.507536	9.388246298

Table 8.1: Detector livetime by month

8.2 Detector Livetime

Livetime is calculated by using the latch and end times clocked for each individual dat file, which corresponds to a filled memory bank in the DAQ. Dead time between memory banks is already accounted for ($\approx 3.3\%$ effect). Livetime by month is displayed in Table 8.1. Since livetime is calculated for each memory bank using the precise 100 MHz clock of the DAQ, any uncertainty in livetime is considered completely negligible. A total of 272.5 live-days, or 2.354×10^7 live-seconds, of WIMP-search data was taken with veto PMTs operational during the LUX Run04 science campaign.

8.3 Cross-sectional Area of Xe Detector

There is some uncertainty in the area the area of the surface through which flux is being calculated, and this section builds upon studies outlined in Reference [108]. As described in Section 4.2, the active region is surrounded by a dodecagonal structure of teflon reflector panels, see rendering in Figure 8.2. The panels were constructed at room temperature, and as the detector was cooled to its operating temperature of 173K, the panels thermally contracted down to an estimated radius of 23.65 cm. Here radius is defined as the perpendicular distance from detector center to a flat face of the reflector panel. The uncertainty in the cold radius is calculated from the uncertainty in the warm radius (0.03 cm, as stated in the detector's technical drawings) and the uncertainty in the coefficient of linear thermal expansion (CLTE)

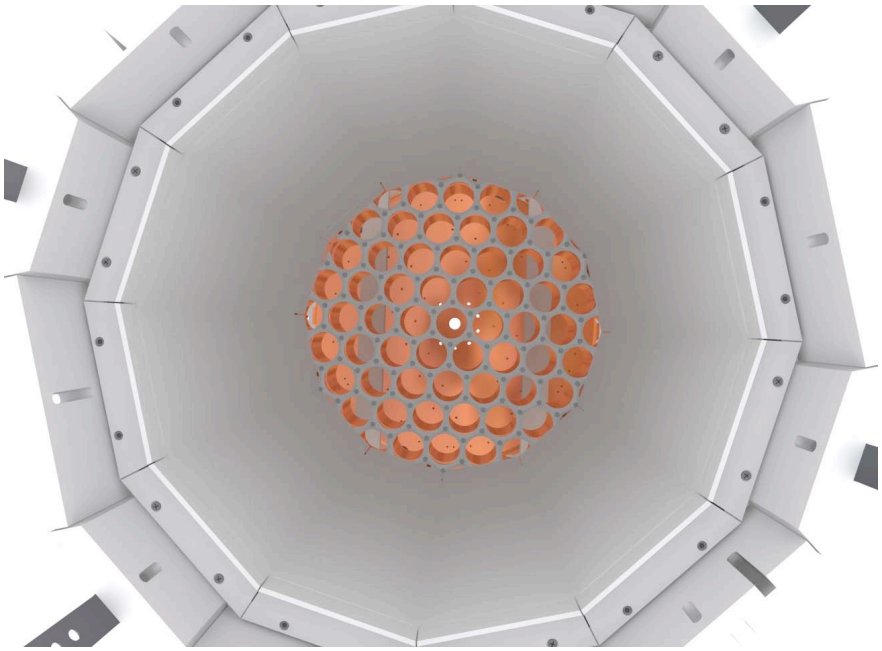

Figure 8.2: Inside the LUX detector, a view from below. A dodecagonal structure of teflon panels defines the cross-sectional area of the detector. Image taken from a series of detector installation drawings [Reference [109]], all lengths assumed warm.

for both teflon and the stainless steel to which the panels are pushed against. These combine to obtain the total uncertainty in cold radius: $\sigma_{cold} = 0.05$ cm.

The area of a regular dodecagon with relation to this inner radius r is $A = 12(2-\sqrt{3})r^2$, leading to an area of 1798.44 cm^2 for the liquid detector surface. The uncertainty in area is $24(2-\sqrt{3})(23.65 \text{ cm})(.05 \text{ cm}) = 7.60$ cm^2, or 0.42%.

8.4 Errors and Systematics

8.4.1 Random Coincidence Rates

The water tank/xenon volume detector system serves as a coincidence counter for muon events that traverse the xenon volume. While the pulses produced in both water and xenon by a through-going muon will exhibit unique characteristics, it is still possible that some of the coincident pulse pairs considered are random in nature, rather than originating from the same muon. Knowing the rate of such accidental coincidences will refine our understanding of the genuine coincidence rate (from Reference [105]).

If a random process occurs at an average rate r, the probability P_0 of finding *no* pulses during time interval T is given by

$$P_0(T) = e^{-rT}, \tag{8.1}$$

giving the probability of finding one or more pulses during time interval T:

$$P_{1+}(T) = 1 - e^{-rT}. \tag{8.2}$$

Typically *resolving time* T is shorter than the [inverse of] rate r considered, or $rT \ll 1$, and the exponential in Equation 8.2 can be approximated to first order:

$$P_{1+}(T) = 1 - e^{-rT} \approx 1 - (1 - rT) = rT. \tag{8.3}$$

Suppose two independent Poisson processes occur with rates r_1 and r_2. The probability P_{AC} of an accidental coincidence of Event 1 and Event 2 within interval T is the product of the two individual probabilities

$$P_{AC} = (r_1 T)(r_2 T), \tag{8.4}$$

and the rate r_{AC} of accidental counts is the probability per unit time,

$$r_{AC} = r_1 r_2 T. \tag{8.5}$$

The above result will be used to consider the accidental coincidence of several different classes of events.

8.4.2 Trapped Electrons on the Liquid Surface

The extraction region between the gate and anode grids has an electric field of 3.5 kV/cm. As discussed in Section 4.2.1, this corresponds to an extraction efficiency of 75%. This leads to a variety of pathological electron extractions that result from charge that has been trapped on the surface, instead of from the drifted electrons that create S2. Electron trains following large S2 can thus deceptively elongate pulse widths. While identification of top-entry muons will not be affected by electron trains, they become important when considering the 500 sample pulse width cut. This cut is meant to eliminate the "background" of recoil events occurring near the liquid surface, which may exhibit the overlapping S1-S2 template that is the hallmark of a top-entry muon.

Trapped electrons can also be extracted in what has been dubbed electron burps (e-burps). These emissions are similar to electron trains, but instead of exhibiting a decay over a period of ms like an electron train, the shape exhibits a distinct rise and fall over a time of hundreds of μs. Hundreds to thousands of electrons are emitted, for an order of 10^5 phe detected. Figure 8.3 shows an e-burp lasting nearly 40,000 samples with an area of 2.14×10^5 phe.

The likelihood that an e-burp is paired with a lone S1 can be calculated using the counting statistics of random events. E-burps occur in less than 1% of events recorded by LUX. This rate is determined from hand-scans performed as a part of LUX data quality monitoring, as e-burp events are not recognized by the LUX Pulse Classifier. Using the detector event rate of 25 Hz, the e-burp rate is estimated to be 0.25 Hz. The average S1 rate of 3.32 Hz is determined by the S1 pulses classified as such by the LUX Pulse Classifier. The overlap

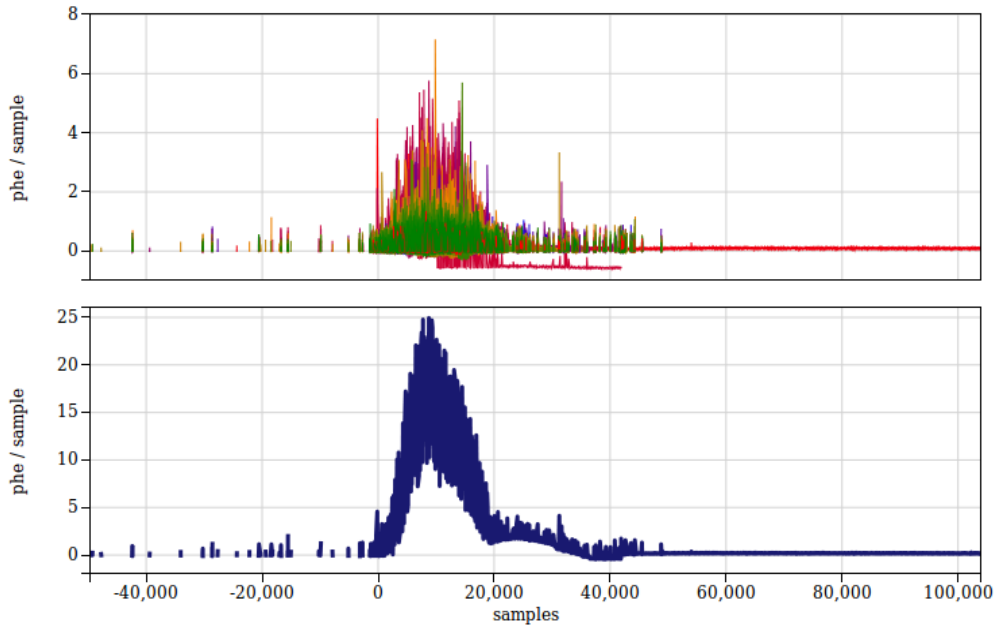

Figure 8.3: Electron burp. These anomalous waveforms result from trapped electrons on the liquid surface and last for tens of thousands of samples.

window between S1 and S2 for top-entry muons is less than 35 samples, as mentioned in Section 7.6.4. An S1/e-burp random coincidence will occur within a 35 sample (350 ns) window at a rate of $r_{S1/eburp} = r_{S1} r_{eburp} T_{window} = (3.32\ \mathrm{s}^{-1})(0.25\ \mathrm{s}^{-1})(350 \times 10^{-9}\ \mathrm{s}) = 2.9 \times 10^{-7}\ \mathrm{s}^{-1}$.

Furthermore, this S1/e-burp pair must coincide with a water tank pulse within a 50 sample window. The veto sumPOD rate is 1.1 Hz. The coincidence rate is further reduced to $r_{Xe/water} = r_{Xe} r_{water} T_{window2} = (2.9 \times 10^{-7}\ \mathrm{s}^{-1})(1.1\ \mathrm{s}^{-1})(500 \times 10^{-9}\ \mathrm{s}) = 1.60 \times 10^{-13}\ \mathrm{s}^{-1}$

Note that this is an extremely conservative estimate because the S1 and veto rates do not take into account pulse sizes, so pulses that are cut in the veto-Xe coincidence search are included here. Even with the gross overestimate of rates, the combined coincidences of S1, e-burp, and water tank signal will happen an expected 3.8×10^{-6} times in the 272 live days of the LUX WIMP search - a negligible phenomena when considering false-positive through-going muon signals.

8.4.3 Pulse Overlap

An expansion of the primary cut timing window (described in Section 7.4) to 100 samples instead of 50 samples yielded no newly found through-going muons, indicating that requiring a start time difference of less than 50 samples is sufficient to capture well-behaved simultaneous water and Xenon PODs. The greater danger could occur when a muon passes through the xenon space during an elongated (greater than 100 sample) pulse, thus hiding the true start time of the muon in the Xe PMTs, causing the event to not be counted in the

primary timing cut. Considering the rate of pulses with $t_2 - t_0 > 100$ samples, and using very conservative overlap windows, the expected rate of overlap with long pulses is 1.8×10^{-8} s^{-1}. An expected 0.4 muon events will be lost due to overlap in 272 live-days.

8.4.4 PODs Cut Short

Activity occurring within a 1 ms window of an event trigger can be captured in a LUX data event. However, data acquisition can be cut short when a memory bank becomes filled. A memory bank will on average collect 1.2 seconds of data, or 1.2×10^8 samples. Under worse data taking conditions (such as high activity caused by noisy PMTs), a memory bank will usually collect .5 s of data. The act of being cut short doesn't affect identification of top-entry muons unless the cutoff occurs less than 500 samples before the pulse start. The cutoff rate is estimated at $r_{cutoff} = r_{coin} r_{disk} T_{window} = (8.13 \times 10^{-6}\ \text{s}^{-1})(2\ \text{s}^{-1})(500 \times 10^{-9}\ \text{s}) = 8.13 \times 10^{-12}\ \text{s}^{-1}$. Again, this will almost never occur in 272 days.

8.4.5 Stopping Muons

Stopping muons are muons with energies such that they stop completely in the detector (water or xenon), and subsequently decay into an electron and neutrinos. Muons that stop in the water before reaching the Xe volume will be missed. While this will not matter for calculating the muon flux at the particular surface chosen in this analysis (the xenon gas/liquid interface), stopping muons should be considered as an additional cause for neutrons that may have formed in the rock or water above. It is expected that less than $\sim 0.5\%$ of all muons will be stopping muons at this depth (Reference [85], see Figure 5.4).

8.4.6 Muons from Neutrino Interactions

Neutrino induced muons are created when cosmic ray neutrinos interact with surrounding rock via charge current interactions. Since neutrinos will penetrate the earth from all directions, not just from above, neutrino-induced muons will hit the detector isotropically from all directions. By contrast, cosmic ray muons follow the $\sec\theta\, e^{-X(\frac{\sec\theta - 1}{\Lambda})}$ zenith angle distribution, originating in the upper 2π hemisphere of the detector. Neutrino-induced muons could possibly be identified from their incidence angles, as they will be the only upward or sideways going muons.

This dissertation's main interest is in cosmic ray muons. In the LUX detector, an upward going neutrino-induced muon will be virtually indistinguishable from a downward-going cosmic ray muon and will be included in the flux calculation. However, neutrino-induced muons don't make significant contributions to overall muon flux at a depth of 4200 m.w.e. With an expected intensity of $2 \times 10^{-13}\text{cm}^{-2}\text{s}^{-1}\text{sr}^{-1}$, neutrino-induced muons make up less than 0.01% of the total muon flux. It is only at depths below 10000 m.w.e. that neutrino-induced muons contribute significantly to muon intensity, as exhibited by the intensity "floor" for depths below 10000 m.w.e. in Figure 5.2.

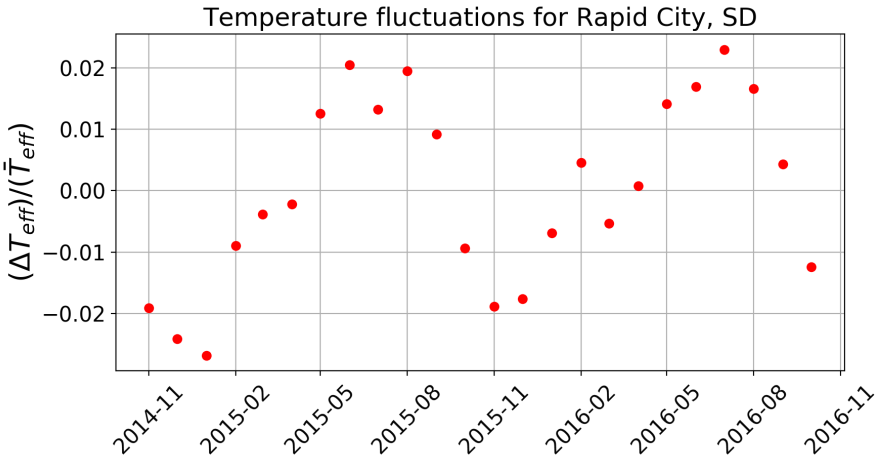

Figure 8.4: Rapid City temperature variation. ΔT_{eff} for each month is calculated from averaging temperatures over pressure levels ranging from 1000 to 10 hPa. Muon fluxes underground are expected to vary similarly, maximal in summer and minimal in winter.

8.4.7 Seasonal Variation of Muons

As stated in Section 5.2.6, the observed muon rate underground will vary with atmospheric temperature. A systematic over- or under-estimate of the muon rate relative to an annual average may result depending on when observations were made. Following the procedure laid out in Reference [95], the effective temperature by month is calculated here for SURF, with a sum over discrete levels X_i approximating the integral:

$$\begin{aligned} T_{eff} &= \frac{\int T(X)\, dX/X\, [\exp(-X/\Lambda_\pi) - \exp(-X/\Lambda_N)]}{\int dX/X\, [\exp(-X/\Lambda_\pi) - \exp(-X/\Lambda_N)]} \\ &\approx \frac{\sum_i T(X_i)/X_i\, [\exp(-X_i/\Lambda_\pi) - \exp(-X_i/\Lambda_N)]}{\sum_i (1/X_i)\, [\exp(-X_i/\Lambda_\pi) - \exp(-X_i/\Lambda_N)]} \end{aligned} \tag{8.6}$$

where $\Lambda_\pi = 160$ g cm^2 is the atmospheric attenuation length for pions and $\Lambda_N = 120$ g cm^2 is the atmospheric attenuation length for nucleons.

Temperature data is obtained from the Integrated Global Radiosonde Archive (IGRA). The closest IGRA station to SURF is in Rapid City, South Dakota, located 34 miles away, and temperature data was taken and averaged monthly at atmospheric pressure levels of 10,20,30,50,70,100,150,200,250,300,400,500,700,850, and 1000 (surface) hPa.

Due to the low monthly counts of top-entry muons in the detector, variations in muon rate can't be accurately judged. However, monthly temperature fluctuations from average can be weighted according to detector livetime to determine if any significant rate fluctuations should be considered. Temperature variations $\Delta T_{eff}/\bar{T_{eff}}$ are normalized to vary between -1 and +1. Monthly livetimes are taken as fractions of the livetime of the entire run. The product of temperature variation from the mean and fractional monthly livetime represents the amount the observed muon rate deviates from the average rate, with +1 corresponding

Effect	Fractional Error
Poisson counting (statistical)	$\pm 7.16\%$
Unknown angular distribution	$\pm < 1\%$
Stopping muons	$+0.5\%$
Seasonal variation	$+ < 0.5\%$
POD overlap	$+0.2\%$
Neutrino-induced muons	-0.01%
POD cutoff	$+0.0001\%$
Random coincidences: eburp	-0.000002%
Detector area	$\pm 0.42\%$

Table 8.2: Table of uncertainties. All rows except the last are associated with counting uncertainty for N_μ, last row refers to detector area.

to the maximal rate, and -1 the minimal rate. The rate was found to be weighted 5.3% of the full amplitude below the average rate.

While the expected fluctuations in rate for the 4850 level of Homestake are not fully known, they aren't expected to vary more than 5% from average (when accounting for seasonal variation). Taking a conservative upper limit of 10% variation, the weighted livetime considered here will lead to a counting underestimate of no more than 0.5%.

8.4.8 Angular Distribution of Muons

The largest counting uncertainty arises from the little that is known of the angular distribution of muons at Davis cavern. The efficiency of the 500 sample pulse timing cut is dependent on the angular distribution of the bombarding muons. This work mainly uses the Miyake distribution (see Equation 5.11), but the distribution has been demonstrated only up to zenith angles of 60°. The simulation from Section 7.3 was redone using a $\cos^{4.83}$ power law angular distribution that has also been suggested for this depth, and again using a constructed distribution that is identical to the Miyake distribution except it is made flat for $\theta > 60°$. Still, it was found that less than 1% of events are eliminated from the pulse timing cut using these flatter distributions.

8.5 Muon Flux

Most of the uncertainty in the calculated muon flux comes from the uncertainty in the number of counted muons. Since the water tank completely surrounds the xenon detector, angular acceptance is virtually 100%, and the high energy nature of cosmic ray muons allows them to be identified with near perfect efficiency within both the water tank and the xenon detector. However, because of the relatively small sample of $N_\mu = 195$, errors are dominated by counting statistics ($\sigma = \sqrt{N}$, for 7% counting error). This could be have been improved

Source	Total Muon Flux $[\times 10^{-9}\,\mu\ \mathrm{s}^{-1}\,\mathrm{cm}^{-2}]$
LUX 2017 (this work)	$4.60 \pm 0.33_{stat}$
Homestake 1983 [110] (see Section 8.6.1 for details)	4.14 ± 0.05
Majorana 2017 [111]	5.31 ± 0.17
Mei and Hime 2006 [85] (calculated from model)	4.4 ± 0.1
Gray et al 2011 [112] (extrapolated from measurements)	4.40

Table 8.3: Total muon flux measurements and predictions for 4850 level of Homestake Mine.

with a longer runtime. All of the uncertainties considered are summarized in Table 8.2.

The LUX detector and veto observed $195 \pm 14_{stat} \pm 2_{syst}$ muons through a 1798.44 ± 7.60 cm^2 surface over 2.35×10^7 live-seconds.

Finally, the muon flux is calculated to be:

$$\boxed{\frac{dN_\mu}{dA\,dt} = (4.60 \pm 0.33_{stat} \pm 0.060_{syst}) \times 10^{-9}\ \mu\,\mathrm{cm}^{-2}\,\mathrm{s}^{-1}}. \tag{8.7}$$

8.6 Comparison to Previous Works

This section compares the LUX muon flux measurement to previous measurements and predictions. Table 8.3 displays the relevant results.

8.6.1 Homestake, 1983

In Reference [110], Cherry *et al.* measured the muon flux at the 4850 level of Homestake over 18 months of data taking between 1979 and 1981. A central scintillator detector was surrounded by many rectangular water Cherenkov modules. The 36 side modules measured $2\text{m} \times 2\text{m} \times 1.2\text{m}$ and were stacked 3 high (6 m tall), 6 across (18 m wide) on two sides of the scintillator detector (see Figure 8.5). High-energy muons were identified by their triggering of multiple modules, and the analysis was restricted to nearly vertical muons by requiring that 3 vertically stacked modules be triggered, and no other modules triggered. This corresponds to zenith angles $\theta \lesssim 18°(= \arctan(1.0/3.0))$, using the width-to-height ratio of a vertical stack). After taking into account the geometric factors of the Cherenkov detectors, the single muon intensity was determined to be $(4.91 \pm 0.06) \times 10^{-9} \mu\ \mathrm{s}^{-1}\ \mathrm{cm}^{-2}\ \mathrm{sr}^{-1}$. Note that intensity includes an angular consideration (the sr^{-1} unit), as opposed to the flux (units of μ cm^{-2} s^{-1}) calculated from LUX data in Section 8.5.

The Homestake study measured muon multiplicity (see References [110] and [113]), and found $\sim 4.5\%$ of events were associated with multiple muons. Since the LUX detector did

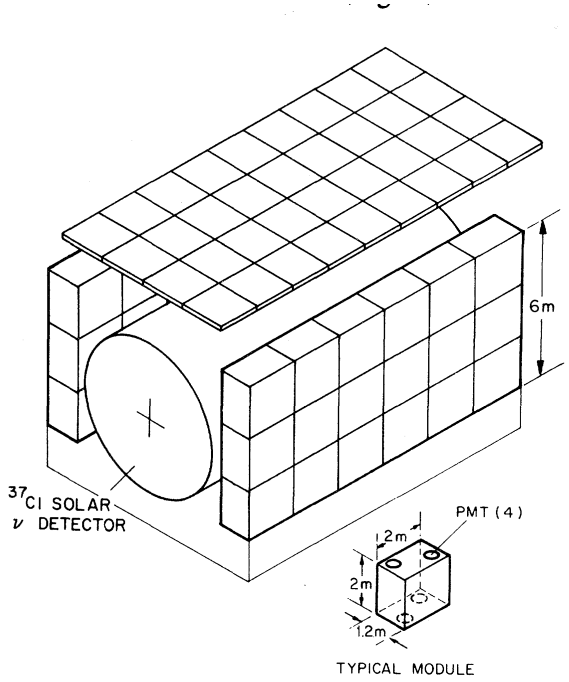

Figure 8.5: Diagram of the Homestake water Cherenkov detector. The two 6×3 stacks of side modules were used to count nearly vertical muons. Figure from [110].

not differentiate between single and multiple muon events, a more comparable measurement would be the total muon event flux, which includes single and multiple muon events, instead of just the single muons. With Homestake, 7214 vertical muon events were found (6814 of them single muons), corresponding to a muon flux of $(5.13 \pm 0.06) \times 10^{-9} \mu$ s^{-1} cm^{-2} sr^{-1}.

To compare the Homestake result with the measurement from LUX, both are converted to a vertical muon flux. The angular distribution of muons must be considered, and again the Miyake distribution described in Section 7.3 is utilized. Following a procedure similar to Reference [111], the LUX result is limited to an 18° cone to roughly correspond to the geometrical acceptance of the water Cherenkov stacks in Homestake, and 58.5% of the muon events remain. This can be seen as the fraction of the distribution in Figure 7.3 with $\theta < 18°$. The corresponding nearly vertical muon flux for LUX is $(2.70 \pm 0.19_{stat}) \times 10^{-9}\, \mu\, \mathrm{s}^{-1}\, \mathrm{cm}^{-2}$.

Flux J can be determined from intensity $I(\theta)$ via integration about the solid angle of interest:

$$J = \int I(\theta) \cos\theta d\Omega \tag{8.8}$$

Using the intensity-depth relation $I(h, \theta) = I(h, 0) \sec\theta\, e^{-\frac{h}{\Lambda}(\sec\theta - 1)}$, and taking $I(h, 0)$ to be the nearly vertical ($\theta = 0$) intensity measured at Homestake, the integral for flux (Equation 8.8) turns into

$$\begin{aligned} J &= ((5.13 \pm 0.06) \times 10^{-9}\, \mu\, \mathrm{s}^{-1}\, \mathrm{cm}^{-2}\, \mathrm{sr}^{-1}) \int_{\theta=0}^{18^\circ} \sec\theta\, e^{-\frac{h}{\Lambda}(\sec\theta - 1)} \cos\theta d\Omega \\ &= (1.42 \pm 0.02) \times 10^{-9}\, \mu\, \mathrm{s}^{-1}\, \mathrm{cm}^{-2} \end{aligned} \tag{8.9}$$

The discrepancy from the two results ($(2.71 \pm 0.19_{stat}) \times 10^{-9}\ \mu\ \mathrm{s}^{-1}\ \mathrm{cm}^{-2}$ for LUX, $(1.42 \pm 0.02) \times 10^{-9}\, \mu\, \mathrm{s}^{-1}\, \mathrm{cm}^{-2}$ for Homestake) is large and not even within several sigma of each other, but some of the gap may be explained by the many simplifying assumptions made to calculate the vertical fluxes. The calculation is dependent on the angular distribution of muons, and the Miyake model used may be too simple to describe muon angles. More detailed simulation may be appropriate. Azimuthal angles are assumed to be uniformly distributed around all 2π radians, but differences in the mountain surface and density profile may create preferred or suppressed angles for incoming muons. This makes the orientation of the Homestake modules important.

The largest overestimate in the above calculations may come from the integration of the LUX result over an 18° cone. The angular acceptance of rectangular modules does not translate readily to solid angle. Using the given geometric factor of $4.0\,\mathrm{m}^2\,\mathrm{sr}$, we can extract an average angular acceptance of 0.14 sr. A cone of apex angle 2θ subtends solid angle $\Omega = 2\pi(1 - \cos\theta)$, and for 0.14 sr, $\theta = 12.1^\circ$. Integrating the LUX result over the smaller cone results in 40.4% of the total count identified as vertical, and gives an vertical flux of $(1.86 \pm 0.13) \times 10^{-9}\, \mu\, \mathrm{s}^{-1}\, \mathrm{cm}^{-2}$. An angular acceptance of 9.5° is an upper bound for an area element at the bottom center of one of the stacked modules, and reduces the LUX total flux to 32.1%, or a vertical flux of $(1.48 \pm 0.11) \times 10^{-9}\ \mu\ \mathrm{s}^{-1}\ \mathrm{cm}^{-2}$. The pitfalls of using vertical flux is highlighted above, as the results are very sensitive to the models used to compare two detectors with wildly different geometries.

If instead the Homestake intensity is integrated over all angles ($0 < \theta < 90^\circ$), with the measured vertical intensity used as $I(h = 4200\,\mathrm{m.w.e.}, \theta = 0)$:

$$\begin{aligned} J &= ((5.13 \pm 0.06) \times 10^{-9}\, \mu\, \mathrm{s}^{-1}\, \mathrm{cm}^{-2}\, \mathrm{sr}^{-1}) \int_{\theta=0}^{90^\circ} \sec\theta\, e^{-\frac{h}{\Lambda}(\sec\theta - 1)} \cos\theta d\Omega \\ &= (4.14 \pm 0.05) \times 10^{-9}\, \mu\, \mathrm{s}^{-1}\, \mathrm{cm}^{-2} \end{aligned} \tag{8.10}$$

The result from Equation 8.10 gives total flux across all zenith angles, and is directly comparable to the LUX measurement. Again, the result will be dependent on which angular distribution is assumed. However, these results are reasonably comparable within two standard deviations: $(4.60 \pm 0.33_{stat}) \times 10^{-9}\, \mu\, \mathrm{s}^{-1}\, \mathrm{cm}^{-2}$ from LUX, $(4.14 \pm 0.05) \times 10^{-9}\, \mu\, \mathrm{s}^{-1}\, \mathrm{cm}^{-2}$ from Homestake. As noted in Reference [111], the uncertainties stated in Reference [110] appear to be purely statistical, with no discussion of systematics. The calculation for total flux still indicates moderate agreement between the two measurements.

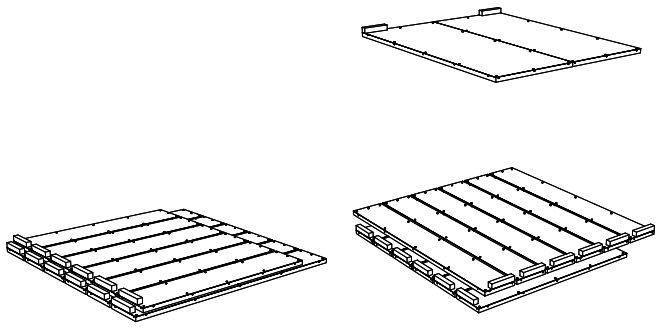

Figure 8.6: MJD veto panel configurations for muon study. Left: 2-fold coincidence, 12 veto panels. Right: 3-fold coincidence, 14 veto panels. Figure from [111].

8.6.2 Majorana Demonstrator, 2017

The Majorana Demonstrator (MJD) is developing high-purity germanium detectors, specifically to be used in search of neutrinoless double-beta decay ($\beta\beta(0\nu)$). MJD is also situated in the Davis Campus of SURF, just down the hallway from the LUX detector. The MJD muon veto system recently measured total muon flux at the 4850 level of SURF to be $(5.31 \pm 0.17) \times 10^{-9}\ \mu\,\mathrm{s}^{-1}\,\mathrm{cm}^{-2}$. (see Reference [111]).

The MJD muon veto system consists of various sizes and shapes of 2.54-cm-thick scintillating acrylic sheets. For 1536 hours of livetime in 2014, a configuration of 6 double-layered panels (12 panels total) observed 912 ± 43 muons, identified by simultaneous signals in two stacked panels. Each panel had an area of $5824\mathrm{cm}^2$. In the second configuration, a third layer of panels was added 1.6-m above the two stacked layers of 12 panels (see Figure 8.6). The 3-fold coincidence setup observed 615 ± 25 muons over 2678 hours of livetime in 2014, and the upper panels had a combined area of 35,450 cm^{-2}.

The result is somewhat higher than the LUX measurement. A natural guess may be that the MJD veto panel geometry is overestimating muon counts due to backgrounds, especially in the thinly stacked two-panel configuration. However, overlap between an exponential energy distribution representing background γ's and and a Landau distribution for muons appears to fit the data and be well-understood, and is not even expected to be a problem for the 3-panel configuration.

Another possible source of discrepancy may come from the spatial separation of the LUX vs. MJD detectors. While they both reside on the 4850-level of the same mine, the different locations may make the muon flux observed susceptible to different features of the rock profile directly above.

It is also noted that MJD data for the 2-panel configuration was taken during the annual modulation minimum (flux of $(5.09 \pm 0.24) \times 10^{-9}\ \mu\,\mathrm{s}^{-1}\,\mathrm{cm}^{-2}$), and 3-panel data during the maximum ($(5.54 \pm 0.23) \times 10^{-9}\ \mu\,\mathrm{s}^{-1}\,\mathrm{cm}^{-2}$), possibly pointing to a $\sim 5\%$ level annual variation. The combined result is taken as an average over seasonal variation.

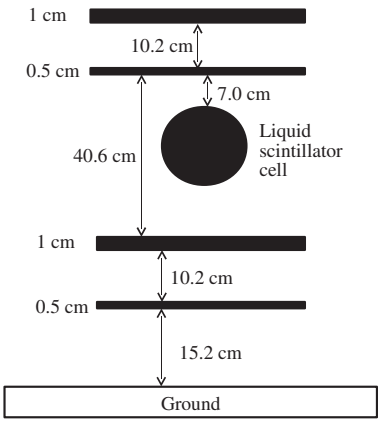

Figure 8.7: Muon detector setup deployed by Gray et al. Four square scintillator panels are spaced vertically. The liquid scintillator cell in the middle is used for underground neutron counting, and was not relevant to this study. Figure from [111].

8.6.3 Mei and Hime, 2006

In Reference [85], Mei and Hime derive a muon intensity function using observed muon fluxes measured at underground sites around the world. It is:

$$I_\mu(h_0) = 67.96 \times 10^{-6} e^{\frac{-h_0}{0.285}} + 2.071 \times 10^{-6} e^{\frac{-h_0}{0.698}}, \tag{8.11}$$

where h_0 is the site depth in km.w.e. and $I_\mu(h_0)$ is in units $\mathrm{cm}^{-2}\mathrm{s}^{-1}$. The total muon flux is calculated for the 4850 level of the Homestake mine at depth 4.3 ± 0.2 km.w.e. This predicts a total muon flux of $(4.4 \pm 0.1) \times 10^{-9}\ \mu\ \mathrm{cm}^{-2}\,\mathrm{s}^{-1}$. The LUX measurement is in agreement with the prediction.

8.6.4 Gray, 2011

In Reference [112], muon flux measurements were taken at three different depths of the Homestake Mine: surface ($\sim$ .001 km.w.e.), 800-ft (0.712 km.w.e.), and 2000-ft below (1.78 km.w.e.). At each depth, a setup of four square plastic scintillation panels, 30.5 cm $\times$ 30.5 cm each (see Figure 8.7), counted muons via 3-fold coincidence between the panels. After using Monte Carlo to calculate the solid angle acceptance of the configuration, and using 4-fold coincidence data as a cross-check, the flux per unit solid angle is found to be $(1.149 \pm 0.017) \times 10^{-2}, (2.67 \pm 0.06) \times 10^{-6}$, and $(2.56 \pm 0.25) \times 10^{-7}\ \mu\ \mathrm{s}^{-1}\,\mathrm{cm}^{-2}\,\mathrm{sr}^{-1}$ for the depths of 0.001, 0.712, and 1.78 km.w.e., respectively.

The modeling techniques used in Reference [85] were used and calibrated by the new results by Gray et al. The new model for the 4850 level of Homestake results in a predicted integral flux of $4.40 \times 10^{-7}\,\mu\,\mathrm{s}^{-1}\,\mathrm{cm}^{-2}\,\mathrm{sr}^{-1}$, a result nearly identical to the previous prediction from Reference [85]. The agreement with the LUX measurement is again within a standard deviation.

8.7 Conclusions

The muon flux of $(4.60 \pm 0.33_{stat} \pm 0.060_{syst}) \times 10^{-9} \mu\text{cm}^{-2}\text{s}^{-1}$ measured by the LUX xenon detector and water tank is in good agreement with previous measurements and predictions for the 4850 level of Homestake Mine. The current understanding of muon transport through the rock overhead prevails, and the expected number of muon-induced neutrons reaching the fiducial xenon region in the full LUX exposure is less than 1 (see Section 6.1 and Reference [102]).

Using the combination of LUX xenon and water tanks offers a unique geometry for identifying cosmic ray muons. Previous works utilized stacked detectors, which limited the angular acceptance of the detectors and relegated the studies to nearly vertical muons. Since the water tank completely surrounds the xenon detector, full angular acceptance is essentially achieved. While this work considered muons crossing the fiducial surface formed by the xenon gas-liquid interface (or "top-entry muons"), pulse shapes for other muons that clip through the xenon detector ("side-entry muons") can be identified and analyzed. A longer exposure of the LUX xenon-water system could inform a study of muons at steep angles to vertical – a distribution that is not as well known as nearly-vertical muons.

Chapter 9

LUX Results and Beyond

The LUX detector was specifically tuned for the search of WIMP dark matter, yet in its short but sweet lifetime, it could not definitively claim to have seen dark matter. But it's not fair to state that it "saw nothing," as the world's most sensitive dark matter detector at the time, it proved skilled at detecting all kinds of radiation, as well as revealing/excluding a lot of new physics.

9.1 LUX WIMP Search Results

LUX has calculated limits on spin-independent WIMP-nucleon interactions based on its first 95 live-day science run (Reference [114]), its second 332 live-day run (Reference [115]), and the combined exposure (Reference [116]). At the times of their publications, the limits boasted being the most sensitive in the world, but that title has recently changed hands and now belongs to Xenon1T (Reference [117]) for WIMP masses above 20 GeV. Xenon1T uses similar technology to LUX, and is the first tonne-scale detector of its kind.

The standard for calculating exclusion limits in the dark matter community has been the Yellin optimal exclusion method (Reference [118]). However LUX utilizes the profile likelihood ratio (PLR, Reference [119]). WIMP signal and background-only models were built as hypotheses to test against the observed LUX data (see Figure 9.1). A likelihood function is constructed for both models over a range of possible WIMP-nucleon cross sections σ, and for a range of WIMP masses. The PLR statistic indicates that the LUX data is consistent with the background-only model with a p-value of .39 for 100 GeV WIMP mass.

The limit curves calculated by LUX and several other experiments are displayed in Figure 9.2. These curves all exhibit the same general shape. The steep ascent at lower WIMP masses come from detector limitations in energy threshold and resolution. The shallower ascent toward higher WIMP masses comes from the mass difference between target and WIMP, and the decreasing number density of WIMPs (since the energy density of WIMPs is taken as a constant, the number density must decrease as mass increases).

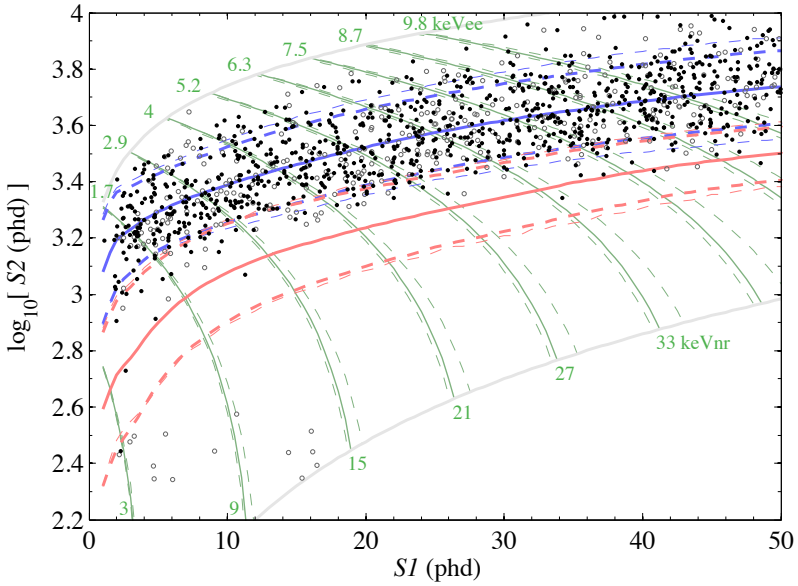

Figure 9.1: Run04 WIMP search data passing all data quality cuts. Appropriate S1-S2 events occurring within the detector fiducial volume are shown, and ER (blue) and NR (red) bands are shown with their mean (solid) and 10% and 90 % contours (dashed), with model variations indicated in fainter contours. Figure from Reference [116].

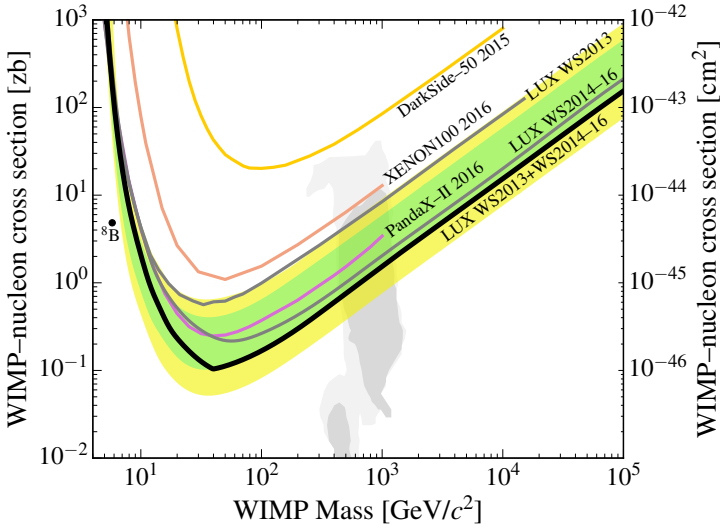

Figure 9.2: WIMP limit plot including LUX's full exposure. Figure from Reference [116].

9.2 The Future

The LUX detector has been decommissioned, and after being brought back to the surface is on display at the Sanford Lab Homestake Visitor Center. With WIMP limits published, the LUX science data is now being analyzed to search for more (and less) exotic physics: other dark matter candidates, effective field theories to explain WIMP coupling, detector physics to better understand xenon scintillation, and much more. Looking forward, the LUX-ZEPLIN (LZ) experiment is currently being planned to take the place of LUX on the 4850 level of Homestake. LZ is the tonne-scale continuation of the LUX and ZEPLIN xenon detectors, and will continue to push limits and press on in the search for dark matter.

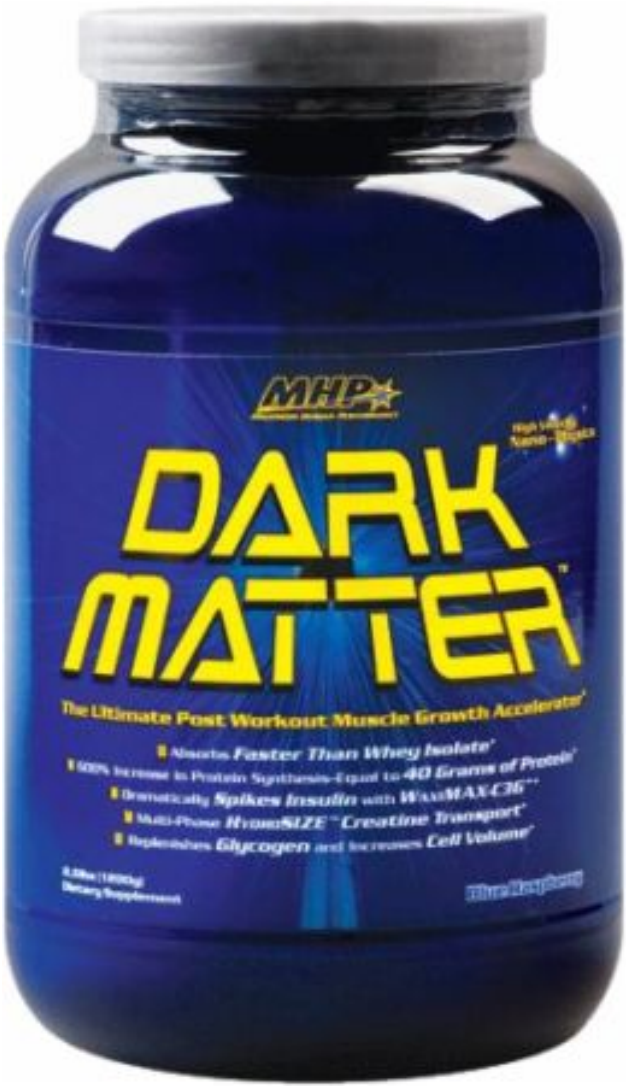

Figure 9.3: A final figure: dark matter.

Bibliography

[1] Edward W. Kolb and Michael Stanley Turner. *The early universe*. Number v. 69 in Frontiers in physics. Addison-Wesley, Reading, Mass, 1990.

[2] Barbara Sue Ryden. *Introduction to cosmology*. Addison-Wesley, San Francisco, 2003.

[3] R. Amanullah, et al. SPECTRA AND *HUBBLE SPACE TELESCOPE* LIGHT CURVES OF SIX TYPE Ia SUPERNOVAE AT $0.511 < z < 1.12$ AND THE UNION2 COMPILATION. *The Astrophysical Journal*, 716(1):712–738, June 2010.

[4] F. Zwicky. On the Masses of Nebulae and of Clusters of Nebulae. *The Astrophysical Journal*, 86:217, October 1937.

[5] F. Zwicky. Die Rotverschiebung von extragalaktischen Nebeln. *Helvetica Physica Acta*, 6:110–127, 1933.

[6] J. H. Oort. The force exerted by the stellar system in the direction perpendicular to the galactic plane and some related problems. *Bulletin of the Astronomical Institutes of the Netherlands*, 6:249, August 1932.

[7] V. C. Rubin, N. Thonnard, and W. K. Ford, Jr. Rotational properties of 21 SC galaxies with a large range of luminosities and radii, from NGC 4605 /R = 4kpc/ to UGC 2885 /R = 122 kpc/. *The Astrophysical Journal*, 238:471, June 1980.

[8] C. Alcock, et al. The MACHO Project: Microlensing Results from 5.7 Years of Large Magellanic Cloud Observations. *The Astrophysical Journal*, 542(1):281–307, October 2000.

[9] Craig J. Copi, David N. Schramm, and Michael S. Turner. Big-Bang Nucleosynthesis and the Baryon Density of the Universe. *Science*, 267(5195):192–199, January 1995. arXiv: astro-ph/9407006.

[10] Ryan Cooke, Max Pettini, Regina A. Jorgenson, Michael T. Murphy, and Charles C. Steidel. Precision measures of the primordial abundance of deuterium. *The Astrophysical Journal*, 781(1):31, January 2014. arXiv: 1308.3240.

[11] N. Jarosik, et al. SEVEN-YEAR *WILKINSON MICROWAVE ANISOTROPY PROBE* (*WMAP*) OBSERVATIONS: SKY MAPS, SYSTEMATIC ERRORS, AND BASIC RESULTS. *The Astrophysical Journal Supplement Series*, 192(2):14, February 2011.

[12] S. D. M. White, M. Davis, and C. S. Frenk. The size of clusters in a neutrino-dominated universe. *Monthly Notices of the Royal Astronomical Society*, 209(1):27P–31P, July 1984.

[13] M. Milgrom. A modification of the Newtonian dynamics as a possible alternative to the hidden mass hypothesis. *The Astrophysical Journal*, 270:365, July 1983.

[14] Douglas Clowe, et al. A Direct Empirical Proof of the Existence of Dark Matter. *The Astrophysical Journal*, 648(2):L109–L113, September 2006.

[15] K.A. Olive. Review of Particle Physics. *Chinese Physics C*, 38(9):090001, August 2014.

[16] Planck Collaboration, et al. Planck 2015 results. XIII. Cosmological parameters. *Astronomy & Astrophysics*, 594:A13, October 2016. arXiv: 1502.01589.

[17] S. Chatrchyan, et al. Observation of a new boson at a mass of 125 GeV with the CMS experiment at the LHC. *Physics Letters B*, 716(1):30–61, September 2012.

[18] G. Aad, et al. Observation of a new particle in the search for the Standard Model Higgs boson with the ATLAS detector at the LHC. *Physics Letters B*, 716(1):1–29, September 2012.

[19] Stephen P. Martin. A SUPERSYMMETRY PRIMER. In *Advanced Series on Directions in High Energy Physics*, volume 18, pages 1–98. WORLD SCIENTIFIC, July 1998. DOI: 10.1142/9789812839657_0001.

[20] Gerard Jungman, Marc Kamionkowski, and Kim Griest. Supersymmetric dark matter. *Physics Reports*, 267(5-6):195–373, March 1996.

[21] John Preskill, Mark B. Wise, and Frank Wilczek. Cosmology of the invisible axion. *Physics Letters B*, 120(1-3):127–132, January 1983.

[22] J. Ipser and P. Sikivie. Can Galactic Halos Be Made of Axions? *Physical Review Letters*, 50(12):925–927, March 1983.

[23] Gray Rybka. Direct detection searches for axion dark matter. *Physics of the Dark Universe*, 4:14–16, September 2014.

[24] R. D. Peccei and Helen R. Quinn. Constraints imposed by $\mathrmCP$ conservation in the presence of pseudoparticles. *Phys. Rev. D*, 16(6):1791–1797, September 1977.

[25] S. J. Asztalos, et al. SQUID-Based Microwave Cavity Search for Dark-Matter Axions. *Physical Review Letters*, 104(4), January 2010.

[26] Scott Dodelson and Lawrence M. Widrow. Sterile neutrinos as dark matter. *Physical Review Letters*, 72(1):17–20, January 1994.

[27] Kenny C.Y. Ng, Shunsaku Horiuchi, Jennifer M. Gaskins, Miles Smith, and Robert Preece. Improved limits on sterile neutrino dark matter using full-sky Fermi Gamma-ray Burst Monitor data. *Physical Review D*, 92(4), August 2015.

[28] O. Adriani, et al. An anomalous positron abundance in cosmic rays with energies 1.5100 GeV. *Nature*, 458(7238):607–609, April 2009.

[29] M. Aguilar, et al. First Result from the Alpha Magnetic Spectrometer on the International Space Station: Precision Measurement of the Positron Fraction in Primary Cosmic Rays of 0.5350 GeV. *Physical Review Letters*, 110(14), April 2013.

[30] Julio F. Navarro, Carlos S. Frenk, and Simon D. M. White. The Structure of Cold Dark Matter Halos. *The Astrophysical Journal*, 462:563, May 1996.

[31] J.D. Lewin and P.F. Smith. Review of mathematics, numerical factors, and corrections for dark matter experiments based on elastic nuclear recoil. *Astroparticle Physics*, 6(1):87–112, December 1996.

[32] V Chepel and H Arajo. Liquid noble gas detectors for low energy particle physics. *Journal of Instrumentation*, 8(04):R04001–R04001, April 2013.

[33] Richard H. Helm. Inelastic and Elastic Scattering of 187-Mev Electrons from Selected Even-Even Nuclei. *Physical Review*, 104(5):1466–1475, December 1956.

[34] G.J. Alner, et al. First limits on nuclear recoil events from the ZEPLIN I galactic dark matter detector. *Astroparticle Physics*, 23(5):444–462, June 2005.

[35] C. E. Aalseth, et al. Results from a Search for Light-Mass Dark Matter with a p -Type Point Contact Germanium Detector. *Physical Review Letters*, 106(13), March 2011.

[36] G. Angloher, et al. Results from 730 kg days of the CRESST-II Dark Matter search. *The European Physical Journal C*, 72(4), April 2012.

[37] E. Behnke, et al. First dark matter search results from a 4-kg CF 3 I bubble chamber operated in a deep underground site. *Physical Review D*, 86(5), September 2012.

[38] Berta Beltran and the Picasso collaboration. Dark matter spin-dependent limits for WIMP interactions on ^{19} F by PICASSO. *Journal of Physics: Conference Series*, 203:012032, January 2010.

[39] G.J. Alner, et al. First limits on WIMP nuclear recoil signals in ZEPLIN-II: A two-phase xenon detector for dark matter detection. *Astroparticle Physics*, 28(3):287–302, November 2007.

[40] E. Aprile, et al. Dark Matter Results from 225 Live Days of XENON100 Data. *Physical Review Letters*, 109(18), November 2012.

[41] R. Agnese, et al. Search for Low-Mass Weakly Interacting Massive Particles with SuperCDMS. *Physical Review Letters*, 112(24), June 2014.

[42] E. Armengaud, et al. Final results of the EDELWEISS-II WIMP search using a 4-kg array of cryogenic germanium detectors with interleaved electrodes. *Physics Letters B*, 702(5):329–335, August 2011.

[43] R. Bernabei, et al. New results from DAMA/LIBRA. *The European Physical Journal C*, 67(1-2):39–49, May 2010.

[44] E. Aprile, et al. First Dark Matter Results from the XENON100 Experiment. *Physical Review Letters*, 105(13), September 2010.

[45] J. I. Collar and D.N. McKinsey. [arXiv:1005.0838 [astro-ph.CO]] Comments on "First Dark Matter Results from the XENON100 Experiment", May 2010.

[46] XENON100 Collaboration. [arXiv:1005.2615 [astro-ph.CO]] Reply to the Comments on the XENON100 First Dark Matter Results, May 2010.

[47] J. I. Collar and D.N. McKinsey. [arXiv:1005.3723 [astro-ph.CO]] Response to arXiv:1005.2615, May 2010.

[48] Christopher Savage, Graciela Gelmini, Paolo Gondolo, and Katherine Freese. XENON10/100 dark matter constraints in comparison with CoGeNT and DAMA: Examining the L eff dependence. *Physical Review D*, 83(5), March 2011.

[49] Juan Collar. [arXiv:1006.2031 [astro-ph.CO]] Comments on arXiv:1006.0972 "XENON10/100 dark matter constraints in comparison with CoGeNT and DAMA: examining the Leff dependence", June 2010.

[50] C. E. Aalseth, et al. Search for an Annual Modulation in a p -Type Point Contact Germanium Dark Matter Detector. *Physical Review Letters*, 107(14), September 2011.

[51] E. Barbosa de Souza, et al. First search for a dark matter annual modulation signal with NaI(Tl) in the Southern Hemisphere by DM-Ice17. *Physical Review D*, 95(3), February 2017.

[52] Glenn F. Knoll. *Radiation detection and measurement*. Wiley, New York, 3rd ed edition, 2000.

[53] J.B. Birks. *The Theory and Practice of Scintillation Counting*. International series of monographs on electronics and instrumentation. Macmillan, 1964.

[54] Elena Aprile, editor. *Noble gas detectors*. Wiley-VCH, Weinheim, 2006. OCLC: ocm74965766.

[55] D.S. Akerib, et al. The Large Underground Xenon (LUX) experiment. *Nuclear Instruments and Methods in Physics Research Section A: Accelerators, Spectrometers, Detectors and Associated Equipment*, 704:111–126, March 2013.

[56] Raymond Davis. Solar Neutrinos. II. Experimental. *Physical Review Letters*, 12(11):303–305, March 1964.

[57] Jaret Heise. The Sanford Underground Research Facility at Homestake. *Journal of Physics: Conference Series*, 606:012015, May 2015. arXiv: 1503.01112.

[58] D. R. Nygren. The Time Projection Chamber: A New 4 pi Detector for Charged Particles. *eConf*, C740805:58, 1974.

[59] Adam Wade Bradley. *LUX THERMOSYPHON CRYOGENICS AND RADON-RELATED BACKGROUNDS FOR THE FIRST WIMP RESULT*. PhD thesis, Case Western Reserve University, 2014.

[60] A. Dobi, et al. Xenon purity analysis for EXO-200 via mass spectrometry. *Nuclear Instruments and Methods in Physics Research Section A: Accelerators, Spectrometers, Detectors and Associated Equipment*, 675:40–46, May 2012.

[61] E. M. Gushchin, et al. Electron emission from condensed noble gases. *Soviet Journal of Experimental and Theoretical Physics*, 49:856, May 1979.

[62] E. M. Gushchin, A. A. Kruglov, and I. M. Obodovski. Emission of "hot" electrons from liquid and solid argon and xenon. *Soviet Journal of Experimental and Theoretical Physics*, 55(5):860, May 1982.

[63] Rachel Mannino. *MEASURING BACKGROUNDS FROM 85KR AND 210BI TO IMPROVE SENSITIVITY OF DARK MATTER DETECTORS*. PhD thesis, Texas A&M University, 2017.

[64] D.S. Akerib, et al. An ultra-low background PMT for liquid xenon detectors. *Nuclear Instruments and Methods in Physics Research Section A: Accelerators, Spectrometers, Detectors and Associated Equipment*, 703:1–6, March 2013.

[65] Carlos H. Faham. *Prototype, Surface Commissioning and Photomultiplier Tube Characterization for the Large Underground Xenon (LUX) Direct Dark Matter Search Experiment*. PhD thesis, Brown University, May 2014.

[66] LUX Collaboration, et al. Chromatographic separation of radioactive noble gases from xenon. *ArXiv e-prints: arXiv:1605.03844 [physics.ins-det]*, May 2016.

[67] D.S. Akerib, et al. Radiogenic and muon-induced backgrounds in the LUX dark matter detector. *Astroparticle Physics*, 62:33–46, March 2015.

[68] David Malling. *Measurement and Analysis of WIMP Detection Backgrounds, and Characterization and Performance of the Large Underground Xenon Dark Matter Search Experiment*. PhD thesis, Brown University, May 2014.

[69] D.S. Akerib, et al. Signal yields, energy resolution, and recombination fluctuations in liquid xenon. *Physical Review D*, 95(1), January 2017.

[70] D.S. Akerib, et al. Tritium calibration of the LUX dark matter experiment. *Physical Review D*, 93(7), April 2016.

[71] L. W. Kastens, S. B. Cahn, A. Manzur, and D. N. McKinsey. Calibration of a liquid xenon detector with Kr 83 m. *Physical Review C*, 80(4), October 2009.

[72] LUX Collaboration, et al. Low-energy (0.7-74 keV) nuclear recoil calibration of the LUX dark matter experiment using D-D neutron scattering kinematics. *arXiv:1608.05381 [astro-ph, physics:hep-ex, physics:physics]*, August 2016. arXiv: 1608.05381.

[73] D.S. Akerib, et al. Data acquisition and readout system for the LUX dark matter experiment. *Nuclear Instruments and Methods in Physics Research Section A: Accelerators, Spectrometers, Detectors and Associated Equipment*, 668:1–8, March 2012.

[74] D.S. Akerib, et al. FPGA-based trigger system for the LUX dark matter experiment. *Nuclear Instruments and Methods in Physics Research Section A: Accelerators, Spectrometers, Detectors and Associated Equipment*, 818:57–67, May 2016.

[75] V. F. Hess. ber Beobachtungen der durchdringenden Strahlung bei sieben Freiballonfahrten. *Physikalische Zeitschrift*, 13:1084–1091, November 1912.

[76] Todor Stanev. *High energy cosmic rays*. Springer-Praxis books in astronomy and planetary sciences. Springer ; Praxis, Berlin ; New York : Chichester, UK, 2nd ed edition, 2009.

[77] P. K. F. Grieder. *Cosmic rays at Earth: researcher's reference manual and data book*. Elsevier Science Ltd, Amsterdam ; New York, 1st ed edition, 2001.

[78] Thomas K. Gaisser. *Cosmic rays and particle physics*. Cambridge University Press, Cambridge [England] ; New York, 1990.

[79] M. Crouch. An Improved World Survey Expression for Cosmic Ray Vertical Intensity VS. Depth in Standard Rock. *International Cosmic Ray Conference*, 6:165, 1987.

[80] Yu M Andreev, VI Gurentzov, and IM Kogai. Proc. 20th Int. Cosmic Ray Conf. *Moscow*, 6:200, 1987.

[81] M Aglietta, et al. Neutrino-induced and atmospheric single-muon fluxes measured over five decades of intensity by LVD at Gran Sasso Laboratory. *Astroparticle Physics*, 3(4):311–320, 1995.

[82] M Ambrosio, et al. Vertical muon intensity measured with MACRO at the Gran Sasso laboratory. *Physical Review D*, 52(7):3793, 1995.

[83] Ch Berger, et al. Experimental study of muon bundles observed in the Fr\'ejus detector. *Physical Review D*, 40(7):2163, 1989.

[84] Saburo Miyake. Empirical Formula for Range Spectrum of Cosmic Ray μ Mesons at Sea Level. *Journal of the Physical Society of Japan*, 18(7):1093–1093, July 1963.

[85] D.-M. Mei and A. Hime. Muon-induced background study for underground laboratories. *Physical Review D*, 73(5), March 2006.

[86] S Miyake. Rapporteur Paper On Muons And Neutrinos. In *Proceedings of the 13th International Cosmic Ray Conference*, volume 5, pages 3638–3655, Denver, CO, August 1973.

[87] E. J. Fenyves, et al. Angular distribution of cosmic ray muons at 4200 m.w.e. *International Cosmic Ray Conference*, 10:317–320, 1981.

[88] M. Ambrosio, et al. High energy cosmic ray physics with underground muons in MACRO. II. Primary spectra and composition. *Physical Review D*, 56(3):1418–1436, August 1997.

[89] P. N. Bhat and P. V. Ramana Murthy. Intensity measurements of low energy cosmic ray muons underground. *Journal of Physics A: Mathematical, Nuclear and General*, 6(12):1960, 1973.

[90] G. L. Cassiday, J. W. Keuffel, and J. A. Thompson. Calculation of the Stopping-Muon Rate Underground. *Phys. Rev. D*, 7(7):2022–2031, April 1973.

[91] B. Baschiera, L. Bergamasco, C. Castagnoli, and P. Picchi. Experimental results on muons stopping underground ((60-4500) m w.e.). *Lettere al Nuovo Cimento (1969-1970)*, 4(4):121–123, July 1970.

[92] B. Baschiera, L. Bergamasco, C. Castagnoli, and P. Picchi. Further results on muons stopping at great depth. *Lettere al Nuovo Cimento*, 1(23):961–966, June 1971.

[93] R. R. S. de Mendona, et al. THE TEMPERATURE EFFECT IN SECONDARY COSMIC RAYS (MUONS) OBSERVED AT THE GROUND: ANALYSIS OF THE GLOBAL MUON DETECTOR NETWORK DATA. *The Astrophysical Journal*, 830(2):88, October 2016.

[94] P. Adamson, et al. Observation of muon intensity variations by season with the MINOS far detector. *Physical Review D*, 81(1), January 2010.

[95] M. Ambrosio, et al. Seasonal variations in the underground muon intensity as seen by MACRO. *Astroparticle Physics*, 7(1-2):109–124, June 1997.

[96] Joseph A. Formaggio and C.J. Martoff. BACKGROUNDS TO SENSITIVE EXPERIMENTS UNDERGROUND. *Annual Review of Nuclear and Particle Science*, 54(1):361–412, December 2004.

[97] Y.-F. Wang, et al. Predicting neutron production from cosmic-ray muons. *Physical Review D*, 64(1), June 2001.

[98] S. Agostinelli, et al. Geant4a simulation toolkit. *Nuclear Instruments and Methods in Physics Research Section A: Accelerators, Spectrometers, Detectors and Associated Equipment*, 506(3):250–303, July 2003.

[99] A. Fasso', et al. The physics models of FLUKA: status and recent development. *ArXiv High Energy Physics - Phenomenology e-prints: arXiv:hep-ph/0306267*, June 2003.

[100] P. Antonioli, C. Ghetti, E.V. Korolkova, V.A. Kudryavtsev, and G. Sartorelli. A three-dimensional code for muon propagation through the rock: MUSIC. *Astroparticle Physics*, 7(4):357–368, October 1997.

[101] V. A. Kudryavtsev. Muon simulation codes MUSIC and MUSUN for underground physics. *Computer Physics Communications*, 180(3):339–346, March 2009. arXiv: 0810.4635.

[102] Luiz de Viveiros. *Optimization of Signal versus Background in Liquid Xe Detectors Used for Dark Matter Direct Detection Experiments.* PhD thesis, Brown University, 2010.

[103] PA Cerenkov. Visible luminescence of pure liquids under action of -radiation. In *Doklady Akad. Nauk (USSR)*, volume 2, page 451, 1934.

[104] IETIM Frank and Ig Tamm. Coherent visible radiation from fast electrons passing through matter. *CR Acad. Sci. USSR*, 14:109–114, 1937.

[105] E Fenyves and O Haiman. *The Physical Principles of Nuclear Radiation Measurements.* Academic Press, 1969.

[106] Michael F. L'Annunziata, editor. *Handbook of radioactivity analysis*. Elsevier, AP, Amsterdam, third edition edition, 2012.

[107] E. Aprile and T. Doke. Liquid xenon detectors for particle physics and astrophysics. *Reviews of Modern Physics*, 82(3):2053–2097, July 2010.

[108] Rachel Mannino and Patrick Phelps. LUX Height and Inner Radius Calculations, Internal LUX collaboration document, November 2013.

[109] T.A. Shutt. LUX Internal Installation Drawings.

[110] M. L. Cherry, et al. Multiple muons in the Homestake underground detector. *Physical Review D*, 27(7):1444–1447, April 1983.

[111] N. Abgrall, et al. Muon flux measurements at the davis campus of the sanford underground research facility with the majorana demonstrator veto system. *Astroparticle Physics*, 93:70–75, July 2017.

[112] F.E. Gray, et al. Cosmic ray muon flux at the Sanford Underground Laboratory at Homestake. *Nuclear Instruments and Methods in Physics Research Section A: Accelerators, Spectrometers, Detectors and Associated Equipment*, 638(1):63–66, May 2011.

[113] J. W. Elbert, T. K. Gaisser, and Todor Stanev. Analysis of deep-underground muons. *Physical Review D*, 27(7):1448–1456, April 1983.

[114] D.S. Akerib, et al. First Results from the LUX Dark Matter Experiment at the Sanford Underground Research Facility. *Physical Review Letters*, 112(9), March 2014.

[115] LUX Collaboration, et al. Improved Limits on Scattering of Weakly Interacting Massive Particles from Reanalysis of 2013 LUX Data. *Physical Review Letters*, 116(16):161301, April 2016.

[116] D.S. Akerib, et al. Results from a Search for Dark Matter in the Complete LUX Exposure. *Physical Review Letters*, 118(2), January 2017.

[117] E. Aprile, et al. First Dark Matter Search Results from the XENON1t Experiment. *ArXiv e-prints: arXiv:1705.06655 [astro-ph.CO]*, May 2017.

[118] S. Yellin. Finding an upper limit in the presence of an unknown background. *Physical Review D*, 66(3), August 2002.

[119] Glen Cowan, Kyle Cranmer, Eilam Gross, and Ofer Vitells. Asymptotic formulae for likelihood-based tests of new physics. *The European Physical Journal C*, 71(2):1–19, February 2011.

Appendix A

Table of Throughgoing Muons

For reference or future study/validation, this Appendix lists the luxstamps and dataset prefixes for the events considered throughgoing muons in this thesis.

Table A.1: Luxstamps and dataset prefixes for throughgoing muons.

luxstamp	dataset_prefix
12418035490547227	lux10_20141208T0307
12431682506602633	lux10_20141209T1735
12470261851016804	lux10_20141214T0601
12488597407629821	lux10_20141216T0901
12503822153221985	lux10_20141218T0322
12526586926688912	lux10_20141220T1654
12527279192250708	lux10_20141220T2039
12532395337594780	lux10_20141221T1036
12546509790608722	lux10_20141223T0215
12686464509643163	lux10_20150108T0608
12716096420448930	lux10_20150111T1627
12741658409592193	lux10_20150114T1624
12780347929223621	lux10_20150119T0436
12781021301338322	lux10_20150119T0436
12839485944482879	lux10_20150126T0035
12902955715302094	lux10_20150202T0549
12990556794249777	lux10_20150212T1157
13001902546755286	lux10_20150213T1724
13009989638054145	lux10_20150214T1851
13016253323674335	lux10_20150215T0955
13017421848717537	lux10_20150215T1359

Table A.1: Luxstamps and dataset prefixes for throughgoing muons.

luxstamp	dataset_prefix
13025753915971353	lux10_20150216T1424
13026044822866750	lux10_20150216T1424
13070846963115653	lux10_20150221T1556
13071373174606653	lux10_20150221T1556
13160590920351936	lux10_20150303T2216
13170633980403775	lux10_20150305T0441
13173776039861686	lux10_20150305T1214
13176772933115602	lux10_20150305T1946
13187140424673924	lux10_20150307T0504
13201525584666231	lux10_20150308T1854
13207747967666590	lux10_20150309T1044
13233238175245614	lux10_20150312T1131
13234064345150364	lux10_20150312T1131
13952267901883381	lux10_20150603T1933
13994192350539156	lux10_20150608T1059
13994201588061938	lux10_20150608T1059
13998585820171576	lux10_20150609T0327
14012913285817290	lux10_20150610T1851
14015645383611566	lux10_20150611T0304
14017473371442029	lux10_20150611T0304
14055142514510364	lux10_20150615T1605
14060700344893657	lux10_20150616T0823
14088570410172961	lux10_20150619T0854
14100226586766440	lux10_20150620T1710
14102679608395228	lux10_20150621T0151
14107230419187119	lux10_20150621T1800
14125481531144134	lux10_20150623T1527
14127642146111408	lux10_20150623T2328
14147246744551184	lux10_20150626T0949
14177145407498934	lux10_20150629T2034
14244385180294458	lux10_20150707T1423
14331014681248852	lux10_20150717T1514
14366440577662730	lux10_20150721T1118
14384094351188258	lux10_20150723T1726

Table A.1: Luxstamps and dataset prefixes for throughgoing muons.

luxstamp	dataset_prefix
14404974792653033	lux10_20150726T0151
14455237960286988	lux10_20150801T0046
14457682830432567	lux10_20150801T0046
14512434039783266	lux10_20150807T1601
14515332233187867	lux10_20150808T0002
14517641081734282	lux10_20150808T0002
14528867452598470	lux10_20150809T0950
14536460524577476	lux10_20150810T0929
14552636429684080	lux10_20150812T0759
14589108248011474	lux10_20150816T0943
14600149085014434	lux10_20150817T1721
14633640594137423	lux10_20150821T1616
14662414795117544	lux10_20150824T1755
14664741213319345	lux10_20150825T0153
14666755260853719	lux10_20150825T0941
14670912240479805	lux10_20150825T1724
14687072728618926	lux10_20150827T1837
14692733839749305	lux10_20150828T1024
14719157860728597	lux10_20150831T0936
14750453083141548	lux10_20150904T0152
14764624606428468	lux10_20150905T1716
14790905313352353	lux10_20150908T1840
14791728201398304	lux10_20150908T1840
14806898826979641	lux10_20150910T1234
14826972219282957	lux10_20150913T0151
14841610295639869	lux10_20150914T1824
14843799130581172	lux10_20150914T1824
14846394978171928	lux10_20150915T0235
14851840586177039	lux10_20150915T2003
14901894762449440	lux10_20150921T1753
14910115254352388	lux10_20150922T1009
14924689202109697	lux10_20150924T0747
14937030755140654	lux10_20150925T1615
14937462184320101	lux10_20150925T1615

Table A.1: Luxstamps and dataset prefixes for throughgoing muons.

luxstamp	dataset_prefix
14948790973393415	lux10_20150927T0151
15105575004246337	lux10_20151015T0310
15106393327664148	lux10_20151015T0310
15120064027413222	lux10_20151016T2210
15141822428593794	lux10_20151019T1037
15148381507964299	lux10_20151019T2332
15180623811313419	lux10_20151023T1859
15191992120792222	lux10_20151025T0151
15200688186451437	lux10_20151026T0143
15203260259239065	lux10_20151026T0940
15224031459995004	lux10_20151028T2057
15229736348973987	lux10_20151029T1250
15235372692921061	lux10_20151030T0646
15250357231361332	lux10_20151101T0151
15310574580039790	lux10_20151108T0051
15316808566694652	lux10_20151108T1702
15349610250298850	lux10_20151112T1205
15353868193263472	lux10_20151112T2010
15372544237281326	lux10_20151115T0051
15381291695041372	lux10_20151116T0101
15385954384244968	lux10_20151116T1350
15423066604080874	lux10_20151121T0052
15455599969523886	lux10_20151124T1332
15467749354190423	lux10_20151126T0530
15482805621857896	lux10_20151127T1917
15498535463245931	lux10_20151129T1644
15558220982352426	lux10_20151206T1645
15558252721141702	lux10_20151206T1645
15573901194255673	lux10_20151208T0928
15578587170712937	lux10_20151208T2336
15615616533579611	lux10_20151213T0051
15630451178899646	lux10_20151214T1857
15655063940904710	lux10_20151217T2125
15676377326968378	lux10_20151220T0842

Table A.1: Luxstamps and dataset prefixes for throughgoing muons.

luxstamp	dataset_prefix
15679801286649183	lux10_20151220T1622
15694947748323835	lux10_20151222T0953
15696609052856760	lux10_20151222T0953
15699674855161506	lux10_20151223T0141
15706658811052500	lux10_20151223T1654
15708947185396770	lux10_20151224T0041
15729687131422906	lux10_20151226T0559
15738030645301827	lux10_20151227T0838
15757490258838285	lux10_20151229T1647
15757562628233667	lux10_20151229T1647
15758747851980355	lux10_20151229T1647
15759588310284104	lux10_20151230T0033
15770733714095334	lux10_20151231T0515
15787640037463326	lux10_20160102T0411
15789049794117702	lux10_20160102T0411
15792583584398261	lux10_20160102T1947
15815887503572630	lux10_20160105T0740
15822971788974512	lux10_20160106T0208
15837722020823748	lux10_20160107T2328
15853280432623659	lux10_20160109T1804
15871653770074657	lux10_20160111T1937
15876531013973254	lux10_20160112T1121
15899087160632344	lux10_20160115T0225
15915618318290851	lux10_20160117T0051
15962893804106079	lux10_20160122T0957
15985236223153569	lux10_20160125T0024
15989476880187655	lux10_20160125T1213
15989556015782694	lux10_20160125T1213
15994665801122882	lux10_20160126T0352
16026363452460545	lux10_20160129T2006
16059339021498780	lux10_20160202T1607
16178701299020226	lux10_20160216T1051
16182184964397259	lux10_20160216T1820
16184761616050908	lux10_20160217T0156

Table A.1: Luxstamps and dataset prefixes for throughgoing muons.

luxstamp	dataset_prefix
16215564412191787	lux10_20160220T1453
16273395439310384	lux10_20160227T0653
16295569190363066	lux10_20160229T2211
16298967518829770	lux10_20160301T0545
16299676344739955	lux10_20160301T0545
16307893932612085	lux10_20160302T0658
16343472252547184	lux10_20160306T0821
16353085188363156	lux10_20160307T1120
16356660256345364	lux10_20160308T0229
16391322084951938	lux10_20160312T0313
16392894502598673	lux10_20160312T0313
16393055600417955	lux10_20160312T0313
16408932760322850	lux10_20160314T0027
16409724444559249	lux10_20160314T0027
16413812516055798	lux10_20160314T1537
16446242056077636	lux10_20160318T0735
16475386838098647	lux10_20160321T1518
16480384242512772	lux10_20160322T0622
16498206669101168	lux10_20160324T1211
16510892478894144	lux10_20160325T2026
16544803706942035	lux10_20160329T1529
16634604776833078	lux10_20160409T0609
16645872763145593	lux10_20160410T0916
16667742273242059	lux10_20160412T2056
16686590840534756	lux10_20160415T0225
16687042670061081	lux10_20160415T0225
16713991806468105	lux10_20160418T0808
16724959833379377	lux10_20160419T1702
16730392259319348	lux10_20160420T0907
16746237462991856	lux10_20160421T2247
16747390945931150	lux10_20160422T0623
16747612809395809	lux10_20160422T0623
16748695024663186	lux10_20160422T0623
16751207722060731	lux10_20160422T1346

Table A.1: Luxstamps and dataset prefixes for throughgoing muons.

luxstamp	dataset_prefix
16768295643263868	lux10_20160424T1702
16784320213113238	lux10_20160426T1312
16817660366808480	lux10_20160430T0805
16820014674389255	lux10_20160430T1528